ON THE GENESIS OF DIVERGENCE AND GRAVITY WAVE EMISSION FROM OSCILLATING BAROTROPIC VORTICES IN ROTATING FLUIDS

SANGAY TSHERING BHUTIA

A DISSERTATION SUBMITTED TO
THE FACULTY OF GRADUATE STUDIES
IN PARTIAL FULFILLMENT OF THE REQUIREMENTS
FOR THE DEGREE OF
DOCTOR OF PHILOSOPHY

GRADUATE PROGRAM IN EARTH AND SPACE SCIENCE
YORK UNIVERSITY
TORONTO, ONTARIO

November 2016

Abstract

Internal gravity waves are ubiquitous in the atmosphere. Our understanding of gravity wave emission from atmospheric jet-front systems, such as the baroclinic vortices, has considerably improved over the past decade. Interestingly, even unstable barotropic jets are known to emit gravity waves. However, the wave generation mechanism in barotropic vortices is thought to be different than in baroclinic vortices. Yet, our current understanding of the wave generation mechanism fails to draw a clear distinction between the emission mechanisms in barotropic and baroclinic vortices; indicating that a deeper understanding of the wave generation is required than which is currently known.

The present study focuses on gaining a better understanding of gravity wave generation mechanism from unstable barotropic jets. A more detailed study of the wave emission mechanism is performed compared to the earlier studies. New details about the wave forcing mechanism from unstable barotropic jets are identified, which provides a much clear picture of the wave emission mechanism from barotropic jets.

The role of planetary vorticity in inhibiting gravity wave emission and its representation in the Ford-Lighthill formulation is elucidated. Gravity wave emission associated with vortex merging is also investigated. This study also provides important insight on the source and significance of divergence in fluid motions.

Dedication

Especially, to my parents Nini and Urgyen, and my dear sister Tshering Kyipa.

Acknowledgments

First, I would like to take this opportunity to express my gratitude to my supervisor Prof. Gary Klaassen. For allowing me to work towards my dissertation under his supervision, and then, importantly, introducing me to this elusive, but interesting problem of gravity wave emission. It has been a long journey, filled with many hardships, and this would not have been possible without him. I thank him for sharing some of his incredible wealth of knowledge, his guidance, his incredible insight which have proved so valuable in completion of my dissertation, his encouragement, the support he has shown in matters even outside research, and his incredible patience. I am forever indebted to him.

I would also like to take this opportunity to thank my supervisory committee members: Prof. James Whitway and Prof. Yongsheng Chen. I thank them for sharing their knowledge, their advice, and all the support they have shown over the years. They have been invaluable. I would also like to thank the rest of the examining committee members: Prof. Wayne Hocking, Prof. Keith Aldridge, and Prof. Dong Liang, for agreeing to be in my committee, and for their comments and constructive criticisms, which have improved my thesis.

I would also like to thank our Graduate Program Direction, Prof. Sunil Bishnath; administrative assistants, Marcia Gaynor and Paola Panaro; and Robert Milverton, for their help and support. I would also like to thank all my friends. Especially, Abhay and Sanchari Rai, Sopan Kurkute, Mahtab Majdzadeh, Richard Liang, Ramtin Ardeshiri , Yoonseok Jwa, Brian (Heungsik) Kim, and many others. Thank you all, for the help and good memories. Lastly, I would like thank my family members for being so supportive. Especially, my aunt and uncle, Pema and Alexander Shyodhi, for their love and support during my undergraduate years in Mumbai, India.

Contents

List of Tables

List of Figures

Chapter 1

Introduction

1.1 Introduction

Internal gravity waves are ubiquitous in our atmosphere. They are generated by various physical processes. Considerable progress has been made in our understanding of gravity waves induced by topography. However, there have also been numerous studies of gravity wave activity associated with meteorological motions other than the ones induced by topography. Observations and models have revealed a broad range of internal gravity waves ranging from high-frequency gravity waves associated with frontal motions to near-inertial low-frequency gravity waves associated with evolution of upper level jet streams (see e.g., Fritts and Alexander 2003; Plougonven and Zhang 2014). Deep moist convection is also another source of internal gravity waves. The present study will focus on non-convective and non-orographic sources.

In spite of the numerous observations and modelling studies, our understanding of gravity wave emission from synoptic scale jets and vortices is still incomplete. One of the primary difficulties that has hindered progress can be un-

derstood as follows. Our large-scale atmosphere is characterized by flows which evolve very slowly at time-scales of the order of few days. These slow motions tend to remain mostly balanced as they evolve, i.e., pressure gradient forces are nearly balanced by the Coriolis force in the horizontal and gravitational forces in the vertical (see e.g., Holton 2004; Vanneste 2013). Since the large-scale flows evolve very slowly at time-scale of the order of few days and tend to remain mostly near a state of balance, they are not expected to force short-scale high-frequency gravity waves. A measure of this weak coupling is estimated by smallness in the Rossby number Ro, which is a dimensionless number, and is defined as

$$Ro = \frac{U}{fL},$$

(1.1)

where U and L are characteristic velocity and length scales, respectively, and f is the *Coriolis parameter*, which is defined as $f = 2\Omega \sin \phi$, where Ω is the angular velocity of rotation of the Earth, and ϕ is the latitude. Since f is the low-frequency limit of inertia-gravity waves and L/U indicates the time-scale of evolution of the slow balanced motion, the smallness of Ro then indicates the separation in time-scale. The gravity wave emission associated with the evolution of a predominantly balanced motion is referred to as *spontaneous emission or adjustment* to distinguish it from *geostrophic adjustment* (see e.g., Plougonven and Zhang 2014; Vanneste 2013).

Since observations have indicated upper level jet-front systems as active sites for gravity waves activity, several researchers have used numerical simulation to study the evolution of an idealized baroclinic[1] (e.g., O'Sullivan and Dunkerton 1995; Zhang 2004; Plougonven and Snyder 2006; Wang and Zhang 2007; see also Plougonven and Zhang 2014 and references therein). Their aim was to seek an

---

[1]A fluid in which density depends on both temperature T and pressure p, $\rho = \rho(T,p)$, is referred to as a *baroclinic* fluid. In such a fluid, surfaces of constant density are not parallel to surfaces of constant pressure (see also fig. (1.1)).

understanding of how a predominantly large-scale, slow, nearly balanced motion leads to the excitation of shorter scale inertia-gravity waves having somewhat shorter time scales.

The notion of balanced flow exciting gravity waves is not just restricted to low Rossby number large-scale balanced flows, but has also been demonstrated in the case of Rossby number order one flows, such as small-scale shallow-water barotropic[2] vortices. These vortices are known to adjust by emission of shallow-water gravity waves. For example, Ford (1994a) demonstrated through numerical simulation that even small-scale (small compared to Rossby radius of deformation[3] R_d) shallow-water vortices with Rossby number order one magnitude emit shallow-water gravity waves during their evolution. The characteristics of emitted gravity waves suggests that these waves are generated by a mechanism which is analogous to Lighthill's (1952) theory of aerodynamic sound generation from small-scale turbulence. Consequently, the gravity wave emission associated with shallow-water vortices have been referred as *Lighthill emission*.

In addition, unstable axisymmetric small-scale shallow-water vortices with Rossby number order one are known to emit gravity waves (Ford 1994b; Schecter and Montgomery 2006). These gravity waves are also known to have been emitted by the Lighthill mechanism, because the emitted waves have wavelengths long compared the size of the vortices.

Over the last decade, significant progress has been made in our understanding of the gravity wave generation from upper-level jet-front system, mainly from numerical simulations of idealized baroclinic waves (Zhang 2004; Plougonven and

---

[2]A *barotropic fluid* is one in which density ρ depends only on pressure p, $\rho = \rho(p)$, so that surfaces of constant density are also surfaces of constant pressure. In the case of shallow-water flows, the density is constant, so the fluid is barotropic (see also fig. (1.1)).

[3]Rossby radius of deformation R_d is defined as the horizontal scale at which rotation effects become as important as stratification effects (Gill 1982).
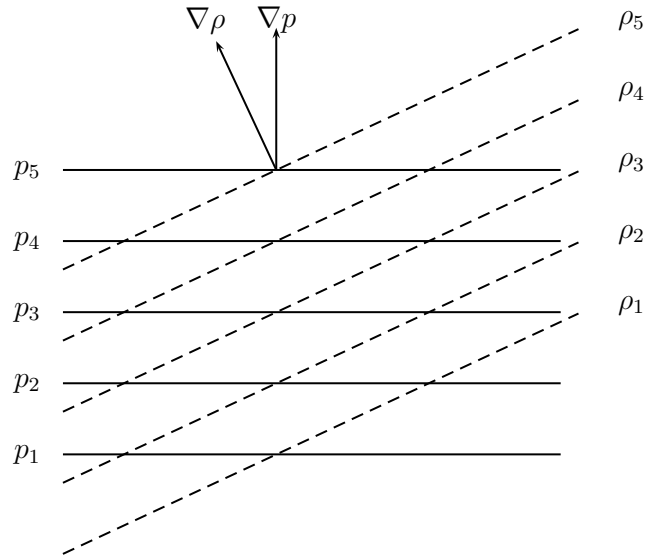
Figure 1.1: A schematic illustrating the situation in barotropic and baroclinic fluids. Solid lines represent lines of constant pressure p, dashed lines represent lines of constant density ρ, and the indices indicate different layers. In case of a barotropic fluid, the lines of constant density are parallel to lines of constant pressure, so $(\nabla\rho \times \nabla p) = 0$, where ∇ is the gradient operator, and in the case of a baroclinic fluid, the lines are not parallel, so $(\nabla\rho \times \nabla p) \neq 0$.

Snyder 2006; Wei and Zhang 2014). The gravity wave generation mechanism associated with the evolution of a baroclinic wave is thought to be different from the Lighthill mechanism. The argument that has often been invoked is that, in the case of Lighthill's emission, the emitted waves propagate exactly horizontally away from the source region, and have wavelengths very long compared to the spatial scale of the flow generating the wave. In contrast, gravity waves forced by large-scale flows, such as baroclinic vortices, tend to have horizontal spatial scale very short compared to the size of the baroclinic vortices (see e.g., Plougonven and Zhang 2014 and references therein), and they propagate predominantly vertically.

Although it has been constantly argued that the Lighthill mechanism is different from the wave generation mechanisms from baroclinic vortices, none of the studies have questioned why the Lighthill mechanism is absent in the case of baroclinic vortices. In both the mechanisms, the nonlinear advection terms play a crucial role in producing wave forcing. So then, how does one kind of forcing result in long waves and the other in short waves ?

Significant insight into this problem can be obtained from the work carried out by Harada and Ishioka (2011). Harada and Ishioka (2011) using a constant f-plane two-layer shallow-water model were able to simulate the gravity wave emission associated with the evolution of both barotropic and baroclinic instability. Their study showed that as the Rossby number is decreased there occurs a transition from barotropic to baroclinic instability regime, and also observed is a transition in the characteristics of the emitted waves. So could it be that, in the case of baroclinic vortices, the Lighthill mechanism is suppressed due to the increased effect of background rotation as the Rossby number is decreased ? And that the wave generation mechanism in baroclinic vortices is such that it is not affected by this increased background rotation ?

A lot of past research has focused on understanding the wave emission associated with baroclinic vortices, but relatively few have focused on wave emission from unstable parallel barotropic flows. Past research on wave emission from barotropically unstable parallel flows, such as Ford (1994a) and Sugimoto et al. (2008), have focused on comparing the simulated wave with that predicted by Ford's modified version of Lighthill's (1952) theory. Consequently, our knowledge of the process of wave emission mechanism have come primarily from the insights obtained using Lighthill-like formulation. Yet, our current understanding of the wave generation mechanism fails to draw a clear distinction between the emission mechanisms in barotropic and baroclinic vortices. This suggests that a deeper understanding of the wave forcing mechanism is required than that is currently known.

The present study therefore revisits the problem of shallow-water gravity wave emission from rotating shallow-water barotropic vortices. Our aim is gain a better understanding of the wave-forcing mechanism associated with shallow-water barotropic vortices with Rossby number order one. Our approach is to use numerical simulations to perform a more detailed investigation of the wave emission mechanism compared to the earlier studies. This study will help in identifying some new characteristics or some new details associated with the wave forcing mechanism, which will be useful in drawing some distinction between the mechanisms observed in barotropic and baroclinic cases. We hope that our study will serve as a step towards a better understanding of this problem.

1.2   Outline of the thesis

The outline of the thesis is as follows. In the remainder of chapter 1, the fundamental concepts that are essential to the understanding of atmospheric fluid dynamics are introduced. The shallow-water equations and the assumptions inherent in these equations are discussed. The significance of using shallow-water equations to study atmospheric motions and the important properties which the shallow-water equations share with atmospheric flows are addressed. The limitations of shallow-water equations in studying atmospheric motions are also highlighted. This introductory survey will serve to provide the necessary foundations for understanding more advanced topics to be considered in the later chapters.

In Chapter 2, the shallow-water analogue of Lighthill's (1952) theory of aerodynamic sound generation is discussed. Our aim is to highlight the key aspects of Lighthill's formulation of the aerodynamic wave generation problem. The shallow-water analogue of Lighthill's (1952) theory of aerodynamic sound generation is presented. Then Ford's (1994a) extension of the shallow-water analogue of Lighthill's theory to rotating fluid is reviewed, and the fundamental differences that arise as a consequence of the effect of background rotation are highlighted and discussed.

In Chapter 3, we perform simulations showing shallow-water gravity wave emission from an initially parallel unstable jet in a constant f-plane shallow-water model. Earlier studies focused more on comparison of the simulated field with the predictions based on Ford's (1994a) extension of Lighthill's (1952) theory of aerodynamic sound generation. Consequently, our understanding of the wave emission mechanism from shallow-water barotropic vortices comes primarily from the insight obtained using the Lighthill's formulation. Our approach, in chapter 3, is to conduct a more detailed and thorough analysis of the numerical simulation results,

compared to earlier studies (Ford 1994a; Sugimoto et al. 2008), to gain additional insight to the wave emission mechanism. We also investigate the numerical errors that arise during the nonlinear advection of the potential vorticity anomaly as a consequence of insufficient resolution. The results from the simulation are also compared with some of Ford's (1994a) simulation results. The sensitivity of model resolution and dissipation to the process of gravity wave generation are also investigated.

In Chapter 4, we carefully review the details of the Green's function solution of the Ford-Lighthill equation with the aim of identifying some limitations of using Lighthill formulation to study wave emission mechanisms. The solution thus obtained is compared with the simulated wave field. Some remarks are made based on this result. We also investigate the contribution of the individual forcing terms in the Ford-Lighthill equation to the simulated wave with the aim of gaining some insight into the wave forcing terms. Of particular interest is the contribution of the additional Coriolis term that arises in Ford's formulation.

In Chapter 5, the process of wave emission associated with the process of vortex merging is investigated using the rotating (constant f) shallow-water model. Differences with the single vortex case are highlighted. Specifically, it is known that merging of vortices results in increasing the size and amplitude of the vortices. The significance of these changes to the gravity wave emission are investigated.

Finally, in chapter 6 we summarize the work that was undertaken, make some concluding remarks, and suggest some potential topics for further research.

1.3 Shallow-water equations and geophysical fluid dynamics

1.3.1 Non-rotating fluids

The shallow-water equations, as their name suggests, are ideal for describing the motion of a shallow-layer of incompressible fluid with free surface, such as oceans, lakes, rivers, etc. However, the shallow-water equations are also often used for studying atmospheric flows. One reason for this is that they form the simplest set of equations that can be used to describe the horizontal structure of the atmosphere, in comparison to the full Navier-Stokes equations. More importantly, despite their simplicity, the shallow-water equations possess important properties which they share with atmospheric and oceanic flows, namely the ability to represent both rotating quasi-geostrophic and wave motions.

The inviscid shallow-water equations for a non-rotating fluid comprises the horizontal momentum equations (see e.g., Holton 2004; Gill 1982; Kundu 1990),

$$\partial_t \mathbf{u} + \mathbf{u} \cdot \nabla \mathbf{u} = -g \nabla h, \tag{1.2}$$

and the continuity equation,

$$\partial_t h + \nabla \cdot (h\mathbf{u}) = 0, \tag{1.3}$$

where $\mathbf{u}$ is the horizontal velocity vector, ∇ is the horizontal gradient operator, and h is the height of the free surface of the fluid, and g is the acceleration due to gravity.

The shallow-water equations are typically used to describe atmospheric

flows for which the following assumptions can be considered to be valid. Density variations can be ignored, i.e., parcels can't be compressed. The vertical depth scale is small compared to the horizontal scale such that the flow can be approximated to be in *hydrostatic balance*. Furthermore, the depth of the fluid is shallow enough that the vertical shear of the horizontal wind can be considered negligible. Lastly, the shallow-water continuity equation can be derived on the basis that the fluid horizontal divergence is independent of depth (see e.g., Holton 2004; Gill 1982; Kundu 1990).

1.3.2 Rotating shallow-water equations

Since our Earth is constantly rotating on its axis and we are also rotating with it, it is simpler to study large-scale atmospheric motions from a rotating or non-inertial frame of reference, as opposed to some fixed or inertial frame of reference.

The inviscid shallow-water equations in a rotating frame (e.g. Gill (1982)) reads as

$$\partial_t \mathbf{u} + \mathbf{u} \cdot \nabla \mathbf{u} + f\mathbf{k} \times \mathbf{u} = -g\nabla h, \tag{1.4}$$

and

$$\partial_t h + \nabla \cdot (h\mathbf{u}) = 0, \tag{1.5}$$

where $\mathbf{u}$, now, represents the horizontal velocity vector relative to the rotating frame, $\hat{\mathbf{k}}$ is the unit vector along the local vertical, and f is the *Coriolis parameter*. The details of the transformation from fixed to rotating frame will not be provided here, and can be found in most of the standard textbooks on atmospheric science (see e.g., Holton 2004; Cushman-Roisin and Beckers 2010). Except for the additional term $(f\mathbf{k} \times \mathbf{u})$ in the momentum equations, the rotating shallow-water equations are identical to the non-rotating equations. This new term is known as

10

the *Coriolis force*. The Coriolis force deflect parcels at a right angle to the horizontal flow. The direction of the Coriolis force is such that a moving fluid particle is deflected towards the right in the Northern hemisphere and towards the left in the Southern hemisphere (see e.g., Holton 2004). In this study we will assume f is a constant for simplicity. This assumption is consistent with the scale of the vortices to be considered.

1.3.3 Planetary vorticity, Rossby number and its significance

Consider a circular ring of fluid undergoing solid body rotation along a specific latitude with angular velocity equal to the rotation of Earth (Ω). Let R be the distance of the ring from the the axis of rotation of the earth and $\mathbf{R}$ the position vector of an element of fluid of the ring. Then the velocity of the fluid $\mathbf{U_e} = \mathbf{\Omega} \times \mathbf{R}$, where direction of Ω is the along the axis of rotation. Such a fluid ring possesses vorticity equal to $\nabla \times \mathbf{U_e}$. Now by vector identity (Holton 2004)

$$\nabla \times \mathbf{U_e} = \nabla \times (\mathbf{\Omega} \times \mathbf{R}) = \mathbf{\Omega}\nabla \cdot \mathbf{R} = 2\mathbf{\Omega} \tag{1.6}$$

The component of $2\mathbf{\Omega}$ along the local vertical, i.e., $2\Omega \sin\phi$, is the vorticity corresponding to a parcel at rest relative to the surface of the earth, and is referred to as *planetary vorticity*. Since ϕ varies across the globe, planetary vorticity is not a constant but varies with latitude (ϕ). Planetary vorticity has a value of zero along the equator. At a latitude of 45° the value of planetary vorticity is approximately 1×10^{-4} s^{-1}. Notice that the expression for the planetary vorticity is identical to the expression for the Coriolis parameter f. Consequently, planetary vorticity is also referred to by the symbol f. The fact that these expressions are identical has consequences.

As a consequence of observing motion in a rotating frame, the vorticity associated with fluid motions can always be expressed as a sum of planetary vorticity f and the vorticity measured relative to the rotating frame, which is referred to as relative vorticity. When the magnitude of relative vorticity is very small compared to the planetary vorticity, we can expect the fluid motions to be strongly influenced by the presence of the background planetary vorticity f. If U and L represents the velocity and the spatial scale associated with the flow, then the relative vorticity scales as U/L. Then the ratio of the relative vorticity scale to planetary vorticity f gives a estimate of *Rossby number* (Ro), which indicates the effect of rotation of the earth on the fluid motions. Large scale (spatial scale greater than 1000 km) atmospheric motions in mid-latitudes tend to have $Ro \ll 1$, and are thus strongly influenced by the Earth's rotation (Holton, 2004). On the other hand, small scale flows tend to have large relative vorticity compared to the planetary vorticity f, and have Rossby number large compared to one. Therefore, when considering small scale fluid motions the effect of planetary vorticity is sometimes ignored.

1.3.4 Potential vorticity

A concept that has proven useful for our understanding of the dynamics of the large-scale atmospheric fluid motions is *potential vorticity η*. Potential vorticity is a conserved scalar quantity under certain conditions. Our atmosphere on the large-scale behaves as a shallow layer of nearly inviscid, adiabatic fluid with vertical motions in hydrostatic balance. This gives rise to a scalar invariant following the motion of the fluid known as *quasi-geostrophic potential vorticity* (see e.g., Holton 2004). The prefix *quasi-geostrophic* is added because the horizontal motions also tend to remain in a state close to *geostrophic balance*.

A more general form of potential vorticity η applicable to the atmosphere takes the form (Holton 2004)

$$\eta = (\zeta_\theta + f)\left(-g\frac{\delta\theta}{\delta p}\right)$$

where ζ_θ is the vertical component of relative vorticity evaluated on a isentropic surface with potential temperature θ, g is the acceleration due to gravity, and δp represents the pressure difference between layers of potential temperature θ and $(\theta + \delta\theta)$.

Since shallow-water equations also permit both vortical and divergent fluid motions, an analogous scalar quantity arises which remains materially conserved following the fluid motions. It is referred to as the *Rossby potential vorticity* η (e.g. Gill 1982; Holton 2004)

$$\eta = \frac{\zeta + f}{h}$$

where

$$\zeta = \hat{\mathbf{k}} \cdot \nabla \times \mathbf{u}$$

is the vertical component of relative vorticity.

1.3.5 Shallow-water gravity waves

The shallow-water equations permit divergent waves which are known as shallow-water gravity waves. In order to see that these waves are divergent, we linearize the shallow-water equations (1.4) - (1.5) about a basic state at rest. The linearized

equations are

$$\partial_t u' - fv' + g\partial_x h' = 0 \tag{1.7}$$

$$\partial_t v' + fu' + g\partial_y h' = 0 \tag{1.8}$$

$$\partial_t h' + h_r(\partial_x u' + \partial_y v') = 0 \tag{1.9}$$

where the primes indicate the small amplitude disturbances imposed on the motionless basic state, and h_r is the height of the fluid at rest. Using the linearized equations we first derive the divergence and vorticity equations. Taking the x-derivative of (1.7) and y-derivative of (1.8) and adding the resulting equations we get the linearized divergence equation,

$$\partial_t \delta' - f\zeta' = -g\nabla^2 h', \tag{1.10}$$

where

$$\delta' = (\partial_x u' + \partial_y v'),$$

is the divergence δ' associated with the perturbations, and

$$\zeta' = (\partial_x v' - \partial_y u'),$$

is the relative vorticity ζ' of the perturbations. Taking x-derivative of (1.8) and y-derivative of (1.7) and subtracting the latter from the former we get the linearized vorticity equation,

$$\partial_t \zeta' = -f\delta' \tag{1.11}$$

Taking the time derivative of the divergence equation, and making use of the linearized continuity equation (1.9) and the linearized vorticity equations, we obtain

a second order equation for δ',

$$\left(\partial_{tt}^2 + f^2\right)\delta' - (gh_r)\nabla^2\delta' = 0, \tag{1.12}$$

where ∇^2 $(= \partial_{xx}^2 + \partial_{yy}^2)$ is the horizontal Laplacian operator.

Setting $f = 0$ (i.e., the non-rotating case) in the last equation reduces it to the familiar second-order wave equation for δ'

$$\partial_{tt}^2\delta' - c^2\nabla^2\delta' = 0, \tag{1.13}$$

where c $(= \sqrt{gh_r})$ is speed with which a *non-rotating* shallow-water gravity wave propagates in a fluid at rest. Thus the *non-rotating* shallow-water gravity waves are divergent and non-dispersive waves.

The inclusion of the effect of rotation (i.e., $f \neq 0$) renders the shallow-water waves dispersive. The dispersion relation for the rotating shallow-water gravity wave can be obtained by seeking normal mode solutions of the form

$$\delta' = \hat{\delta}e^{i(kx+ly-\omega t)} = \hat{\delta}e^{i(\mathbf{k}.\mathbf{x}-\omega t)}$$

in (1.12), whence we obtain

$$\omega^2 = f^2 + gh_r|\mathbf{k}|^2 \tag{1.14}$$

where ω is the angular frequency, and $\mathbf{k}$ is the horizontal wavenumber vector. Expression (1.14) also indicates that, contrary to the *non-rotating* case, the *rotating* shallow-water gravity waves have a low-frequency limit equal to f, which is referred to as the *inertial* frequency .

Dividing (1.14) by $|\mathbf{k}|$, we get the expression for the phase speed of the
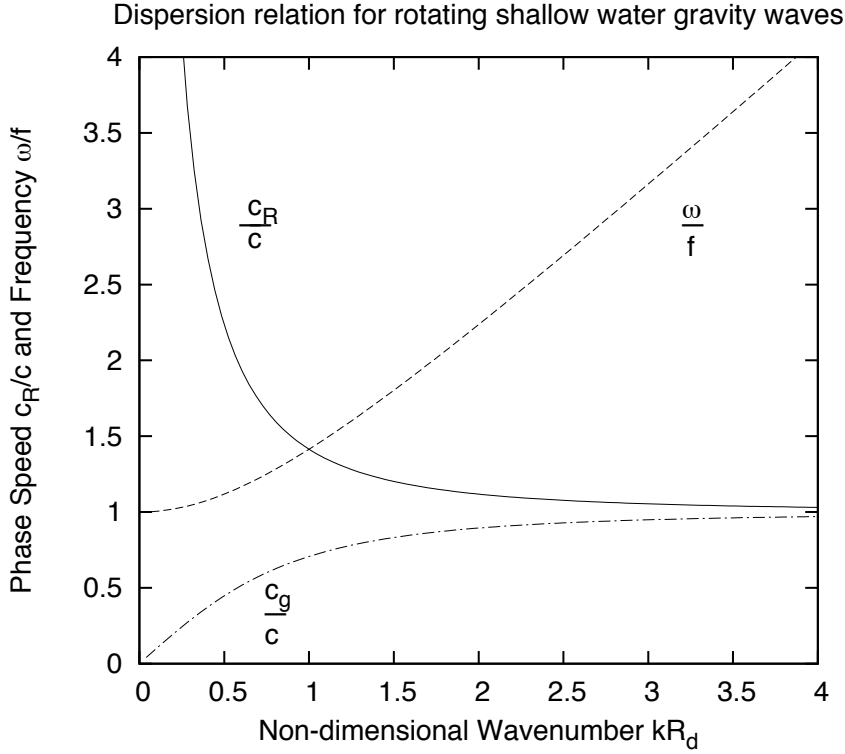
Figure 1.2: Plot showing the non-dimensional phase speed c_R/c, group speed c_g/c and frequency ω/f versus the non-dimensional wavenumber kR_d.

rotating shallow-water gravity wave,

$$c_R^2 = \omega^2/|\mathbf{k}|^2 = gh_r + f^2/|\mathbf{k}|^2. \tag{1.15}$$

The last expression indicates that, unlike the non-rotating case, the rotating shallow-water phase speed c_R increases as $|\mathbf{k}|$ approaches 0, and for short waves (i.e., $|\mathbf{k}| \gg 1$), the c_R approaches the *non-rotating* phase speed c. Thus the effect of rotation renders the wave dispersive, and this effect becomes more important as the waves get longer.

The expression for the group velocity c_g is

$$c_g = \frac{\partial \omega}{\partial k_H} = \frac{gh_r}{c_R} \tag{1.16}$$

16

where $k_H = |\mathbf{k}|$. Fig. (1.2) shows the dispersion relation for rotating shallow-water gravity waves. Also shown are the phase speed c_R and group velocity c_g.

1.3.6   Geostrophic balance

Observations indicate that in the case of the large-scale flow outside the tropics and above the boundary layer, the Coriolis force is of the same order of magnitude as the pressure gradient force. This state of approximate balance between the Coriolis force and the pressure gradient force is known as *geostrophic balance.* Geostrophic balance indicates that at these scales the horizontal motions are strongly influenced by rotation of the earth.

Since the Coriolis parameter f $(= 2\Omega \sin \phi)$ varies with latitude (ϕ), the Coriolis force $(f\hat{\mathbf{k}} \times \mathbf{v})$ also varies with it. Consequently, the length-scale over which the flow is in geostrophic balance also varies with latitude.

1.3.7   Rotating shallow-water gravity waves and Rossby radius of deformation R_d

It is evident from (1.15) that when the length scale $|\mathbf{k}|^{-1}$ of a disturbance becomes equal to $\sqrt{gh_r}/f$, both the terms on the right hand side (rhs) of (1.15) make equal contributions to the rotating shallow-water phase speed c_R. As will be demonstrated below, the first term (gh_r) in the rhs of (1.15) can be used to represent the effect of stratification in stratified fluids. The second term in (1.15) captures the effect of rotation. Therefore, this natural length scale $\sqrt{gh_r}/f$ at which the effect of rotation becomes equally important as the effect of stratification can be defined as the *Rossby radius of deformation* (R_d) for the rotating shallow-

17

water equations (Gill 1982; Holton 2004), i.e.,

$$R_d = \frac{\sqrt{gh_r}}{f}.$$ (1.17)

Consequently, R_d can also be interpreted as the distance that the shallow-water gravity wave propagates in inertial time scale. In what follows, we will be demonstrated how the first term in (1.15), i.e., (gh_r), can be used to indicate the effect of stratification.

We now estimate the value R_d that is of relevance in our atmosphere. Our atmosphere is a continuously stratified fluid, but expression (1.17) is valid only for a homogeneous layer of fluid with a free surface. If we assume that the troposphere behaves as a homogeneous fluid and the tropopause behaves like an interfacial surface, then the value R_d for such an atmosphere can be readily calculated. The typical value of f in the mid-latitudes is 10^{-4} s^{-1}, then assuming that height of the tropopause h_r is 10 km and taking $g = 9.81$ ms^{-2}, we get phase speed $\sqrt{gh_r}$ ≈ 300 m/s, and $R_d \approx 3000$ km. Although observations indicate that length scales of approximately 3000 km are commonly associated with mid-latitude synoptic scale weather systems (Holton, 2004), however, a phase speed of 300 m/s is still too close to the speed of sound, and therefore overestimates the phase speed of internal gravity waves that are of mesoscale meteorological significance in a stratified atmosphere.

We now estimate the value of the Rossby radius of deformation in the case of a continuously stratified atmosphere. This is achieved by first defining a homogeneous or shallow-water equivalent for the continuously stratified atmosphere (see e.g., Gill 1982). In the case of our atmosphere, the *Brunt-Vaisala* or stratification

frequency N is defined by

$$N^2 = \frac{g}{\theta}\frac{\partial\theta}{\partial z} \tag{1.18}$$

where θ is the potential temperature, and z indicates the vertical coordinate. To a first order approximation, we can write $N^2 \approx (g\Delta\theta/\theta\Delta z)$, where $\Delta\theta$ now indicates a difference in potential temperature across a height Δz. Then one can define *reduced* gravity $g' = g\Delta\theta/\theta$, and letting $\Delta z = h_r$, we get

$$\sqrt{g'h_r} \approx Nh_r. \tag{1.19}$$

The term on the left hand side $\sqrt{g'h_r}$ can be identified as the phase speed of a non-rotating shallow-water gravity wave, but with g now replaced by g'. Relation (1.19) indicates that increasing N, i.e., increasing stratification, is equivalent to increasing the phase speed of the equivalent shallow-water wave, and, consequently, the R_d. It is also now clear that the term $\sqrt{gh_r}$ in (1.15) is analogous to a *buoyancy* effect.

The typical value of N in troposphere is 10^{-2} s^{-1}, and using $h_r = 10$ km, we get $\sqrt{g'h_r} = 100$ m/s, and R_d ($= \sqrt{g'h_r}/f$) $= 1{,}000$ km. Using $h_r = 3$ km reduces $\sqrt{g'h_r}$ to 30 m/s and R_d to 300 km. These values of phase speed and Rossby radius are smaller compared to the earlier estimates, which neglected the effects of stratification. This indicates that using $g = 9.8$ m/s overestimates the effect of stratification, and that g should be replaced by g'. Using reduced gravity slows the shallow water speeds into the same range as internal gravity waves.

1.3.8   Shallow-water vortical waves

Interestingly, the shallow-water equations permit not just gravity waves but also vortical waves. Among the vortical waves, the shallow-water equations also permit the shallow-water analogue of the atmospheric Rossby wave. These waves are different from shallow-water gravity waves in that they arise as a consequence of conservation of absolute vorticity, where absolute vorticity is defined as sum of planetary vorticity (f) and relative vorticity (ζ). And the same is true for atmospheric Rossby waves. In the case of the atmospheric Rossby waves, the factor that is responsible for the propagation of the wave is the meridional gradient of the planetary vorticity f. The intrinsic phase speed of the atmospheric Rossby wave is

$$c_{Rossby} = -\beta/k^2,$$

where β is the meridional gradient of planetary vorticity f, and k is the zonal wavenumber of the wave (Holton 2004). Consequently, unlike the shallow-water gravity waves, the phase speed of Rossby wave is independent of depth of the fluid. We note that Rossby waves are also dispersive waves whose phase speed increases with the wavelength of the disturbance. An estimation of the Rossby wave speed can be made by using the typical mid-latitude value of β equal to 10^{-11} m^{-1}s^{-1}. Then zonal wavelengths of 1000 - 10,000 km results in phase speed in the range 0.25 - 25 ms^{-1}. For the purposes of our study f is assumed constant, and since Rossby waves depend on the meridional gradient of f for propagation, these waves are filtered out and will not be considered in the rest of this thesis.

1.3.9 Limitations of shallow-water equations

One of the main limitations of the shallow-water equations is its lack of stratification. Since our atmosphere and oceans are continuously stratified fluids, under statically stable or stably stratified conditions, it permits the propagation of what are known as *internal gravity* or *buoyancy* waves. These waves are generated when a vertically displaced air parcel under statically stable conditions undergoes purely vertical oscillations about its equilibrium level with frequency equal to the *Brunt-Vaisala* or *buoyancy* frequency N, and if the parcel oscillations are slantwise then frequency is less that N. The value of N is a measure of the static stability of the environment. In the atmosphere N is determined by the expression (1.18). Positive values of N^2 indicates statically stable condition, negative values indicates statically unstable condition, and zero indicates neutral conditions. The average value of N in the troposphere is 1.2×10^{-2} s^{-1}, so the period of buoyancy oscillation $(2\pi/N)$ is about 8 min.

The dispersion relation for a nonhydrostatic internal gravity wave (see e.g. Holton 2004) is

$$\omega = \pm Nk/|\mathbf{k}| = \pm N \cos \beta \tag{1.20}$$

where $\mathbf{k} = (k, m)$ is the wavenumber vector with k and m being the horizontal and vertical wavenumber, respectively, and β is the angle between the horizontal and the wavevector $\mathbf{k}$. Internal gravity waves that are affected by rotation of the Earth have frequency close to inertial frequency f are known as *inertia-gravity* waves. The dispersion relation of a hydrostatic inertia-gravity wave is (see e.g. Holton 2004)

$$\omega^2 = f^2 + N^2(k^2 + l^2)/m^2 \tag{1.21}$$

Since the above expression is derived under the assumption that waves are in hydrostatic balance, we have $(k^2 + l^2)/m^2 \ll 1$, which implies that

$$|f| \leq |\omega| \ll N.$$

Internal gravity waves under suitable conditions can propagate vertically into the atmosphere. These waves are thus very different from shallow-water gravity waves. Shallow-water waves are interfacial waves and consequently, propagate only horizontally. Dispersion relations (1.20) and (1.21) highlight an important characteristic which distinguishes internal gravity waves from a shallow-water gravity waves, i.e., the normalized frequency ω/N of an internal gravity wave depends only on the angle β between the wavenumber vector $\mathbf{k}$ and the horizontal.

1.3.10 Comparison of shallow and internal gravity waves

Even though shallow-water waves are very different from internal gravity waves in their propagation characteristics, the similarities in their dispersion relation opens up the possibility of defining a shallow-water equivalent of an inertia-gravity wave.

To see this, we express the dispersion relations in dimensionless form. The dispersion relation (1.21) of hydrostatic inertia-gravity wave expressed in a dimensionless form is

$$\left(\frac{\omega}{f}\right)^2 = 1 + \left(\frac{Nm^{-1}}{f}\right)^2 k_H^2 \tag{1.22}$$

where $k_H = \sqrt{k^2 + l^2}$. The dispersion relation of rotating shallow-water gravity

wave (1.14) written in dimensionless form is

$$\left(\frac{\omega}{f}\right)^2 = 1 + \left(\frac{\sqrt{gh_r}}{f}\right)^2 |\mathbf{k}|^2 \qquad (1.23)$$

The similarities indicated by (1.22) and (1.23) implies that it may be possible to define a rotating shallow-water equivalent of a hydrostatic inertia-gravity wave.

One such possibility is that the equivalent shallow-water gravity wave could have the same frequency and horizontal wave number as the inertia-gravity wave provided

$$\sqrt{gh_r} = N/m. \qquad (1.24)$$

Condition (1.24) also implies that their horizontal phase speed becomes identical. The expression for the horizontal phase speeds are

$$c_H^2 = \frac{\omega^2}{k_H^2} = \frac{N^2}{m^2} + \frac{f^2}{k_H^2}$$

and

$$c_R^2 = gh_r + \frac{f^2}{k_H^2},$$

respectively. Furthermore, their horizontal group velocities also become identical. The horizontal group velocity c_{gH} of the hydrostatic inertia-gravity waves is (Gill, 1982)

$$c_{gH} \approx \frac{N^2\alpha}{m\sqrt{(f^2 + N^2\alpha^2)}} = \left(\frac{N^2}{m^2}\right)\frac{1}{\sqrt{(f^2/k_H^2 + N^2/m^2)}}$$

where $\alpha = k_H/m \ (\ll 1)$, which is a ratio of vertical to horizontal scale is the aspect

ratio, and the horizontal group velocity c_g of rotating shallow-water gravity is

$$c_g \;\; = \;\; \frac{\partial \nu}{\partial k_H} = \frac{gh_r}{\sqrt{(f^2/k_H^2 + (gh_r))}}$$

(1.25)

Shallow-water waves, unlike inertia-gravity waves, do not propagate vertically. However, some justifications to the use of shallow-water equations can be made, when one considers the vertical propagation characteristics of inertia-gravity waves. The vertical group velocity of the hydrostatic inertia-gravity wave c_{gz} is given approximately by (Gill, 1982)

$$c_{gz} \approx \frac{-N^2 k_H^2}{m^2 \sqrt{(f^2 m^2 + N^2 k_H^2)}} = \frac{-N^2 \alpha^2}{m \sqrt{(f^2 + N^2 \alpha^2)}}$$

So, for example, if N is 10^{-2} s^{-1} and k_H^{-1} is 30 km, the waves with vertical scale $m^{-1} = 1$ km would have group velocity of 0.3 m s^{-1} (26 km per day), whereas waves with $m^{-1} = 100$ m would have a frequency only about 5% above inertial and a vertical group velocity of only 1 mm s^{-1} (86 m per day). Therefore, as long as the aspect ratio for inertia-gravity wave $\alpha \ll 1$, an equivalent shallow-water wave can be useful in representing hydrostatic inertia-gravity waves.

In conclusion, it must be stated that regardless of the resemblance in the dispersion relations indicated by expressions (1.22) and (1.23), shallow-water gravity waves are completely different from inertia-gravity waves. Shallow-water waves are interfacial waves, and only under special circumstances, such as when there exists a jump in stratification or density, one can expect shallow-water like waves to be of significance.

24

1.3.11 Froude number, Richardson number and stratification

Generally, in studies of fluid mechanics, the *Froude number* F is defined as the ratio of inertia force to pressure gradient force. Froude number then determines whether the subsequent motion will be dominated either by inertia or pressure gradient force. In the case of shallow incompressible fluid flows with a free surface, the Froude number can also be expressed as ratio of flow velocity to shallow-water gravity wave speed. Defined in this sense, the Froude number is the incompressible analogue of the *Mach number* for compressible flows, which is defined as ratio of velocity of air to speed of sound. Analogous to compressible fluids, flows with Froude number less than one are known as *sub-critical* and greater than one is known as *super-critical*. This implies that shallow-water equations permit the formation of shock waves which are known as hydraulic jumps. Consequently, shallow-water equations are also frequently used as a prototype model for demonstrating the hydraulic effects associated with wind flows over topography (see e.g., Baines 1998).

In the case of our atmosphere, the Froude number is often used as a measure of stratification. In what follows, we will now demonstrate the significance of the Froude number to stratification. First, consider the case of an air parcel moving horizontally with speed U in an unstratified environment. The parcel, upon approaching a ridge begins to move uphill. So the parcel does work against gravity, and will begin to lose its kinetic energy ($\rho U^2/2$, where ρ is the density of parcel) as it gains height. If the compressibility effects following the motion of the air parcel can be ignored, then conservation of mass implies that the ascent of the parcel must be accompanied by descent of an equal amount of fluid from above. Such an exchange of fluid renders the potential energy of the environment

unaltered. Now consider an identical case, but when the environment is stably stratified. Just as in the unstratified case, the ascending parcel gains potential energy at the expense of its kinetic energy, and the descending parcel loses potential energy. However, this time, the exchange of fluid has resulted in an increase of potential energy of the environment because of the change in density with height. and this increase in potential energy must have come at the expense of the initial kinetic energy of the parcel. (see e.g., Cushman-Roisin and Beckers 2010)

If ρ is the density of the parcel, then its initial kinetic energy is $\rho U^2/2$. The gain in potential energy by the environment is $\Delta \rho g H$, where $\Delta \rho$ is the scale of the density variation across height H. Then the ratio of available kinetic energy to the gain in potential energy is $\rho U^2/2\Delta \rho g H$. This ratio determines whether the kinetic energy carried by the parcel is sufficient to overcome the effect of stratification and disturb the equilibrium of the environment. The ratio can equivalently be written as $U^2/g'H$, where we have replaced g with reduced gravity $g' = (\Delta \rho g/\rho)$ and neglected the factor of one-half. This ratio can be identified as a square of the Froude number F, i.e.,

$$F^2 = \left(\frac{U}{\sqrt{g'H}} \right)^2, \tag{1.26}$$

where g' ($= \Delta \rho g/\rho$) is now the *reduced-gravity*, and $\sqrt{g'H}$ can be identified as the phase speed of non-rotating shallow-water gravity wave propagating in a fluid of depth H with acceleration due to gravity equal to g'. We showed earlier in (1.3.7) that the shallow-water equivalent phase speed of a stratified fluid can be determined by the expression, $\sqrt{g'H} = NH$.

Then (1.26) becomes

$$F = \frac{U}{NH}, \tag{1.27}$$

which indicates that Froude number can also be used as a measure of stratification. Therefore the stronger the stratification (i.e, larger the value of N), the smaller

the Froude number. Using typical value of $N = .01$ s^{-1} and $H = 10$ km as the typical depth of troposphere gives NH $(= \sqrt{g'H}) = 100$ m/s. For mid-latitude synoptic scale disturbances $U \approx 10$ m/s, and we get $F = 0.1$.

Another non-dimensional parameter which is commonly used instead of Froude number is known as *Richardson number Ri* (see e.g., Kundu 1990). It is defined as

$$Ri = \frac{N^2}{(\partial u/\partial z)^2} \tag{1.28}$$

where $\partial u/\partial z$ is the vertical wind shear . If U is the scale of the wind speed variation across height H, then we get

$$Ri = \left(\frac{NH}{U}\right)^2 = \frac{1}{F^2} \tag{1.29}$$

In the remainder of the thesis, since Ri and F^2 are equivalent, we will use the Froude number instead of the Richardson number for purposes of discussion.

1.3.12 Summary

This chapter introduced some fundamental concepts that are important in studying geophysical fluid dynamics. This was mainly done with the use of the shallow-water equations, because they are the simplest sets of equations that can be used to study atmospheric flows. In addition to their simplicity, these equations possesses important properties, such as their ability to represent both vortical and divergent fluid motions, both of which are present in the atmosphere.

Large-scale atmospheric motions are dominated by the action of the Coriolis force, and vertical fluid motions are closely approximated by hydrostatic

balance. The fact that shallow-water equations include both height gradients and Coriolis forces, and are derived under the assumption of hydrostatic balance makes them particularly useful for studying synoptic scale motions. Furthermore, shallow-water equations conserve potential vorticity, which can be considered as the shallow-water analogue of the atmospheric potential vorticity.

One of the limitations of shallow-water equations in studying atmospheric and oceanic fluid motions is its lack of stratification. A continuously stratified fluid such as our atmosphere permits the propagation of internal gravity waves, whereas shallow-water gravity waves are interfacial waves. Nevertheless, for the purpose of this thesis, the important properties that the shallow-water equations share with our atmosphere makes them a valuable tool for studying the wave emission mechanism associated with vortical motions.

This chapter has thus provided a brief introduction to geophysical fluid dynamics, and also provided the necessary foundations for understanding the more advanced topics to be dealt in the remainder the thesis.

Chapter 2

Lighthill's (1952) theory and Ford's (1994) extension

2.1   Introduction

In an effort to extend Lighthill's (1952) formulation of the aerodynamic sound generation problem to meteorologically significant fluid motions, Norton (see page 117 of Ford 1994a; Ford et al. 2000) used the rotating shallow-water equations to derive the following equation:

$$\left(\partial_{tt}^2 + f^2 - c^2\nabla^2\right)\partial_t h = \partial_{ij}^2 T_{ij} \tag{2.1}$$

where

$$T_{ij} = \partial_t(hu_iu_j) + \frac{1}{2}f(\epsilon_{ik}hu_ju_k + \epsilon_{jk}hu_iu_k) + \frac{1}{2}g\partial_t(h-h_r)^2\delta_{ij}, \tag{2.2}$$

$c\,(=\sqrt{gh_r})$ is the non-rotating shallow-water gravity wave speed in an undisturbed medium with height h_r, g is the acceleration due to gravity, and ϵ_{ij} is the two-

29

dimensional anti-symmetric tensor of rank two and unit determinant, such that, ϵ_{11} = $\epsilon_{22} = 0$, $\epsilon_{12} = -\epsilon_{21} = 1$. In equation (2.1) terms on the left hand side represent a linear rotating shallow-water gravity wave equation and therefore describe the propagation of a wave through an undisturbed medium, and the terms on the right hand side are regarded as wave forcing terms.

Lighthill's (1952) ideas were originally developed using the compressible gas equations, but for purposes of application to atmospheric and oceanic flows, we will follow Ford (1994a) by discussing Lighthill's (1952) ideas using the shallow-water equations. The non-rotating shallow-water equations are equivalent to the two-dimensional adiabatic gas equations. Just as acoustic waves are compressible waves, so are shallow-water gravity waves. Furthermore, shallow-water equations are the simplest set of equations that can be used to study both the vortical and gravity wave aspect of atmospheric fluid motions. Although, acoustic waves are permitted in our atmosphere, their amplitudes are generally considered unimportant relative to meteorologically significant motions.

In this chapter, we revisit Lighthill's (1952) formulation of the problem of aerodynamic sound generation using the shallow-water equations. The purpose is to highlight the idea behind Lighthill's (1952) formulation. The shallow-water equations, unlike the compressible gas equations, materially conserve nonlinear potential vorticity. However, as we shall see, this does not fundamentally affect Lighthill's formulation, because 1) in common with sound waves, the motion of small-amplitude non-rotating shallow-water gravity waves is also governed by conservation of vorticity, and not *linear* potential vorticity, and 2) the forcing functions are of the same nature.

We then discuss the extension of Lighthill's (1952) formulation to rotating shallow-water flows, i.e., we discuss in detail the derivation of the wave equation

(2.1). The details of the derivation have not been provided by Ford (1994a), and have only been sketched in a few lines by Ford et al. (2000).

It is our aim to highlight that the presence of background or planetary vorticity introduces important differences when Lighthill's formulation is extended to rotating shallow-water flows, and they require justification.

Lastly, Ford (1994a), based on his study, concluded that the effect of planetary vorticity introduces a cutoff frequency that severely inhibits gravity wave emission even for vortices of order one Rossby number (see page 99-101, Ford 1994a). These Rossby number order one vortices had size very small compared to the Rossby radius. Further investigation into the effects of rotation are warranted and will be carried out in this chapter as well as chapter 4.

The remainder of this chapter is organised as follows: In section (2.2), the basis of Lighthill's formulation of wave emission problem is reviewed. Lighthill's formulation is presented using the non-rotating shallow-water equations. This is followed by discussion of extension of Lighthill's (1952) ideas to rotating shallow-water fluid system or, equivalently, Ford's (1994) formulation in section (2.3). Finally in section (2.4) we summarize and make some concluding remarks.

2.2 Lighthill (1952)'s formulation adapted to non-rotating shallow-water equations

The central idea in Lighthill's (1952) theory of aerodynamic sound generation is to formulate the problem of wave emission associated with fluctuating fluid motions in a manner analogous to studies in linear acoustics. In studies of linear acoustics, the focus is on determining the properties of linear acoustic waves propagating through

an undisturbed acoustic medium forced by some prescribed external source field.

The problem of aerodynamic sound generation then reduces to identifying a suitable wave forcing function which can be associated with the actual fluctuations in fluid motion. Once this is done, it can used to study the response of an undisturbed fluid to this hypothetical forcing function (see section 2, Lighthill 1952).

We now discuss the shallow-water analogue of Lighthill's (1952) theory of aerodynamic sound generation. Lighthill's (1952) ideas can be readily extended to the non-rotating shallow-water equations. The first step in Lighthill's formulation is to express the momentum equations in flux form.

The non-rotating shallow-water equations (1.2) - (1.3), which govern the motion of a shallow layer of an incompressible fluid with a free surface, when written in tensor notation, read as

$$\partial_t u_i + u_j \partial_j u_i + \partial_i(gh) = 0 \tag{2.3}$$

$$\partial_t h + \partial_j(hu_j) = 0 \tag{2.4}$$

where Einstein summation convention has been used, i.e., a summation over the repeated index is implied, although the summation sign is not explicitly written. The subscripts i and j take on values 1 and 2, where 1 and 2 corresponds to coordinates x and y, respectively. Equations (2.3) are the horizontal momentum equations in Cartesian coordinates, and equation (2.4) is the continuity equation.

Multiplying the momentum equations (2.3) by h, and expressing the advective term $u_j \partial_j u_i$ in flux form, we get

$$h\partial_t u_i + \partial_j(hu_iu_j) - u_i\partial_j(hu_j) + h\partial_i(gh) = 0. \tag{2.5}$$

32

Then multiplying the continuity equation (2.4) by u_i, and adding to the last equation we get

$$\underbrace{\partial_t(hu_i)}_{\substack{\text{Rate of change of i}^\text{th} \\ \text{component of momentum of a column} \\ \text{of fluid per unit area}}} = \underbrace{-\partial_j\left(hu_iu_j + \frac{gh^2}{2}\delta_{ij}\right)}_{\substack{\text{Divergence of i}^\text{th}\text{ component of momentum flux} \\ \text{of fluid column of unit area}}} \qquad (2.6)$$

where δ_{ij} is the Kronecker delta ($= 1$ for $i = j$, and 0 for $i \neq j$). This equation represents the shallow-water analogue of the flux form of the compressible gas equations. Equation (2.6) governs the motion of a column of fluid of unit area of height h, whereas the flux form of the compressible gas equations describe the motion of a unit volume of fluid. These differences arise because fluid convergence produces change in density in the case of compressible fluid, and in the case of shallow-water motion, horizontal convergence produces change in the local height which appear as ripples on the surface, as density is assumed constant. Nevertheless, the last equation can be interpreted in a manner analogous to the one provided by Lighthill (1952) (see also Lighthill 1978) for the compressible gas.

Equation (2.6) expresses that idea that the rate of change of ith component of momentum of a column of fluid of unit area changes due to the combined effect of

1. divergence of ith component of momentum flux (hu_iu_j), which arises as a consequence of fluctuations in Reynolds stresses.

2. divergence of ith-momentum flux $(gh^2/2\delta_{ij})$, which arises as a consequence of fluctuations in hydrostatic pressure or normal stresses. Viscous stresses make no contribution because viscosity has been neglected in our study.

Since the pressure fluctuations associated with the passage of a linear shallow-water wave arise due to gradients in the hydrostatic pressure field gh,

33

Lighthill's method suggests that the stress field F_{ij} responsible for forcing wave motion in a uniform medium at rest must be equal to the stress field in (2.6) minus the stress associated with the linear wave, i.e.,

$$F_{ij} = \left(hu_iu_j + gh^2/2\delta_{ij} - c^2h\delta_{ij} \right). \tag{2.7}$$

Then the non-rotating shallow-water analogue of Lighthill's (1952) acoustic analogy is equivalent to stating that the momentum equation governing the fluid motions under the influence of an externally imposed hypothetical stress field F_{ij} can be written as

$$\partial_t(hu_i) + c^2\partial_i h \;=\; -\partial_j\left(hu_iu_j + \frac{gh^2}{2}\delta_{ij} - c^2h\delta_{ij} \right) \tag{2.8}$$

$$\;=\; -\partial_j F_{ij} \tag{2.9}$$

Then the forced wave equation can be derived by taking ∂_i of (2.9) to get

$$\partial_t(\partial_i hu_i) + c^2\nabla^2 h \;=\; -\partial_{ij}^2 F_{ij} \tag{2.10}$$

and then using the continuity equation (2.4) to substitute $(\partial_i hu_i)$ by $-(\partial_t h)$ in (2.10) to get

$$\partial_{tt}^2 h - c^2\nabla^2 h \;=\; \partial_{ij}^2 F_{ij}$$

$$\;\equiv\; q[\mathbf{x}, t] \tag{2.11}$$

This is the shallow-water analogue of Lighthill's (1952) forced wave equation. The terms on right hand side of equation (2.11) describe the wave forcing terms and the terms on left hand side of (2.11) describes the propagation of the forced wave through an undisturbed medium.

34

2.2.1 Solution of Lighthill's equation

Since (2.11) represents a non-homogeneous equation, the Green's function technique can be applied to obtain the solution. The general expression for a Green's function solution of the (2.11) takes the form

$$h[\mathbf{x}, t] = \int_{space} \int_{time} q[\mathbf{x}', t'] G[\mathbf{x} - \mathbf{x}', t - t'] d\mathbf{x}' dt', \tag{2.12}$$

where $G[\mathbf{x}, t]$ represents a suitable Green's function.

In order to determine the wave field, the first step is to determine the Green's function G. Then one also has to know how the forcing function $q[\mathbf{x}, t]$ varies both spatially and temporally. Note that $q[\mathbf{x}, t]$ depends on both velocity $\mathbf{v}[\mathbf{x}, t]$ and height field $h[\mathbf{x}, t]$, which implies that the flow field generating the forcing has to be known before the wave field can be computed. This constraint, as will be investigated and discussed further in later chapters, has consequences with respect to investigating the details of the wave forcing mechanism when using a Lighthill-like formulation.

2.3 Extension of Lighthill's ideas to rotating fluids: Ford's formulation

Lighthill (1952) formulated the problem of aerodynamic sound emission in a non-rotating or *inertial* frame of reference, since the effects of planetary vorticity may be neglected for sound waves, and sound waves tend to have short wavelengths and high frequencies. Extending Lighthill's (1952) ideas to rotating fluid implies that

1. the governing equations have to be reconsidered with respect to a rotating or *non-inertial* frame of reference,

2. the effect of background rotation or planetary vorticity have to be taken into consideration.

We now review Ford's (1994) extension of Lighthill's (1952) theory to rotating flows. The details of the formulation have only been briefly sketched by Ford et al. (2000), hence we will discuss the detail of the steps that led to the derivation of equation (2.1).

Reconsidering the problem of wave emission from a *non-inertial* frame of reference does not affect the formulation, but the presence of background or planetary vorticity does introduce new effects, which were not considered by Lighthill (1952).

It it important to remember that the Coriolis force is an *apparent* force that arises as a consequence of using the *non-inertial* frame of reference. The expression for Coriolis force is

$$f\hat{\mathbf{k}} \times \mathbf{v}, \tag{2.13}$$

where f $(= 2\Omega \sin \phi)$ is known as a *Coriolis parameter*, because it determines the rate of rotation of the frame of reference about its local vertical. But, f is also equal to the planetary vorticity. Note that both the planetary vorticity and Coriolis parameter vary with latitude. Along the equator, $f = 0$, so planetary vorticity there is zero and the *non-inertial* frame of reference does not rotate about its local vertical, but only translates along the equator.

So we are interested in knowing to what extent Lighthill's formulation is affected by the presence of background or planetary vorticity, and more impor-

36

tantly, does it affect the process of wave emission. Ford (1994a), based on his study, concluded that the effect of planetary vorticity is to inhibit gravity wave emission due to the cutoff frequency f below which waves can't propagate. In what follows, we will carry out a more thorough investigation of the effects of rotation on wave emission.

When viewed from a *non-inertial* or rotating frame of reference the shallow-water equations take the form

$$\partial_t u_i + u_j \partial_j u_i + f\epsilon_{i3j} u_j + \partial_i(gh) = 0 \tag{2.14}$$

$$\partial_t h + \partial_j(hu_j) = 0 \tag{2.15}$$

where f $(= 2\Omega \sin\phi)$ is known as Coriolis parameter (assumed to be constant in this study), Ω is the angular velocity of rotation of the earth, ϕ is latitude, and ϵ_{ijk} is the *permutation symbol* or *alternating tensor*[1].

As in the non-rotating case, first we express the conservation of momentum in flux form. Multiplying the momentum equations (2.14) by h, and then making use of the continuity equation (2.15), we get the momentum equations in flux form

$$\underbrace{\partial_t(hu_i)}_{\substack{\text{Rate of change of i}^{\text{th}} \\ \textit{component of } \text{momentum of a column} \\ \text{of fluid per unit area}}} + \underbrace{f\epsilon_{i3j}hu_j}_{\text{Coriolis force}} = \underbrace{-\partial_j\left(hu_iu_j + g\frac{h^2}{2}\delta_{ij}\right)}_{\substack{\text{Divergence of i}^{\text{th}} \text{ component of momentum flux} \\ \text{of fluid column of unit area}}} \tag{2.17}$$

The terms on the right hand side of this equation can be interpreted in the same fashion as we did in the non-rotating case, but this time there arises an additional term, the Coriolis force $f\epsilon_{i3j}hu_j$, as a consequence of the *non-inertial* frame of

[1]The *permutation symbol* or *alternating tensor* is defined as

$$\epsilon_{ijk} = \begin{cases} 1 & \text{if } ijk = 123, 231, \text{or } 312 \text{ (cyclic order)}, \\ 0 & \text{if any two indices are equal}, \\ -1 & \text{if } ijk = 321, \ 213, \text{ or } 132 \text{ (anticyclic order)} \end{cases} \tag{2.16}$$

reference.

Then, we continue as in the non-rotating case, i.e., apply Lighthill's *acoustic analogy*, which is equivalent to rewriting (2.17) as

$$\partial_t(hu_i) + f\epsilon_{i3j}hu_j + c^2\partial_i h = -\partial_j\left(hu_iu_j + g\frac{h^2}{2}\delta_{ij} - c^2h\delta_{ij}\right). \quad (2.18)$$

This expression can be interpreted as in the non-rotating case with the inclusion of the Coriolis force.

Then in order to derive the forced wave equation, we take the divergence of (2.18), and then use the continuity equation to replace $\partial_j(hu_j)$ by $-(\partial_t h)$, to get

$$\partial_{tt}^2 h - f\epsilon_{i3j}\partial_i hu_j - c^2\nabla^2 h = \partial_{ij}\left(hu_iu_j + gh^2/2\delta_{ij} - c^2h\delta_{ij}\right) \quad (2.19)$$

Unlike the non-rotating case, the left hand side of the last equation does not represent a linear wave operator because of the presence of the term $f\epsilon_{i3j}\partial_i hu_j$. Since $-\epsilon_{i3j} = \epsilon_{3ij}$, the term $f\epsilon_{i3j}\partial_i hu_j$ can be identified as the vertical component of the curl of the fluid momentum hu_j times the factor f.

The term containing vorticity arises in the wave equation for h because when $f \neq 0$ small-amplitude height fluctuations associated with small-amplitude gravity waves induce vorticity fluctuations through vortex stretching[2] This cou-

---

[2]Note that vortex stretching occurs in the nonlinear shallow-water equations whether rotation is present or not, i.e.,

$$\frac{d}{dt}(\zeta + f) = -(\zeta + f)\nabla \cdot \mathbf{v} \quad (2.20)$$

Linearizing this equation yields

$$\frac{\partial \zeta'}{\partial t} = -f\nabla \cdot \mathbf{v}', \quad (2.21)$$

where the primed variable indicate small amplitude fluctuations. So vortex stretching cannot occur for linear shallow-water waves when $f = 0$.

pling arises due to the presence of the background or planetary vorticity f, and is indicated by the conservation of a scalar quantity known as the *linear* potential vorticity.

The coupling becomes more evident when we consider the linearized version of the forced equation, i.e., when we consider the case of a propagation of small-amplitude wave through an undisturbed medium far from the source region. The linearized equation is

$$\partial_{tt}^2 h' + h_r f \zeta' - g h_r \nabla^2 h' = 0 \qquad (2.22)$$

where ζ' $(= \epsilon_{3ij} \partial_i u'_j)$ is the relative vertical vorticity. The relation between the vorticity fluctuation ζ' and height fluctuation h' is provided by conservation of linear potential vorticity η', which can be expressed as

$$\partial_t \eta' = 0 \qquad (2.23)$$

where $\eta' = (\zeta' - fh'/h_r)$, where primed variables indicate the deviation from the undisturbed basic state at time t.

If the medium is initially undisturbed, then both vorticity fluctuation ζ' and height fluctuation h' are zero, initially. Then, the relative vorticity fluctuation ζ' at a later time t can be computed from (2.23) and $\eta'(\text{t=0}) = 0$, yielding

$$\zeta' = fh'/h_r. \qquad (2.24)$$

Substituting for ζ' in (2.22) we get

$$\partial_{tt}^2 h' + f^2 h' - g h_r \nabla^2 h' = 0, \qquad (2.25)$$

where we have used $\partial_t h_r = 0$ and $\nabla^2 h_r = 0$. We note here that equation (2.25) represents a linear rotating shallow-water wave equation for h', but not for h ($= h_r + h'$). This problem arises because, unlike the *linear* non-rotating shallow-water equations, the linear rotating shallow-water equations contain three modes: two propagating shallow-water gravity waves ($\omega = \pm\sqrt{f^2 + gh_r k^2}$) and one steady geostrophic mode ($\omega = 0$).

Now returning back to (2.19), in order to express vorticity fluctuations in terms of the height fluctuations, we take the time derivative of (2.19) to obtain

$$\partial_{tt}^2(\partial_t h) + f\partial_t(\epsilon_{3ij}\partial_i h u_j)$$
$$-gh_r\nabla^2(\partial_t h) = \partial_{ij}^2\partial_t\left(hu_i u_j + gh^2/2\delta_{ij} - c^2 h\delta_{ij}\right) \qquad (2.26)$$

The expression for local fluctuation of vorticity of a fluid column $\partial_t(\epsilon_{3ij}\partial_i h u_j)$ can obtained by taking the vertical component of the curl of (2.17), which is

$$\partial_t(\epsilon_{3ij}\partial_i h u_j) = -\underbrace{\partial_i(fhu_i)}_{A} - \underbrace{\epsilon_{3ki}\partial_k(\partial_j hu_i u_j)}_{B} \qquad (2.27)$$

where term A indicates the rate of change of vorticity produced by stretching of the planetary vorticity f, and term B indicates the rate of production of vorticity associated with nonlinear interactions, such as the fluctuations in the vorticity field associated with velocity field u_i produced by convergence of ith-momentum flux $\partial_j(hu_i u_j)$.

Since the continuity equation can be used to replace $\partial_i(hu_i)$ by $-(\partial_t h)$ in (2.27), we obtain

$$\partial_t(\epsilon_{3ij}\partial_i h u_j) = \underbrace{f(\partial_t h)}_{A} - \underbrace{\epsilon_{3ki}\partial_k(\partial_j hu_i u_j)}_{B}, \qquad (2.28)$$

40

which assures that the fluid motions conserve *linear* potential vorticity in regions where the nonlinear interaction (term B) can be neglected. In regions where nonlinear interactions cannot be neglected, both the terms A and B contribute to the production of vorticity, and the flow is determined by conservation of nonlinear potential vorticity. It is yet to be determined how significant is the contribution of term A when the flow considered has Rossby number order one, for it would imply planetary vorticity has a significant effect even when nonlinear interactions become important.

Substituting for $\partial_t(\epsilon_{3ij}\partial_i h u_j)$ in (2.26), we get

$$\partial_{tt}^2(\partial_t h) + f\left[\underbrace{f(\partial_t h)}_{A} - \underbrace{\epsilon_{3jk}\partial_j(\partial_l h u_k u_l)}_{B}\right] - gh_r\nabla^2(\partial_t h)$$
$$= \partial_{ij}^2\partial_t\left(hu_i u_j + g\frac{h^2}{2}\delta_{ij} - c^2 h\delta_{ij}\right) \tag{2.29}$$

Ford (1994a) (see also Ford et al. 2000), now transfer term B which is quadratic in u_i to the *rhs*, while term A, which is linear in u_i, is retained on the *lhs* to obtain

$$\left(\partial_{tt}^2 + f^2 - gh_r\nabla^2\right)\partial_t h = \partial_{ij}^2\partial_t\left(hu_i u_j + g\frac{h^2}{2}\delta_{ij} - c^2 h\delta_{ij}\right)$$
$$+f\epsilon_{3jk}\partial_j(\partial_l h u_k u_l),$$
$$= \partial_{ij}^2\left(\partial_t(hu_i u_j) + \frac{g}{2}\partial_t(h - h_r)^2\delta_{ij}\right)$$
$$+\partial_{jl}^2(f\epsilon_{3jk}h u_k u_l) \tag{2.30}$$

where we have used $\partial_t h_r = 0$. Furthermore, since it can be shown that both the terms: $\partial_{jl}^2(f\epsilon_{3jk}h u_k u_l)$ in equation (2.30) and $\partial_{ij}^2 f(\epsilon_{ik}h u_j u_k + \epsilon_{jk}h u_i u_k)/2$ in equations (2.1) and (2.2), reduce to the same expression,

$$f\left(\partial_{11}^2(hu_1 u_2) - \partial_{22}^2(hu_1 u_2) + \partial_{12}^2(hu_2 u_2) - \partial_{12}^2(hu_1 u_1)\right), \tag{2.31}$$

proves that the non-homogeneous wave equation (2.30) is equivalent to the Ford-Lighthill equation (2.1).

The effects of rotation have been split into a familiar term that affects wave propagation and an unfamiliar term that affects wave forcing. Those authors did not consider whether the term $f\epsilon_{3jk}\partial_j(\partial_l h u_k u_l)$ adds to forcing provided by other non-linear terms: $\partial_{ij}^2\partial_t(h u_i u_j)$ and $\partial_{ij}^2 g h^2/2\delta_{ij}$, or whether it acts in opposition to them. A determination of the effect of this term of this will be provided in chapter (4), when we investigate the contribution of this term to wave forcing.

2.4   Summary and concluding remarks

In this chapter, the basis of Lighthill's (1952) formulation of the problem of aerodynamic sound generation was discussed using the shallow-water equations. The interpretation of the problem of wave generation as Lighthill's acoustic analogy was reviewed. No fundamental differences arise when the formulation is repeated using the non-rotating shallow-water equations, because both the small-amplitude non-rotating shallow-water gravity waves and sound waves are governed by conservation of vorticity, and the nature of the wave forcing remains the same.

We then reviewed the details of the Ford's (1994) extension of Lighthill's formulation to rotating shallow-water flows, since important details of the derivation have not been provided in the literature. Important differences arise in the formulation due to the presence of background or planetary vorticity, which makes the formulation less straight forward than in the non-rotating case.

Contrary to the non-rotating case, linear rotating shallow-water gravity waves conserve *linear* potential vorticity due the presence of background vorticity. Consequently, even small-amplitude height fluctuations disturb the background

vorticity. Our study also showed that since the linear rotating shallow-water equations consist of three modes: two gravity wave modes and one steady geostrophic mode, the formulation is not as straight forward as in the non-rotating case.

Our study also highlighted some of the issues in interpreting the new terms that arise during the formulation, and will investigate these issues further in Chapter 4.

Chapter 3

Simulation of gravity wave emission from vortical flows

3.1 Introduction

In the past decade or so, there has been a lot of interest shown in understanding the gravity wave emission mechanism associated with atmospheric jets. Consequently, we now have a much clearer picture of wave emission associated with atmospheric jets. However, studies on wave emission from barotropic vortices have been relatively few. In this chapter, we revisit the problem of gravity wave emission from rotating shallow-water barotropic vortices for the purpose of gaining a deeper understanding of the mechanism of gravity wave generation.

One of the difficulties related to the understanding of the gravity emission from vortices can be understood as follows: Physically divergence and vorticity are independent properties (see e.g., Aris 1989; Kundu 1990; Holton 2004). So the question arises, how are shallow-water gravity waves (which are divergent waves)

44

forced during the evolution of the vortices. The purpose of the chapter is to shed light on the physical mechanism through which a vortex may generate a wave-like divergence field.

Specifically, we revisit the problem considered by Ford (1994a). He performed simulations showing an unstable parallel flow rolling up into vortices and, in the process, emitting gravity waves in a constant f-plane shallow-water model. He also showed that the characteristics of these simulated waves agree well with that predicted by Ford's (1994a) modified version of Lighthill's (1952) theory of aerodynamic sound generation. Sugimoto et al. (2008) also studied shallow-water barotropic vortices using a constant f-plane shallow-water model. Harada and Ishioka (2011) used a two-layer constant f-plane shallow-water model to study the evolution of an unstable Bickley jet and the subsequent evolution of the shallow-water gravity waves.

The studies conducted by Ford (1994a) and Sugimoto et al. (2008) focused mainly on comparison of simulated wave with the Ford's (1994a) modified version of Lighthill's theory. But none of these past studies have sought a detailed answer to the question that has been raised above.

In addition to the above mentioned factors, our interest to revisit the problem considered by Ford (1994a) concerns the numerical errors and it's effect on the wave emission mechanism. Our study with resolution comparable to that used by Ford (1994a), to be discussed in section (3.4), will show that during the simulations oscillations develop on the leading edge of the advecting PV-front and extend to the trailing side. These oscillations arise as a consequence of nonlinear advection which compresses gradients and leads to insufficient resolution. We wish to investigate whether these oscillations can be reduced by varying model resolution and dissipation, and, more importantly, we are interested in knowing

whether the wave generation mechanism is sensitive to these errors. Also of interest are the characteristics of the emitted gravity waves associated with such a forcing. These and the above mentioned reasons strongly suggests that the wave generation mechanism from barotropic vortices needs to be reviewed in detail.

The remainder of this chapter is organized as follows: We start by performing simulations of gravity wave emission from an initially parallel, unstable flow using a constant f-plane shallow-water model. The details of the constant f-plane shallow-water model are provided in section (3.2). The details of the simulation are provided in section (3.3) and the results discussed in section (3.4). The sensitivity of the simulation results in regard to resolution and dissipation, and it's implications to the wave generation mechanism are discussed in section (3.5). Finally, in section (3.6) we make some concluding remarks.

3.2   Shallow-water Model

3.2.1   Introduction

The inviscid constant f-plane shallow-water equations in Cartesian co-ordinates are

$$\partial_t u + u\partial_x u + v\partial_y u - fv + g\partial_x h = 0 \tag{3.1}$$

$$\partial_t v + u\partial_x v + v\partial_y v + fu + g\partial_x h = 0 \tag{3.2}$$

$$\partial_t h + \partial_x(uh) + \partial_y(vh) = 0 \tag{3.3}$$

where x and y are horizontal Cartesian co-ordinates, u and v are the horizontal velocities in the x and y-direction, respectively, h is the height of the free surface, g is the acceleration due to gravity, f ($= 2\Omega \sin \phi$) is the Coriolis parameter,

where Ω is the angular velocity of rotation of the earth and ϕ is the latitude.

The numerical scheme used to discretize the above shallow-water equations is the well-known potential-enstrophy conserving scheme of Sadourny (1975) (see also Washington and Parkinson 1986). This is a second-order finite-difference scheme. Before this scheme is implemented, the governing equations are transformed to a suitable form. The steps taken to derive this form are as follows: Adding $((\partial_x v - \partial_y u - \zeta)v)$ to (3.1) and subtracting $(\partial_x v - \partial_y u - \zeta)\, u$ to (3.2), we get

$$\partial_t u + u \partial_x u + v \partial_y u + (\partial_x v - \partial_y u)v - (\zeta + f)v + g \partial_x h = 0, \tag{3.4}$$

$$\partial_t v + u \partial_x v + v \partial_y v - (\partial_x v - \partial_y u)\, u + (\zeta + f)u + g \partial_x h = 0. \tag{3.5}$$

where $\zeta = (\partial_x v - \partial_y u)$ is the relative vorticity. Rearranging the terms we get

$$\partial_t u - (\zeta + f)v + \partial_x \left(\frac{u^2 + v^2}{2} + gh \right) = 0, \tag{3.6}$$

$$\partial_t v + (\zeta + f)u + \partial_y \left(\frac{u^2 + v^2}{2} + gh \right) = 0. \tag{3.7}$$

We now express the second terms in (3.6) and (3.7) in terms of *potential vorticity* (η) by dividing and multiplying the second terms by h. The resulting equations become

$$\partial_t u - \eta V + \partial_x B = 0, \tag{3.8}$$

$$\partial_t v + \eta U + \partial_y B = 0, \tag{3.9}$$

and the continuity equation (3.3) can be written as

$$\partial_t h + \partial_x U + \partial_y V = 0, \tag{3.10}$$

where

$$\eta = \frac{(\zeta + f)}{h} \tag{3.11}$$

is the *potential vorticity*,

$$U \;=\; hu \qquad and \qquad V \;=\; hv \tag{3.12}$$

are the mass fluxes, and

$$B = \frac{(u^2 + v^2)}{2} + gh \tag{3.13}$$

is the *Bernoulli function*. The shallow-water equations (3.8 - 3.10) expressed in this form are now suitable for discretization using Sadourny's scheme.

3.2.2 Sadourny (1975)'s scheme

The Sadourny's potential-enstrophy conserving scheme when applied to the shallow-water equations (3.8 - 3.10) reads as

$$\partial_t u - \overline{\eta}^y \overline{\overline{V}^x}^y + \delta_x B \;=\; 0 \tag{3.14}$$

$$\partial_t v + \overline{\eta}^x \overline{\overline{U}^x}^y + \delta_y B \;=\; 0 \tag{3.15}$$

$$\partial_t h + \delta_x U + \delta_y V \;=\; 0 \tag{3.16}$$

where the overbars represent second-order spatial averaging operator, and δ represents the second-order finite-difference operator, where subscripts x and y represents the direction of the derivatives. The averaging and the finite-difference
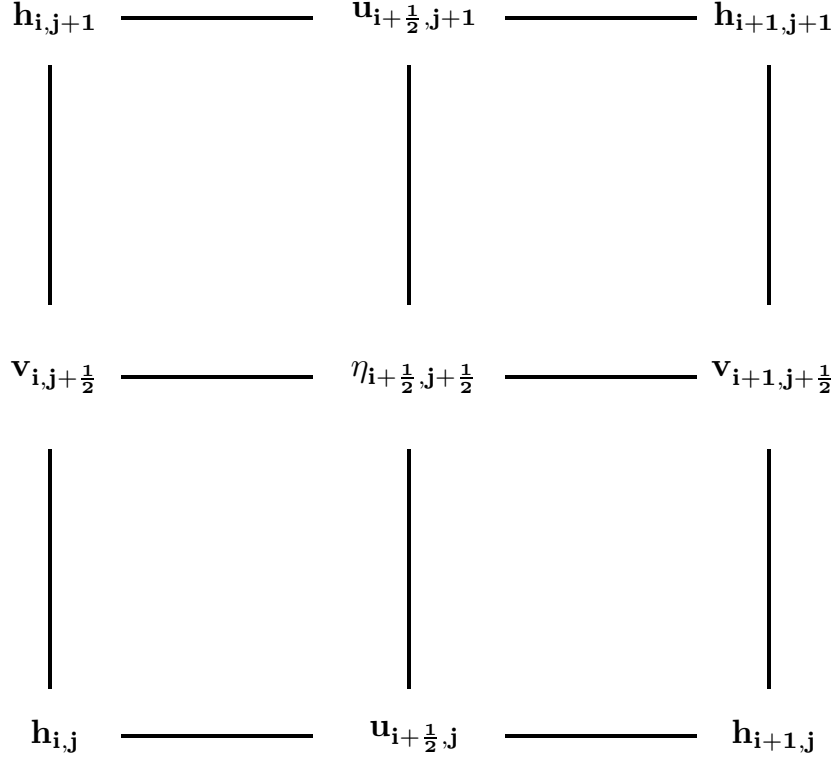
Figure 3.1: Figure shows the spatial disposition of the variables u, v, and h when using the Arakawa C-grid staggering, where the subscripts i and j represent grid-indices. Also shown is the location of the variable η.

operator are defined as follows:

$$\overline{a}^{x_i} = \frac{1}{2}\left(a[x_i + \frac{\Delta x_i}{2}] + a[x_i - \frac{\Delta x_i}{2}]\right) \tag{3.17}$$

$$\delta_{x_i}a = \frac{\left(a[x_i + \frac{\Delta x_i}{2}] - a[x - \frac{\Delta x_i}{2}]\right)}{\Delta x_i} \tag{3.18}$$

where x_i represents either x or y for $i = 1$ or 2, respectively, $a[x_i]$ represents an arbitrary variable a at a location x_i. The Arakawa C-grid is utilized for the spatial disposition of the variables u, v, and h (see fig. 3.1). The mass fluxes U and V

are evaluated at points where u and v are located, i.e.,

$$U = \overline{h}^x u, \tag{3.19}$$

$$V = \overline{h}^y v. \tag{3.20}$$

B is defined at points where h is located such that

$$B = gh + \frac{1}{2}(\overline{u^2}^x + \overline{v^2}^y). \tag{3.21}$$

Potential vorticity η is evaluated at the mesh centers as

$$\eta = \frac{\delta_x v - \delta_y u}{\overline{h}^{yx}}. \tag{3.22}$$

The model invariants are the total energy E, defined as

$$E = \sum \frac{1}{2}(gh^2 + h\overline{u^2}^x + h\overline{v^2}^y), \tag{3.23}$$

and absolute potential enstrophy Z, which is defined as

$$Z = \sum \frac{1}{2}\eta^2 \overline{h}^{yx}, \tag{3.24}$$

where the summation is carried over the entire domain, and

$$\sum a \equiv \sum_{ij} a_{ij}.$$

3.2.3   Time differencing

The time integration is Leap-frog with Robert-Asselin (Robert 1966; Asselin 1972) filtering to damp the computational mode associated with Leap-frog scheme. The

50

Robert-Asselin filter is implemented as follows: The Leap-frog time discretization when applied to the differential equation

$$\frac{ds}{dt} = F[s(t)], \tag{3.25}$$

where $F[s]$ is a some function of variable s, reads as

$$s[t + \Delta t] = s(t - \Delta t) + (2\Delta t)F[s(t)] \tag{3.26}$$

where $s[t - \Delta t]$, $s[t]$, and $s[t + \Delta t]$ indicates the value of s at time $(t - \Delta t)$, t and $(t + \Delta t)$, respectively. Then the filtering step is applied by updating the value of $s[t]$ before the next integration step as

$$s(t) = s(t) + \alpha \left[s(t - \Delta t) - 2s(t) + s(t + \Delta t) \right], \tag{3.27}$$

where α is the Robert-Asselin filtering coefficient. Note that setting $\alpha = 1/2$ reduces (3.27) to the mid-point averaging scheme. A filter parameter of $\alpha = 0.06$ is typically used in global atmospheric models. Values of $\alpha = 0.2$ are common in convective cloud models. For certain advection– diffusion problems, the recommended value is in the range 0.25–0.3. (see e.g., Durran 2010)

3.2.4   Model domain, boundary conditions, and Rayleigh damping layer

The model domain is rectangular in shape. The x-direction domain extends from $x = 0$ to $x = L_x$, where $L_x = (M-1)\Delta x$, M is the number of grid-points in the x-direction, and Δx is the grid spacing. Boundary conditions along the x-coordinate direction are periodic. In the y-direction, the domain extends from $y = -L_y$ to

$y = L_y$, where $L_y = 0.5(N - 1)\Delta y$, N is the total number of grid points in the y-direction, and Δy is the grid spacing. Fixed boundaries are implemented in the y-direction.

Two Rayleigh damping layers are implemented to prevent reflection of gravity waves from the fixed boundaries. The width of each damping layer is D ($= N_d \Delta y$, where N_d is the indical width of the damping layer). One layer extends from $y = $ -L_y to $y = (-L_y + D)$, and the other layer extends from $y = (L_y - D)$ to $y = L_y$.

The Rayleigh damping term takes the form $\tau_R(s - s_0)$, where τ_R is the damping coefficient, s represents the variable that is being damped, and s_0 represents the value of the variable s at the edge of the domain (see e.g., Durran 2010 and references therein). The damping coefficient τ_R takes the value zero when it first encounters the disturbance and then gradually increases and attains a maximum value at the edge of the domain. The maximum value of the damping coefficient is chosen such that $max(\tau_R)\Delta t \leq 1$ (see e.g., Durran 2010). Since the effectiveness of damping increases with the thickness of the damping layer, then by choosing sufficient number of grid points, layers of sufficient thickness can be utilized to effectively damp the disturbances even over a wide spectrum. The time integration of the damping term is performed using an *implicit* scheme for stability purposes. Since the time integration of the non-diffusive terms are performed using Leap-frog scheme, the backward time differencing when applied to the Rayleigh damping term reads as

$$\frac{s_n[t + \Delta t] - s_n[t - \Delta t]}{2\Delta t} = -\tau_R(s_n[t + \Delta t] - s_0) \qquad (3.28)$$

where n indicates the grid point index.

3.2.5 Model dissipation

Explicit sixth-order hyper-diffusion (∇^6) has been applied to remove grid-scale noise, where

$$\nabla^6 = \frac{\partial^6}{\partial x^6} + \frac{\partial^6}{\partial y^6}. \tag{3.29}$$

The sixth-order spatial derivative when approximated using the second-order finite difference scheme takes the form

$$\frac{1}{(\Delta x_i)^6} \left(s_{n+3} - 6s_{n+2} + 15s_{n+1} - 20s_n + 15s_{n-1} - 6s_{n-2} + s_{n-3} \right), \tag{3.30}$$

where s represents the variables u, v or h, and Δx_i represents Δx for $i = 1$ and Δy for $i = 2$, and n indicates the grid point index. The hyperdiffusion term is integrated *forward* in time.

Again, since the time integration of the non-diffusive terms are performed using Leap-frog scheme, the forward time integration when applied to the hyper-diffusion term (3.30) reads as

$$
\begin{aligned}
\frac{s_n[t + \Delta t] - s_n[t - \Delta t]}{2\Delta t} = \quad & \frac{\nu}{(\Delta x_i)^6} (s_{n+3}[t - \Delta t] \\
& -6s_{n+2}[t - \Delta t] + 15s_{n+1}[t - \Delta t] \\
& -20s_n[t - \Delta t] + 15s_{n-1}[t - \Delta t] \\
& -6s_{n-2}[t - \Delta t] + s_{n-3}[t - \Delta t])
\end{aligned} \tag{3.31}
$$

where ν is the diffusivity.

The dissipation e-folding time τ_e in the case of an explicit m^{th}-order deriva-

tive is

$$\tau_e^{-1} \;=\; \frac{\nu}{(\Delta x_i)^m} 2^{m/2} \left(1 - \cos k\Delta x_i\right)^{m/2} \tag{3.32}$$

where k is the wave number, m is the order of derivative (Durran 2010). In case of the grid-level noise, i.e., the $2\Delta x_i$-wave, we have $k = \pi/\Delta x_i$, so then (3.32) becomes

$$\tau_e^{-1} \;=\; \gamma 2^m \tag{3.33}$$

where $\gamma = \nu/(\Delta x_i)^m$.

The typical value of γ used in our simulations is $0.25{\times}10^{-4}$. Then grid-spacing (Δx_i) of 0.675 km, implies $\tau_e = 10.4$ min. The typical time-step (Δt) used in the simulations ranges from 5.6 s to 2 s. In order to facilitate comparison with Ford (1994a)'s results, nonuniform dissipation is applied only along the x and the y-direction. The dissipation coefficients along x and y-directions will then be referred to as ν_x and ν_y, respectively.

The inviscid shallow-water model with the addition of hyper-diffusion and the damping layer reads as

$$\partial_t u + \delta_x B - \overline{\eta}^y \overline{\overline{V}}^{xy} \;=\; -\tau_R(u - u_0) + \nu\nabla^6 u \tag{3.34}$$

$$\partial_t v + \delta_y B + \overline{\eta}^x \overline{\overline{U}}^{xy} \;=\; -\tau_R v + \nu\nabla^6 v \tag{3.35}$$

$$\partial_t h + \delta_x U + \delta_y V \;=\; -\tau_R(h - h_0) + \nu\nabla^6 h \tag{3.36}$$

where ν is the diffusivity, and u_0 and h_0 indicates the basic state velocity and height of the fluid.

3.3   Simulation Details

3.3.1   Introduction

It was realized long ago that one of the problems associated with studying mete-
orological phenomena with numerical models is that any imbalance in the initial
wind and pressure fields will begin to undergo oscillations, which results in the
emission of inertia-gravity waves (Rossby 1938; Cahn 1945; Blumen 1972). Such
waves generated during model initialization are referred to as *meteorological noise*
because the source of such waves, depending on the strength of the imbalance,
is often of an artificial or unphysical nature, primarily due to an insufficiently
accurate knowledge of the initial state.

Since our aim is to study the gravity wave generation mechanism associated
with the instability in a rotating fluid system, it is important to distinguish the
waves associated with initialization procedures, i.e., the noise, from the ones that
are of interest to our study. In the simulations considered, since the initial wind is
assumed to be a parallel flow, we are able to set the wind field to be in *geostrophic
balance* with the pressure field.

In the case of rotating shallow-water flows, the two dimensionless parame-
ters of significance are the Rossby number Ro and the Froude number F, where Ro
determines the effect of background rotation, and F indicates the effect of strati-
fication (see section (1.3.11)). Below, on the basis of scaling arguments, we show
how these non-dimensional parameters can be related to background rotation and
stratification in the case of the rotating shallow-water equations.

The rotating shallow-water momentum equations in vector form reads as

$$\frac{\partial \mathbf{v}}{\partial t} + \mathbf{v} \cdot \nabla \mathbf{v} - f\mathbf{k} \times \mathbf{v} = -g\nabla h. \tag{3.37}$$

Let U indicate the velocity scale, i.e., $|\mathbf{v}| \sim U$ and L indicate the length scale such that $|\nabla \mathbf{v}| \sim U/L$. Let Δh indicates the order of magnitude of height fluctuation across the distance L. Furthermore, we let the time scale T equal to the advective time scale L/U. Then equation (3.37), when scaled using U, L and (L/U) becomes

$$\left(\frac{U^2}{L}\right)\frac{\partial \tilde{\mathbf{v}}}{\partial \tilde{t}} + \left(\frac{U^2}{L}\right)\tilde{\mathbf{v}} \cdot \nabla \tilde{\mathbf{v}} - (fU)\,\mathbf{k} \times \tilde{\mathbf{v}} = -\left(\frac{g\Delta h}{L}\right)\nabla \tilde{h}, \tag{3.38}$$

where the terms in the brackets indicate the order of magnitude of each terms, and tilde indicate the dimensionless variables. If the last equation is multiplied by (L/U^2) we get

$$\frac{\partial \tilde{\mathbf{v}}}{\partial \tilde{t}} + \tilde{\mathbf{v}} \cdot \nabla \tilde{\mathbf{v}} - \left(\frac{1}{Ro}\right)\,\mathbf{k} \times \tilde{\mathbf{v}} = -\left(\frac{\Delta h}{F^2 h_r}\right)\nabla \tilde{h} \tag{3.39}$$

where $F = U/\sqrt{gh_r}$ is the Froude number, h_r is the height of fluid at rest, and $Ro = U/fL$ is the Rossby number.

Since the local acceleration term and the nonlinear advective term are of the same order of magnitude in (3.39), it is evident in (3.39) that Ro determines the significance of the nonlinear advective term to the Coriolis term. In the limit of small Ro, i.e., $Ro \ll 1$, the nonlinear terms are not important, and the pressure gradient force is balanced by the Coriolis force and the resulting balance is known as the *geostrophic balance*. When $Ro \sim 1$, both the nonlinear advective terms and the Coriolis force are equally important, and in the case of circular flow in the absence of a mean wind the resulting balance is known as the *gradient wind balance*. For $Ro \gg 1$, the Coriolis force is negligible, and the nonlinear terms are

balanced by the pressure gradient force, and again for circular flow in the absence of a mean zonal wind the resulting balance is known as *cyclostrophic balance.* Therefore, Ro can also be used as a *nonlinearity parameter.*

It is also evident from (3.39) that the Froude number F determines the amplitude of the height fluctuations Δh. For example, in the case of high Rossby number flows, i.e., $Ro \gg 1$, the Coriolis term is negligible in (3.39), and we get

$$\Delta h \sim F^2 h_r \qquad (3.40)$$

Since small Froude number F corresponds to small Δh, it implies that vertical motion is strongly inhibited, which further implies that horizontal fluid motions are strongly non-divergent. Therefore, the fluid behaves more like a non-divergent fluid when Froude number is small. Defined in this sense, the Froude number behaves analogous to the Mach number for compressible flows.

In the case of small Rossby number flows, $Ro \ll 1$, e.g., for flows in geostrophic balance, equating the order of magnitude of the pressure gradient term and Coriolis force in (3.39), we get

$$\Delta h \sim \frac{F^2}{Ro} h_r \qquad (3.41)$$

This expression opens up the possibility for three flow regimes depending on the values of Ro and F: Flows for which 1) $F \gg Ro$; 2) $F \sim Ro$; and 3) $F \ll Ro$. When F exceeds Ro, rotation effects seem to dominate. When Ro exceeds F, stratification effects tend to dominate. And when $Ro \sim F$, both the effects becomes equally important.

Additional insight is obtained when the two dimensionless parameters can be combined to form an additional parameter, which can be expressed in terms of

ratio of length scales. For example, the ratio

$$\frac{F}{Ro} = \frac{U}{\sqrt{gh_r}}\frac{fL}{U} = \frac{L}{\sqrt{gh_r}/f} = \frac{L}{R_d}, \tag{3.42}$$

which is a another dimensionless number that is a ratio of the length scale L and the Rossby radius of deformation R_d. Although this new dimensionless number provides no new information than that provided by Ro and F, its use is sometimes preferred. For example, in (3.42), when $L < R_d$, we get $F < Ro$, which implies that flows with length scale smaller than R_d will be dominated by stratification effects. On the other hand, when $L > R_d$, we get $Ro < F$. For such flows the rotation effects will be stronger than stratification effects. Finally, when length scale $L \sim R_d$, we get $Ro \sim F$, which indicates that the flow will be dominated by both stratification and rotation effects. Therefore, specification of any two out of the three dimensionless parameters Ro, F, and L/R_d serves to determine the characteristics of the flow.

In the next subsection, we discuss details of the basic state.

3.3.2 Description of the Basic state

The basic state used in our simulations is determined by its potential vorticity (PV)-distribution. Our approach closely follows the one used by Ford (1994a), but it is not identical. Since our aim is to study waves generated as a consequence of flow instability, the basic state is rendered unstable by specification of a PV-anomaly over the region of interest. Since basic flows for which the PV-gradient changes sign within the flow satisfies the necessary condition for barotropic instability (Ripa 1983), the basic state is comprised of a thin strip of PV-anomaly, say $\eta_{anomaly}$, embedded over an extensive region of undisturbed fluid. We will refer to

PV of the undisturbed fluid as the background PV, and its amplitude

$$\eta_b = \frac{f}{h_r}, \tag{3.43}$$

where h_r is the height of undisturbed fluid and f is the Coriolis parameter (assumed to be a constant).

Then the PV of the basic state, η_0, can be written as

$$
\begin{aligned}
\eta_0 &= \eta_b + \eta_{anomaly} & (3.44) \\
&= \eta_b \left(1 + \frac{\eta_{anomaly}}{\eta_b} \right) & (3.45)
\end{aligned}
$$

The shape of the PV-anomaly is similar to that used by Ford (1994a). It comprises of a thin region of uniform PV-anomaly. Fig. (3.2) illustrates the typical distribution of the PV-anomaly used in the simulations. The expression used to determine the PV-anomaly is

$$\frac{\eta_{anomaly}}{\eta_b} = \begin{cases} \dfrac{A}{2} \left(1 - \tanh\left[\dfrac{y - y_0}{\Delta} \right] \right) & \text{for } y > 0 \\[2ex] \dfrac{A}{2} \left(1 + \tanh\left[\dfrac{y + y_0}{\Delta} \right] \right) & \text{for } y < 0 \end{cases} \tag{3.46}$$

where the dimensionless constant A determines the maximum amplitude of the anomaly, $2y_0$ is approximately equal to width of the region with constant PV-anomaly, and Δ provides a measure of the distance over which the PV-anomaly is adjusted to the background value. In contrast to Ford (1994a), who used a linear function to adjust the PV-anomaly to the background value over 5 grid intervals (see pg. 93, Ford 1994a), we use a hyperbolic tangent function to adjust the PV-anomaly to the background value η_b.

The basic state was determined by the PV-distribution, which, based on
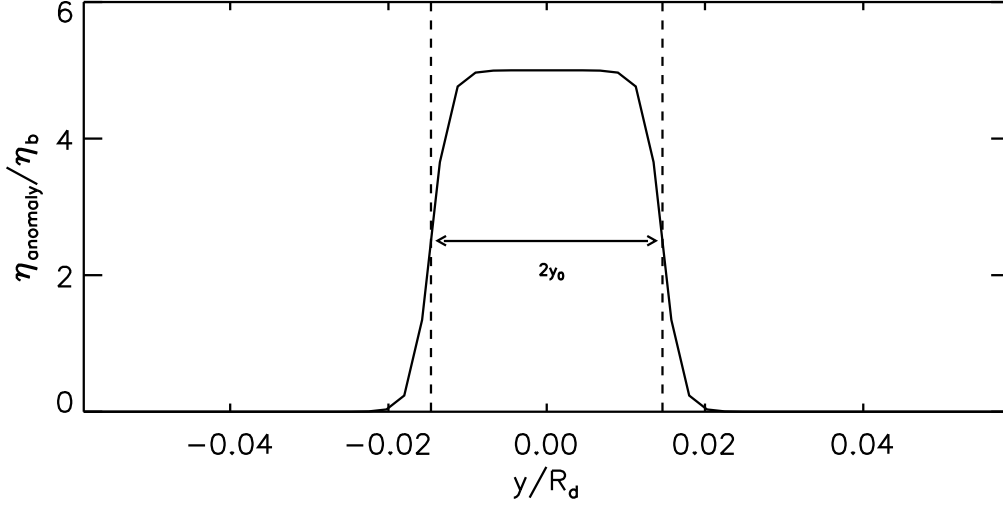
Figure 3.2: Figure shows the distribution of the PV-anomaly $\eta_{anomaly}$ obtained using expression (3.46). $A = 5$ and $y_0 = 0.014625R_d$, and $\Delta = .00225R_d$. R_d $(=\sqrt{gh_r}/f)$ is the Rossby radius of deformation.

(3.46), is dependent on two parameters: the amplitude of the anomaly A and the half-width y_0. It is, however, not obvious how these parameter values are related to the more familiar basic state flow parameters, such as the Rossby number and the Froude number. Therefore, in the following paragraph, we discuss how the parameters Ro and F can be determined for a given A and y_0. First, the basic state wind and height field is determined based on the PV-distribution, and then we use the obtained wind and the height profiles to estimate the corresponding Rossby and Froude numbers.

The basic state height h_0 can be obtained by combining the expression for shallow-water PV, i.e.,

$$\eta_0 = \frac{(\zeta_0 + f)}{h_0}, \tag{3.47}$$

60
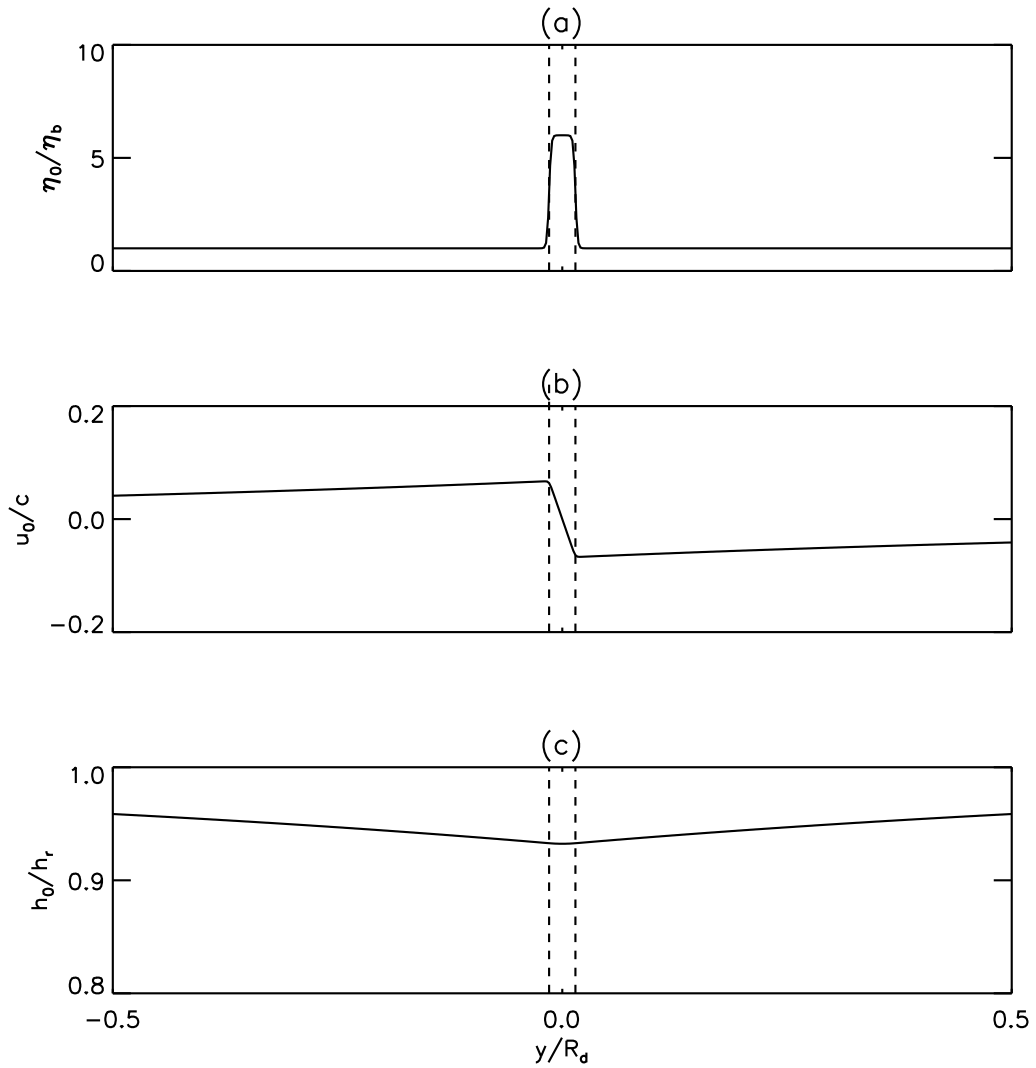
Figure 3.3: Figure shows that basic state profiles: $A = 5$, $y_0 = 0.014625 R_d$, and $\Delta = .00225 R_d$ ($Ro = 4.5$ and $F = .066$); **(a)** Normalized PV of the basic state η_0/η_b. **(b)** Normalized basic state velocity u_0/c, where $c = \sqrt{gh_r}$; **(c)** Normalized basic state height h_0/h_r. Dashed lines indicate the width $2y_0$ of the PV-anomaly.

with the geostrophic balance relation,

$$fu_0 = -g\partial_y h_0. \tag{3.48}$$

Combining the last two equations we get

$$\partial_{yy}^2 h_0 - (f\eta_0/g)h_0 + f^2/g = 0, \tag{3.49}$$

where we have substituted $\zeta_0 = -\partial_y u_0$. Then (3.49) is solved numerically subject to the following boundary condition,

$$h_0 \to h_r \qquad \text{as} \qquad y \to \pm\infty. \tag{3.50}$$

Then, the basic state velocity u_0 is determined using (3.48).

Once the height and the velocity profiles are determined, the Rossby number Ro and the Froude number F can be readily evaluated using the expressions

$$Ro = \frac{U}{fL}, \tag{3.51}$$

and

$$F = \frac{U}{c}, \tag{3.52}$$

where U is the velocity scale, L is the length scale, and $c = \sqrt{gh_r}$ is the non-rotating shallow-water gravity wave phase speed at rest. We choose U equal to the maximum wind speed in ms^{-1} and L equal to half-width of PV-anomaly y_0 in meters.

Fig. (3.3) (b) shows the typical shape of the basic height h_0 obtained using

(3.49). The height field takes a minimum value along the y-axis, and gradually increases and approaches the height of fluid at rest h_r as we move away from the low pressure center. The basic state wind u_0, obtained from (3.48), comprises a thin region of strong shear associated with the PV-anomaly (see fig. 3.3 (c)). In the region outside the PV-anomaly, the wind shear is weak and the wind speed gradually relaxes as the distance from the y-axis increases. The e-folding distance outside the anomaly is the Rossby radius of deformation R_d (see section (1.3.7) for discussion on the concept of R_d).

In case of the basic state profile shown in the fig. (3.3), which corresponds to $A = 5$ and $y_0 = .014625R_d$, we get $F = 0.06681$, and $Ro = 4.568$. Furthermore, we also observe that varying the amplitude of the PV-anomaly A, while the width y_0 is held constant, produces almost linear variation in both Rossby number Ro and Froude number F (as can be seen in fig. 3.4). On the other hand, if the amplitude of the PV-anomaly A is kept constant and the width y_0 is varied, F changes almost linearly with y_0, but Ro varies very slowly (see fig. 3.5).

3.3.3 Model Initialization

As our first case, we consider the simulation of a basic state for which the effect of background rotation and the effect of divergence can be expected to be small. The basic state shown in fig. (3.3) has $Ro = 4.568$ and $F = .0668$. The evolution of this profile will be used to study the mechanism of gravity wave emission associated with the instability of barotropic parallel flows. The Rossby number value of order one magnitude implies that the effect of rotation on the PV-anomaly can be expected to be small, at least, during the initial stages of the simulation, and the small Froude number indicates that the effect of divergence will remain small. Hereafter this simulation will be referred to as $S1$.
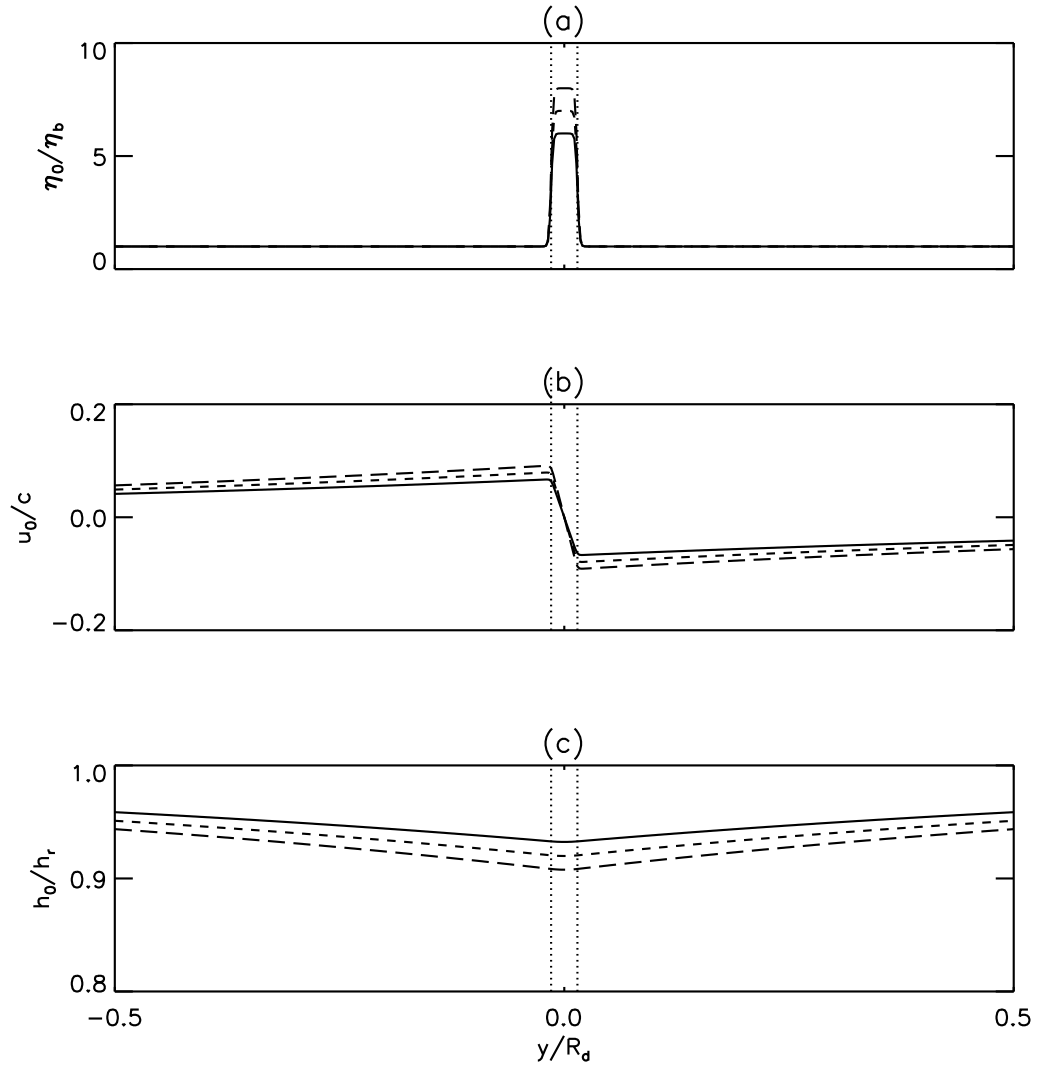
Figure 3.4: Same as fig.(3.3), but showing the effect of varying A when $y_0 = .014625 R_d$. Solid line is for $A = 5$ ($F = .067$ and $Ro = 4.56$). Dashed line is for $A = 6$, ($F = .079$ and $Ro = 5.4$). Long-dashed line for $A = 7$ ($F = .091$ and $Ro = 6.23$).
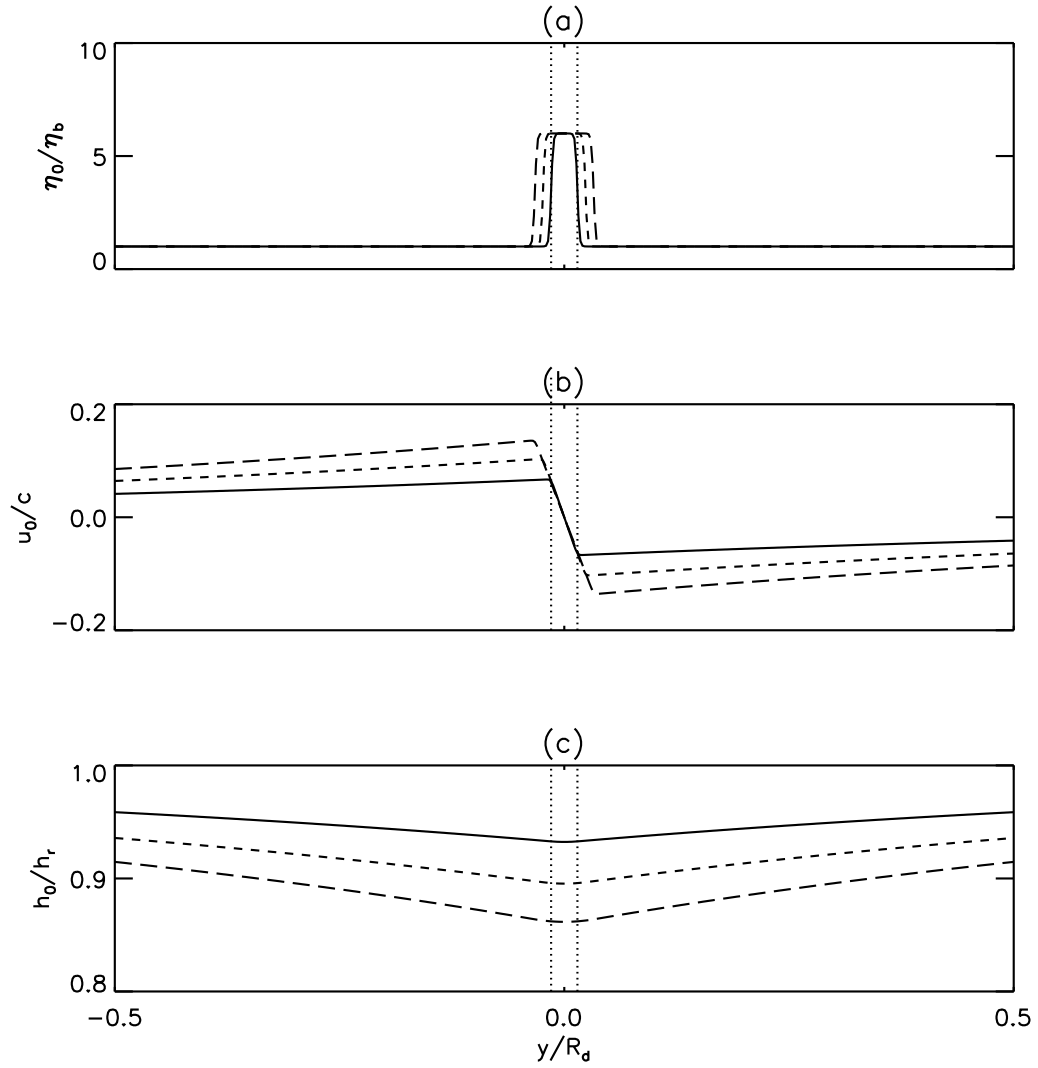
Figure 3.5: Same as fig. (3.3), but showing the effect of varying y_0 when $A = 5$. Solid line $y_0 = .014625R_d$ ($F = .067$ and $Ro = 4.56$). Dashed line is for $y_0 = .023625R_d$ ($F = 0.1$ and $Ro = 4.35$). Long-dashed line for $y_0 = 0.032625$ ($F = .135$ and $Ro = 4.15$).

Furthermore, since the properties of this particular basic state profile are very similar to Ford's (1994a) simulations Ai and Aii, the simulation results will also be compared with Ford's (1994a). Ford's (1994a) simulations Ai and Aii correspond to $A = 5$, and $2y_0 = .018R_d$ and $.035R_d$, respectively. Firstly, this should serve to verify that our simulation results are consistent with Ford's findings and that our model is behaving properly. Secondly, since we intend to perform a more detailed analysis of the process of wave emission, this will help to highlight the new insights revealed by our analysis.

The main difference between the model used by Ford (1994a) and ours is that he used a pseudo-spectral scheme to evaluate the derivatives in the streamwise (x) direction. He used a second-order centered-difference scheme to evaluate the cross-stream derivatives. Ford also used variable cross-stream resolution to resolve the long gravity waves propagating away from the vortical region, which was resolved using a uniform grid spacing.

Furthermore, he used dissipation only along the x-direction. Ford argued that since the flow field evolves into a rotating flow, the application of dissipation along one direction should be sufficient for purposes of maintaining numerical stability. Ford's choice is certainly arguable since, as is shown later, the flow evolves structures that are thin in the cross-stream (y) direction. However, as a part of our study, we will consider the effects of using both isotropic and anisotropic dissipation on the simulation results.

In all the simulations considered, the positive x-direction is taken as the *east-west* or *zonal* (streamwise) direction and the positive y-axis the *south-north* or *meridional* (cross-stream) direction. The wind direction is from east to west in positive y-region, decreases to zero at $y = 0$, and blows from west to east in the negative y-region (see fig. (3.3) (b)). The basic state flow is uniform in the zonal

66

direction.

Such wind flow patterns are often found near 10°-15° North and South of the equator, usually associated with the Intertropical Convergence zone (ITCZ). In the Northern hemisphere these strong shear layers usually have wind differences in the range 5 - 15 ms^{-1} over a few degrees of latitude between the easterlies to the north and westerlies to its south (see e.g., Lipps (1970), Nieto Ferreira and Schubert (1997), Mishra et al. (2007), Yokota et al. (2015)).

Finally, the simulations were initialized by addition of small-amplitude sinusoidal perturbations to the basic state. The wavelength of the disturbance is set equal to the wavelength of the fastest growing mode. The fastest growing mode was determined using matrix method similar to that used by Ford (1994a). The details of the stability analysis are provided in the Appendix. The form of disturbance height field $h'[x, y]$ added to perturb the basic state height is

$$h'[x, y] = \exp \left[-\frac{|y|}{l_y} \right] \sin \left[k_x x + \beta \right], \qquad (3.53)$$

where k_x is the wave number of the fastest growing mode, β indicates the phase, and l_y is the meridional e-folding length of the height perturbations. Thus the total height of the fluid

$$h[x, y, t = 0] = h_0[y] + h'[x, y] \qquad (3.54)$$

The use of shallow-water equations to study atmospheric processes is limited by the fact that for most part our atmosphere is continuously stratified. Continuous stratification implies that disturbances tends to propagate more efficiently as internal gravity waves as opposed to external or shallow-water gravity waves. Internal gravity waves can propagate in the vertical direction and have

small horizontal phase speeds compared to shallow-water gravity waves. Shallow-water theory can be adopted to explain the nonlinear effects associated with the flow over topography, such as the downslope wind storms. The shallow-water approximation is usually applied to a shallow layer of atmosphere in the troposphere which is capped by an inversion, and the acceleration due to gravity g is replaced by reduced acceleration due to gravity g' (see e.g., Jiang 2014, and references therein), and in tropical region due to barotropic nature.

Lastly, since our aim is to investigate the nature of the wave forcing mechanism, and not to accurately predict the characteristics of the observed gravity waves in the atmosphere, we choose the depth of the fluid at rest h_r equal to 3 km and use reduced acceleration due to gravity g' equal to 0.3 m s^{-2}. These choices result in non-rotating gravity wave phase speed c equal to 30 ms^{-1}. Disturbances with phase speeds in this range are generally considered significant as far as meteorological motions are concerned. We also choose the Coriolis parameter $f = 10^{-4}$ s^{-1}, which corresponds to the typical value for mid-latitudes, as barotropic vortices have also been observed in the mid-latitudes (see e.g., Weinand 2000; Maejima et al. 2006) (Note that the value of f at the previously mentioned latitude 15° is 3.8×10^{-5}, which is sufficiently close to the adopted value of 10^{-4}). Table (3.1) lists the initialization parameter values used in simulation $S1$. The details of the numerical discretization, dissipation and damping parameters used in this simulation are provided in table (3.2). In the next section, results from simulation $S1$ will be discussed.

Initialization parameters		Values
		Simulation S1
Height of fluid at rest	h_r	3 km
Reduced gravity	g'	0.3 m s^{-2}
Coriolis parameter	f	10^{-4} s^{-1}
Gravity wave phase speed	$c\ (=\sqrt{gh_r})$	30 m s^{-1}
Rossby radius	$R_d\ (=c/f)$	300 km
Half-width of PV-anomaly	y_0	$.014625 R_d$
Amplitude of PV-anomaly	A	5
Rossby number	Ro	4.568
Froude number	F	.06681
Wave number of fastest growing mode	k_x	$27.94/R_d$
Perturbation e-folding distance	l_y	$0.9 R_d$

Table 3.1: Table lists the initialization parameter values used in simulations. The expression used to calculate the Rossby number $Ro = U/fL$ and the Froude number $F = U/c$, where U is the maximum wind speed, and L is equal to y_0.

3.4 Results and discussion

3.4.1 Near-field fluctuations

Fig. (3.6) shows the evolution of the potential vorticity field η after time $t = 11$ from the start of the simulation, where time is in units of $(1/f)$. Small amplitude sinusoidal perturbations $(\hat{h}/h_r = 10^{-4})$ were used to disturb the basic state; consequently, it takes some time for perturbations to become large enough to disturb the initially parallel PV-field. Wave-like disturbances on the PV-field are clearly visible in frame (a) of fig. (3.6). Subsequent frames show that the initially parallel strip begins to roll-up. This further results in stretching, and formation of thin regions of steep PV-gradient known as "braids". Fig. (3.6) also shows the evolution of the wind field vector, which shows that the roll-up of the strip is associated

Numerical discretization parameters		Simulation
		S1
Meridional grid spacing	Δy	$0.00225 R_d$
Zonal grid spacing	Δx	$2\Delta y$
Total grid points in x-direction	M	51
Total grid points in y-direction	N	10001
Zonal domain length	L_x	$0.225 R_d$
Meridional domain length	$2L_y$	$22.5 R_d$
Time step	Δt	5.625 s
Robert-Asselin filter	α	.02
Width of damping layer	D	$2.25 R_d$
Courant number	C_n	0.25
Zonal dissipation parameter	γ_x	0.25×10^{-4}
Meridional dissipation parameter	γ_y	0

Table 3.2: Table lists the spatial and temporal discretization, and dissipation parameters values used in simulation. Courant number $C_n = c(\Delta t/\Delta y)$ and $c = \sqrt{gh_r}$ is the non-rotating gravity wave phase speed at rest. $\gamma_x = \nu_x/\Delta x^6$, and $\gamma_y = \nu_y/\Delta y^6$, where ν_x and ν_y are the diffusivity along x and y-directions, respectively. The value of Rayleigh damping coefficient τ_R increases gradually from 0 to 1 at the boundary.

with the development of cyclonic wind circulation. As the disturbance continues to grow, the vortex appears to rotate and the braids on either side of the cyclonic vortex are stretched further (see frames (c) and (d) of fig. (3.6)).

Figs. (3.7) shows the evolution of the meridional cross-section of PV along lines $x = .08$, 0.1, 0.13 and 0.15, respectively, corresponding to the vertical lines in fig. (3.6)(a) and (b). Plots are shown for times $t = 10.125, 11.25, 12.375$. Unit of time is $1/f$. Clearly the initial roll-up of the PV-strip is accompanied by advection of the PV-front, and a subsequent increase in the width of the PV-anomaly. We also observe that as the PV-front is meridionally advected, the gradients in the deformation zone steepen with time due to differential advection across the
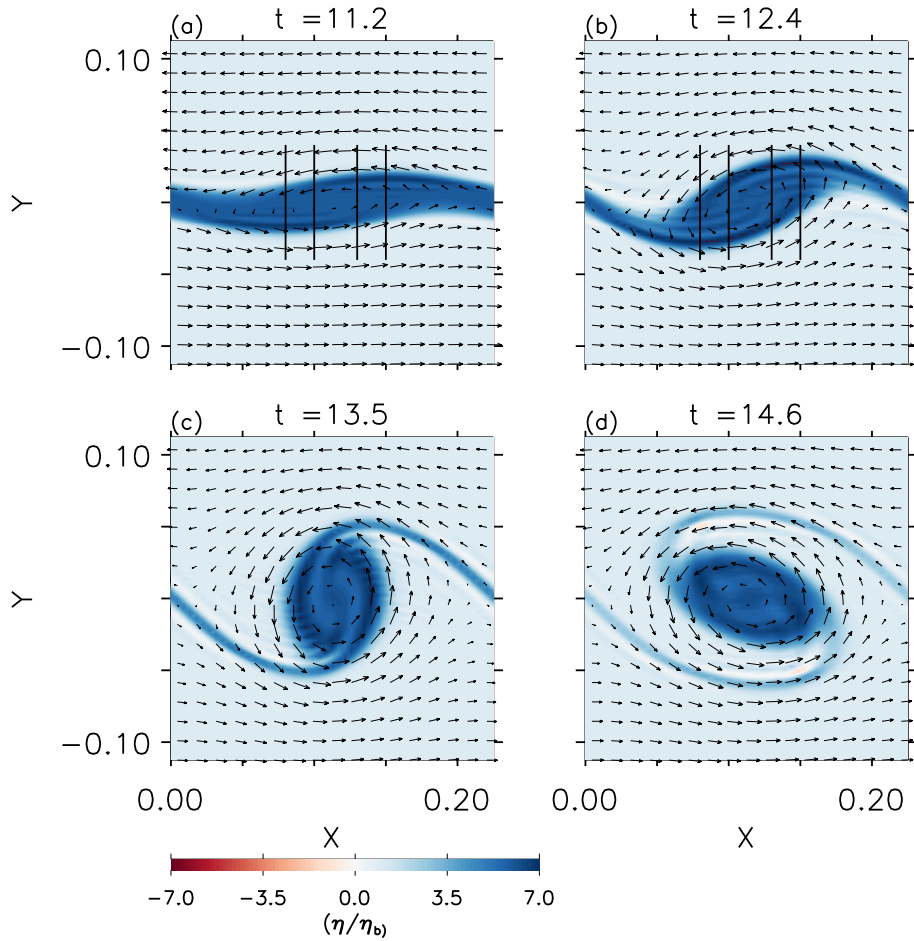
Figure 3.6: Figure showing the evolution of the potential vorticity field η/η_b, where η_b $= h_r/f$. Wind field vector **v** has been overlaid on it. The magnitude of longest wind vector is $\approx 3.0\ \mathrm{ms}^{-1}$. X and Y indicate the downstream and cross-stream distances in units of R_d. Time is in units of $1/f$. The vertical lines for $t = 11.2$ and 12.4 corresponds to the x/R_d locations plotted in fig. (3.7).

71
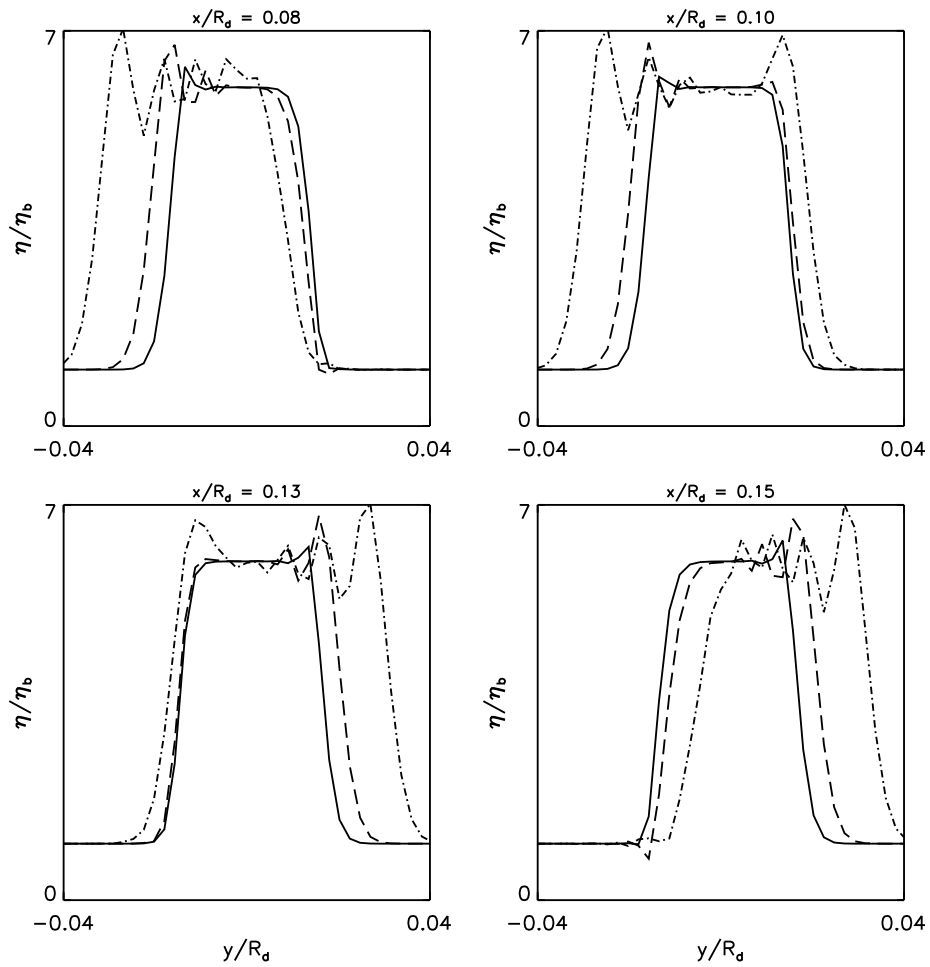
Figure 3.7: Cross-section along the lines shown in fig. 3.6 (a) and (b) showing evolution of the (η/η_b) (See fig. (3.6) for the corresponding x/R_d). The lines are located along $x/R_d = .08$, 0.1, .13, and 0.15, respectively. Plots times are $t = 10.125$ (Solid-line), 11.25 (Long dash line), and 12.375 (Dot-dashed line).
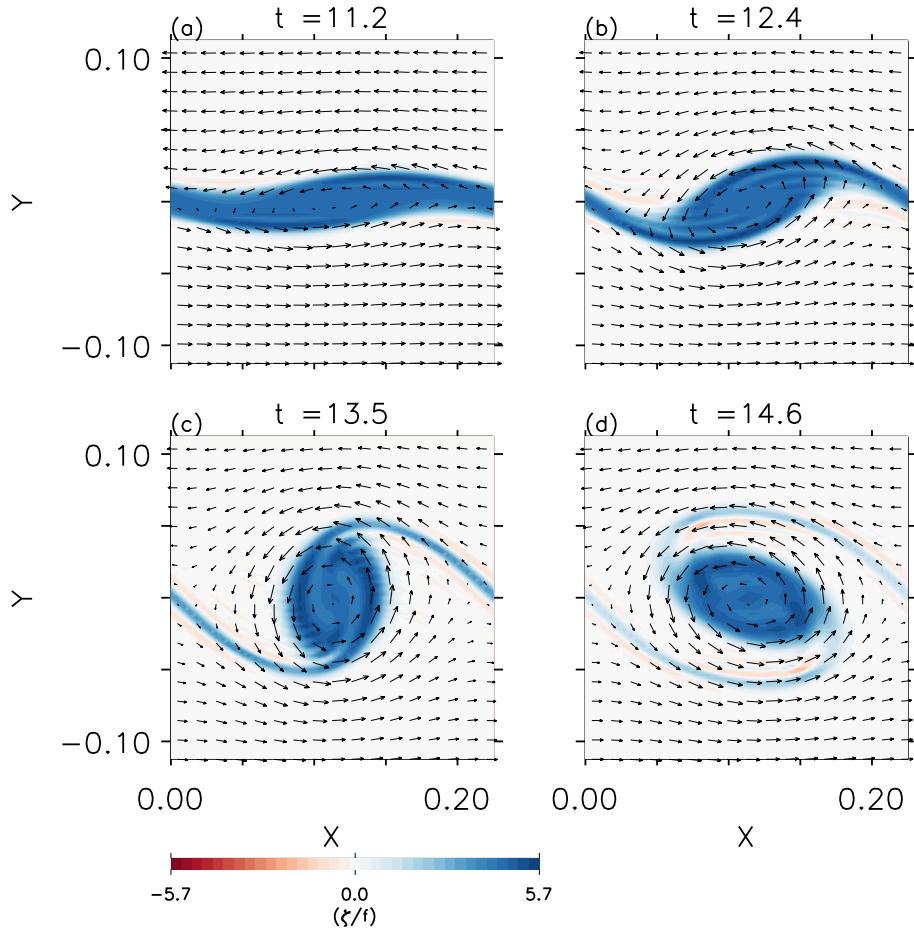
Figure 3.8: Same as fig. 3.6, but showing relative vorticity ζ/f.

gradient. After some time, model has trouble resolving this steep gradient and gives rise to numerical errors. Consequently, as it is compressed, the leading edge of the front develops an over-shoot and produces Gibbs-like oscillations, which extend to the trailing edge in some instances (see e.g., Mendez-Nunez and Carrol (1993) for discussion of development of such oscillations).

The resolution used in the meridional direction in simulation $S1$ is the same as that used by Ford (1994a) for his simulations Ai and double compared to his simulation Aii. Since the PV-anomaly in simulation $S1$ has the same form and amplitude as Ford's simulations Ai and Aii, it is quite likely that these
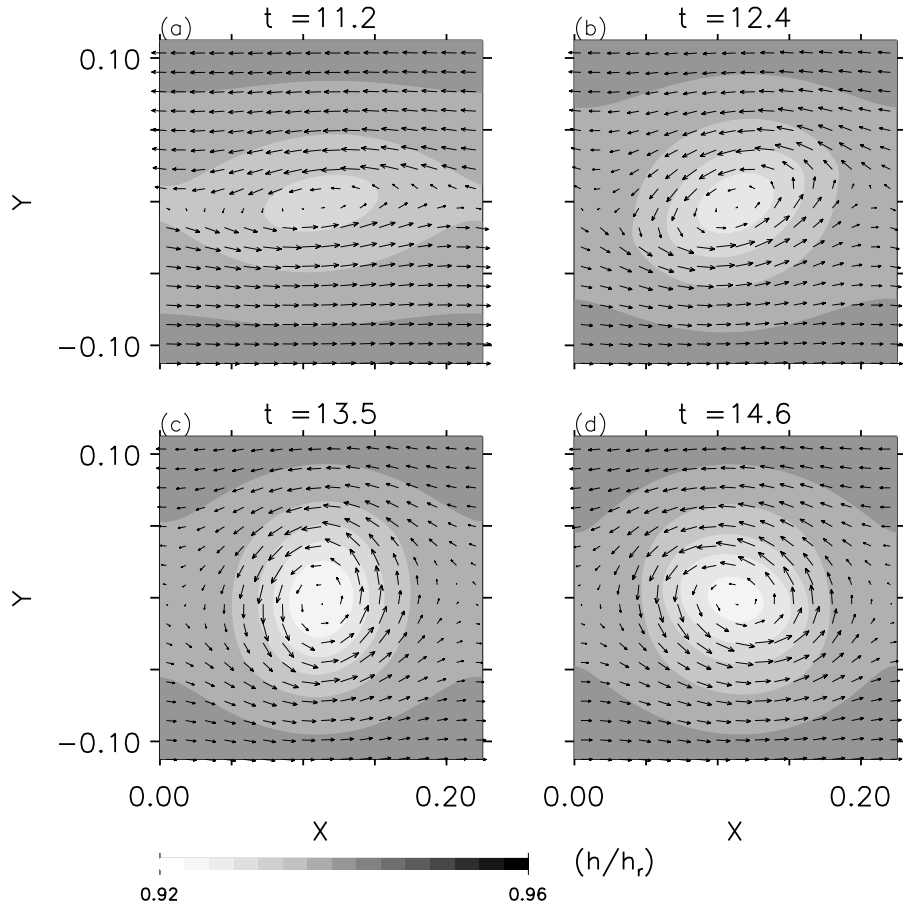
Figure 3.9: Figure shows the evolution of the normalized height field h/h_r, where h_r is the fluid rest height, associated with the growth of the perturbations. The wind field vector **v** has been overlaid on it.

overshoots and oscillations also developed in the simulations conducted by Ford (1994a). Details of whether such oscillations arose have not been discussed by Ford, though his published figures are detailed enough to reveal them (e.g., see his fig. 3(d)). The consequence of these numerical errors on the mechanism of generation the gravity waves have not been discussed in the past and, consequently, will be investigated later in Section (3.5). For now we continue with our analysis of the results from simulation $S1$.

Fig. (3.8) shows the evolution of the vorticity field ζ after time $t = 11$ from

74
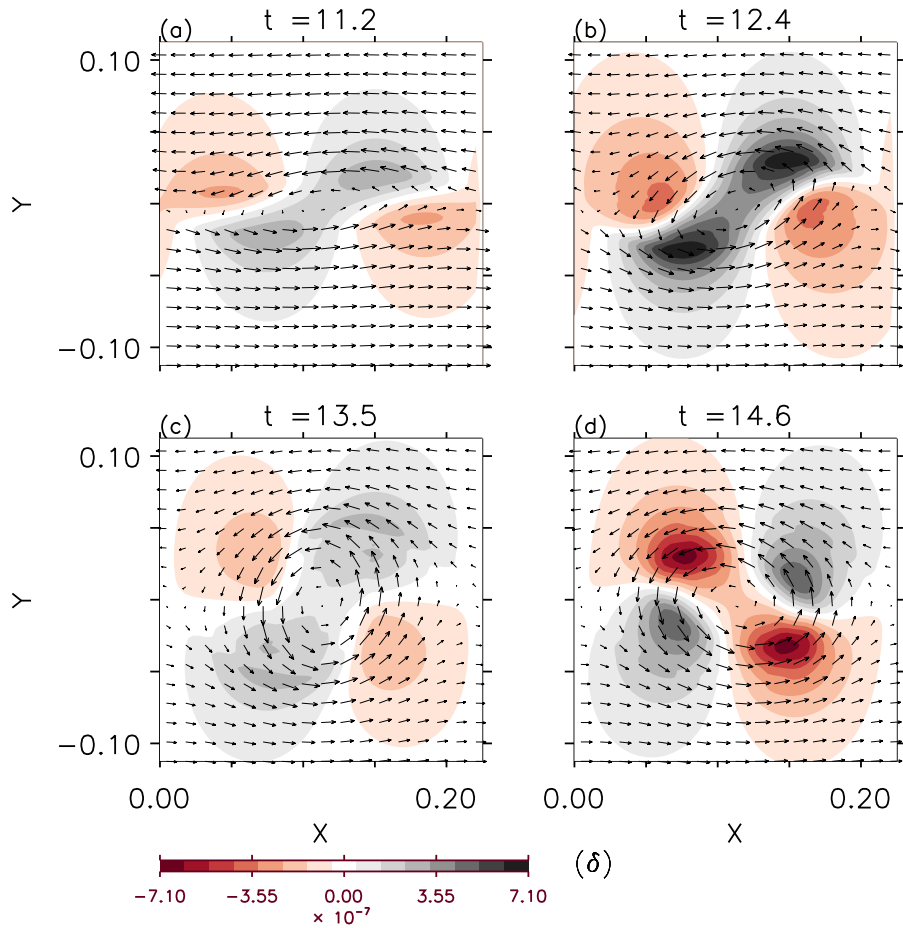
Figure 3.10: Figure showing the evolution of divergence δ-field (Unit is s^{-1}) associated with the intensification of the disturbance. Wind field $\mathbf{v}$ is overlaid on the divergence plot.

the start of the simulation. The vorticity plots are very similar to the PV-plots, and differ only in magnitude. This indicates that the evolution of PV is dominated by the evolution of the vorticity field. The figure also indicates that the roll-up of the vorticity strip, which is primarily comprised of positive vorticity, results is development of thin regions of negative vorticity, as indicated by the faint, thin red regions. Positive vorticity is associated with cyclonic wind circulation and negative vorticity with anticyclonic wind circulation. These anticyclonic circulations are too weak to be visible even in the wind vector plots. However, they become clearly
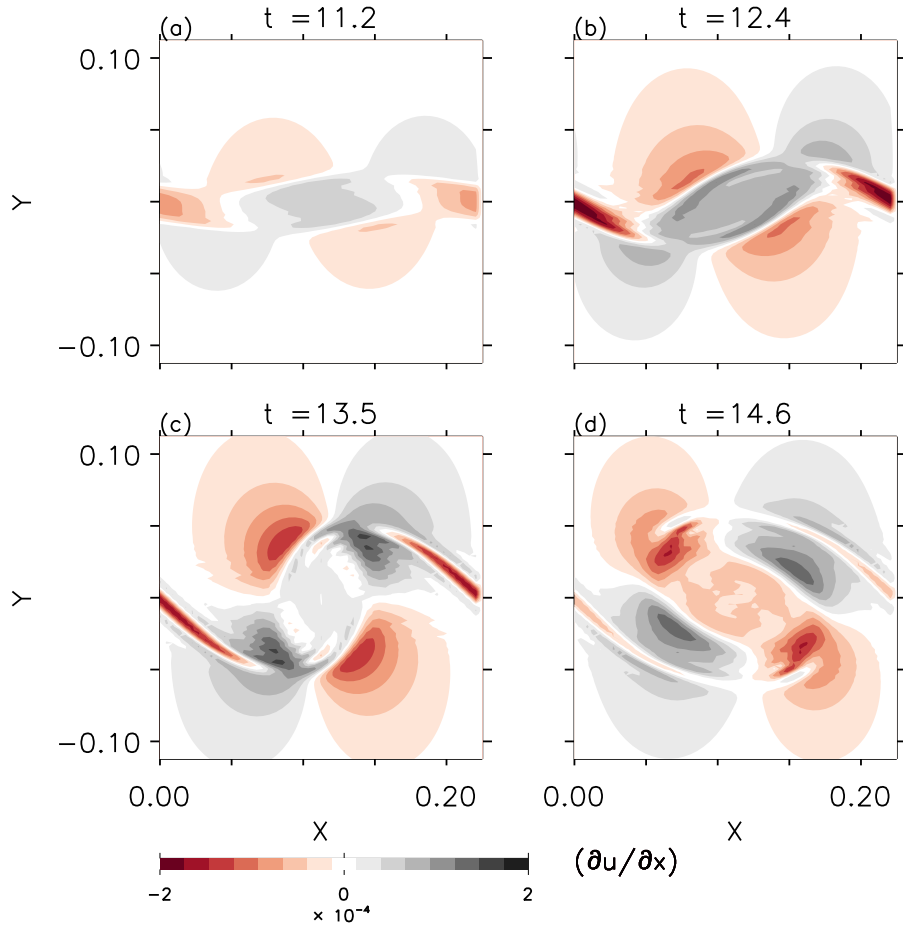
Figure 3.11: Figure showing the $(\partial u/\partial x)$-field (Unit is s^{-1}).

visible when the mean zonal flow is subtracted from the flow field. The significance and discussions on these anticyclonic circulations will be provided later when we discuss fig. (3.25).

Fig. (3.9) shows the evolution of the height field h during the roll-up of the vortex. Clearly evident is the deepening of the pressure associated with the intensification of the cyclonic circulation.

Fig. (3.10) shows the evolution of the near-field horizontal divergence δ (= $(\partial_x u + \partial_y v)$). The divergence field shows a *quadrupolar* or *four-cell* pattern which undergoes slow change in intensity along with the evolution of the vorticity field.
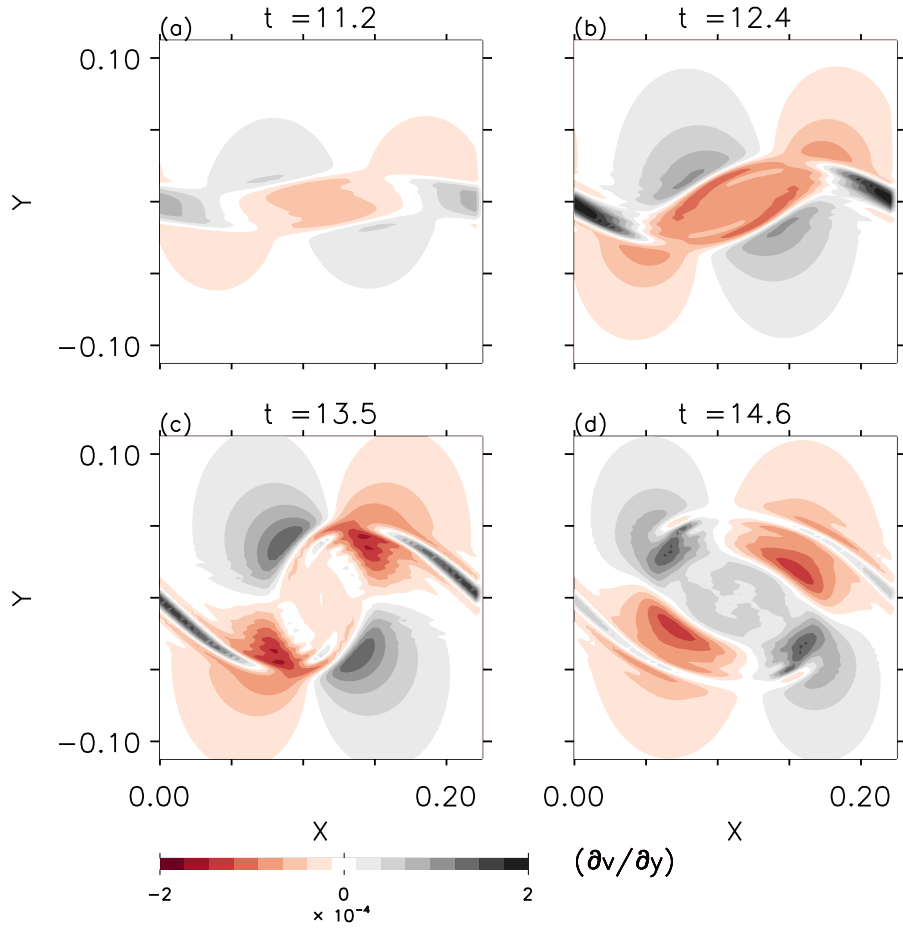
Figure 3.12: Figure showing evolution of $(\partial v/\partial y)$-field (Unit is s^{-1}).

Such four-cell pattern is typically associated with a balanced jet-streak or a dipole vortex (see e.g., Houghton et al. 1981; Vantuyl and Young 1982; Cunningham and Keyser 2000; Snyder et al. 2007). A dipole vortex is considered as an idealization of the atmospheric jet streak. It is characterized by a localized jet between two counter rotating constituent vortices (see e.g., Snyder et al. 2007, 2009). Although, the vorticity field of fig. (3.8) failed to show a localized jet between two counter rotating vortices, however, as shown later, they become visible when the zonal mean flow is subtracted from the total field. Of particular interest even to our study is the forcing associated by jet between the counter-rotating vortices.
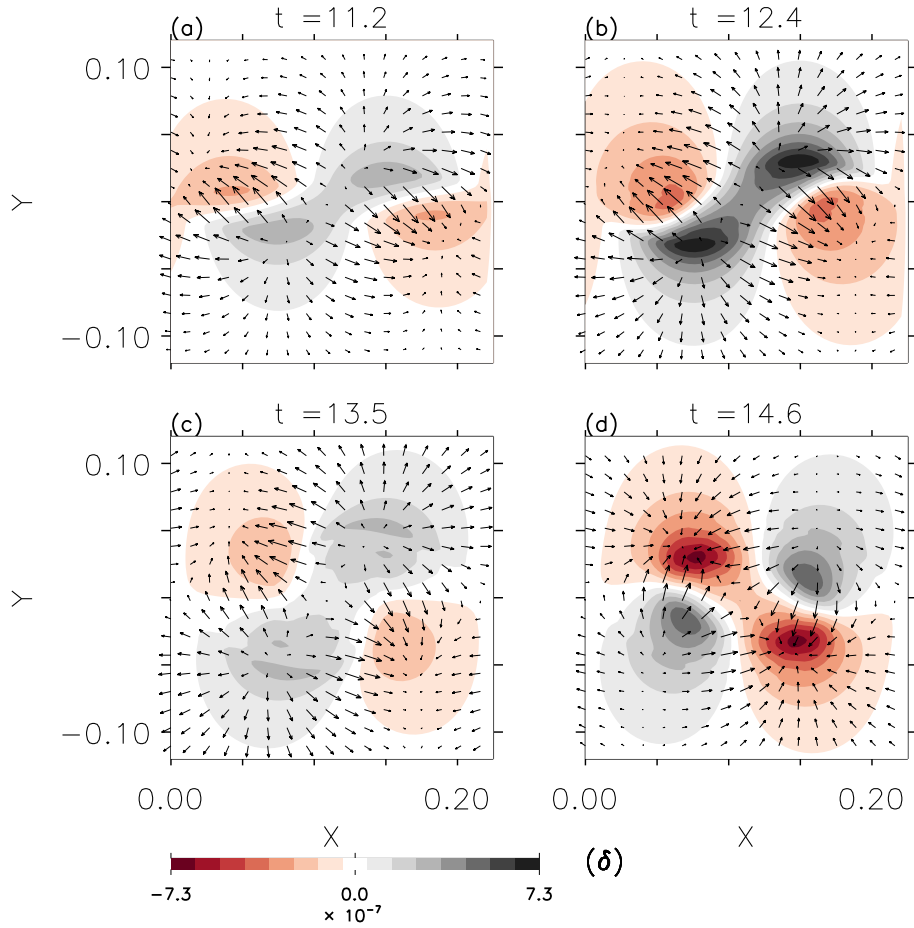
Figure 3.13: Figure showing the evolution of divergence δ-field (Unit is s^{-1}) associated with the intensification of the disturbance. Also show is the *divergent* wind field $\mathbf{v}_\chi$. Amplitude of the maximum wind is ≈ 0.002 m/s.

Frames (a) and (b) of fig. (3.10) show that the divergence field during the vortex roll-up phase is initially weak and begins to intensify as the perturbation grows (grey regions indicate positive divergence, and pinkish-red regions show negative divergence or convergence). Frame (b) shows that the major axis of the cyclonic vortex is associated with strong positive divergence. However, 2 units of time later (see frame (d)), the vortex has rotated and the major axis is now a region of strong convergence. Interestingly, throughout the flow, we observe that the divergence remains oriented along a SW to NE axis, while the convergence is
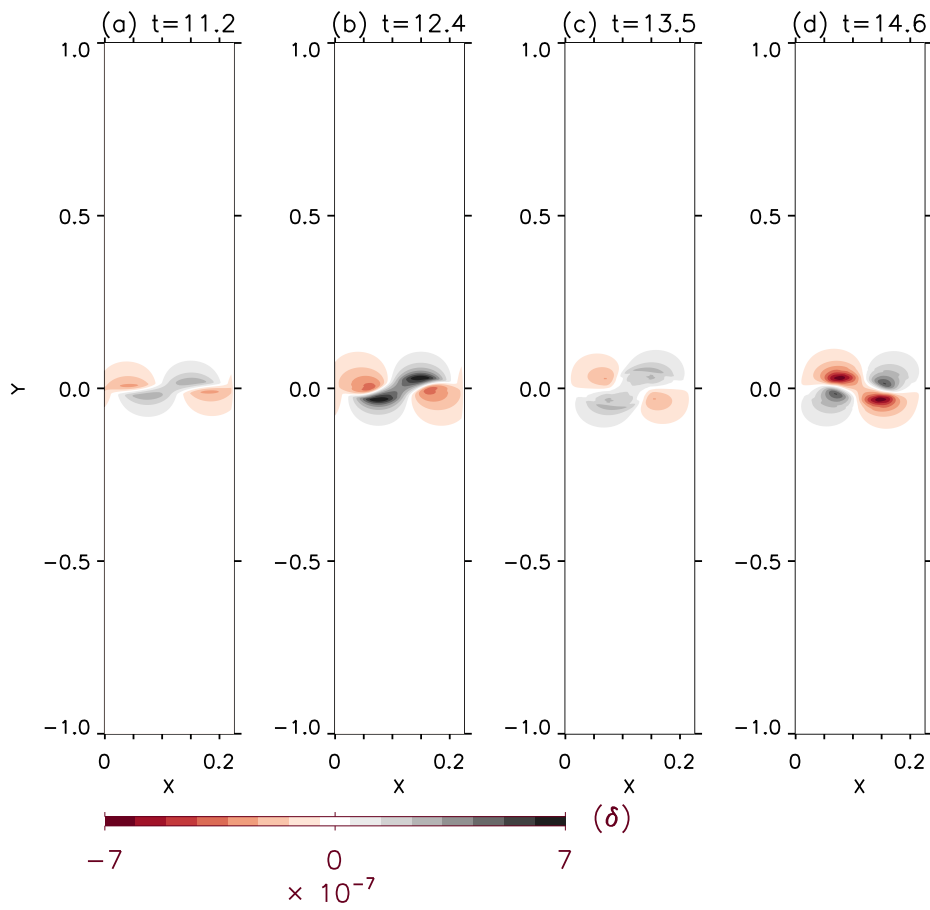
Figure 3.14: Same as figure (3.10) (i.e., showing divergence (δ) field), but in the intermediate domain.
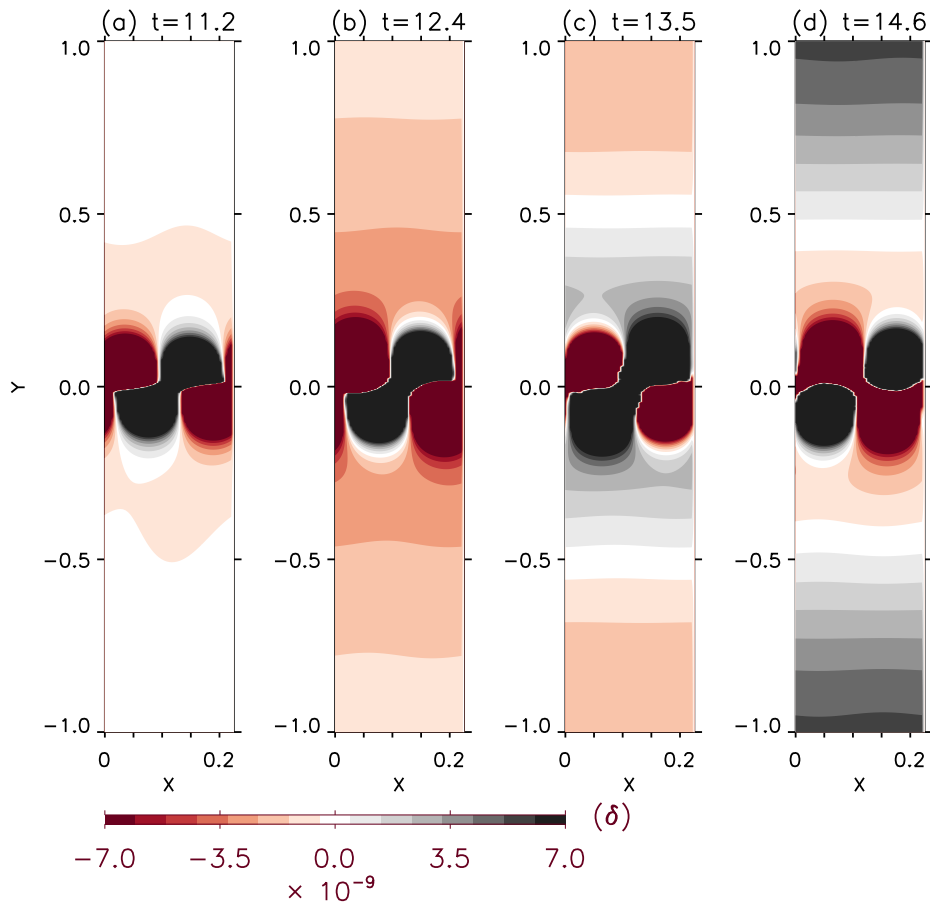
Figure 3.15: Same as figure (3.14) (i.e., showing divergence (δ) field), but only show divergence contours in the range (-7, 7)$\times 10^{-9}$ s^{-1}. Therefore, the divergence (δ) contours with values exceeding this range have been assigned the extreme values of the new contour range.
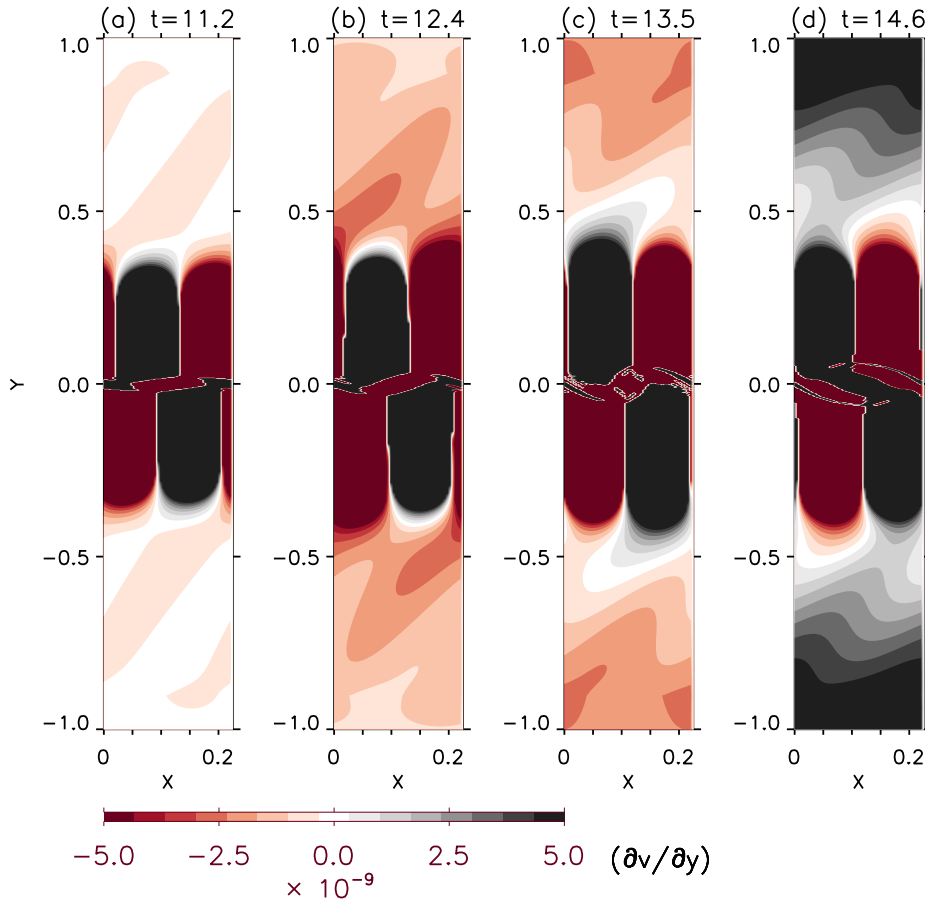
Figure 3.16: Same as fig. (3.15), but showing $(\partial v/\partial y)$ (Unit is s^{-1}).

oriented along a SE to NE axis.

Since the horizontal divergence δ $(= \partial_x u + \partial_y v)$ arises as a consequence of contribution from two terms, namely, the zonal term $\partial_x u$ and the meridional term $\partial_y v$, we look at the evolution of each fields to gain some insight. Figs. (3.11) and (3.12) show the evolution of $\partial_x u$ and $\partial_y v$, respectively. Fig. (3.12) shows that the vorticity fronts (visible in the first and the third quadrant) are regions of fluid convergence associated with the meridional motion. However, fig. (3.11) shows that these are also regions of strong positive divergence associated with zonal motion, and this divergence is stronger in magnitude compared to the
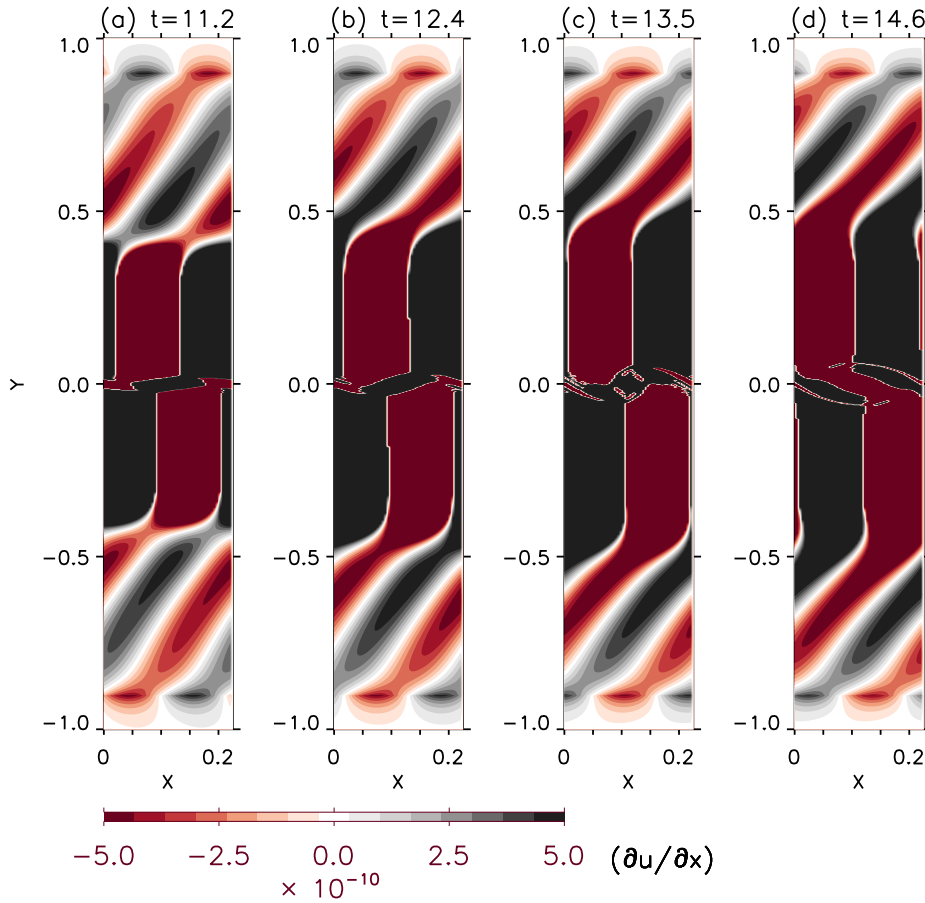
Figure 3.17: Same as fig. (3.15), but showing $(\partial u/\partial x)$ (Unit is s^{-1}).

convergence associated with meridional motion. Consequently, the resultant δ-field of fig. (3.10) shows that vorticity front as a regions of strong positive divergence (dark grey contour).

The subsequent divergence field (see fig. (3.10) (c)) shows that the δ-field has weakened. We also observe that although both $\partial_x u$ and $\partial_y v$ fields have intensified (see figs. (3.11) (c) and (3.12) (c)), this time there occurs a strong cancellation between the fields, which accounts for the decrease in the δ-field.

The next frame, i.e., fig. (3.10) (d), shows that the δ-field has intensified again. Although this time, in comparison to divergence pattern in frame (b), the
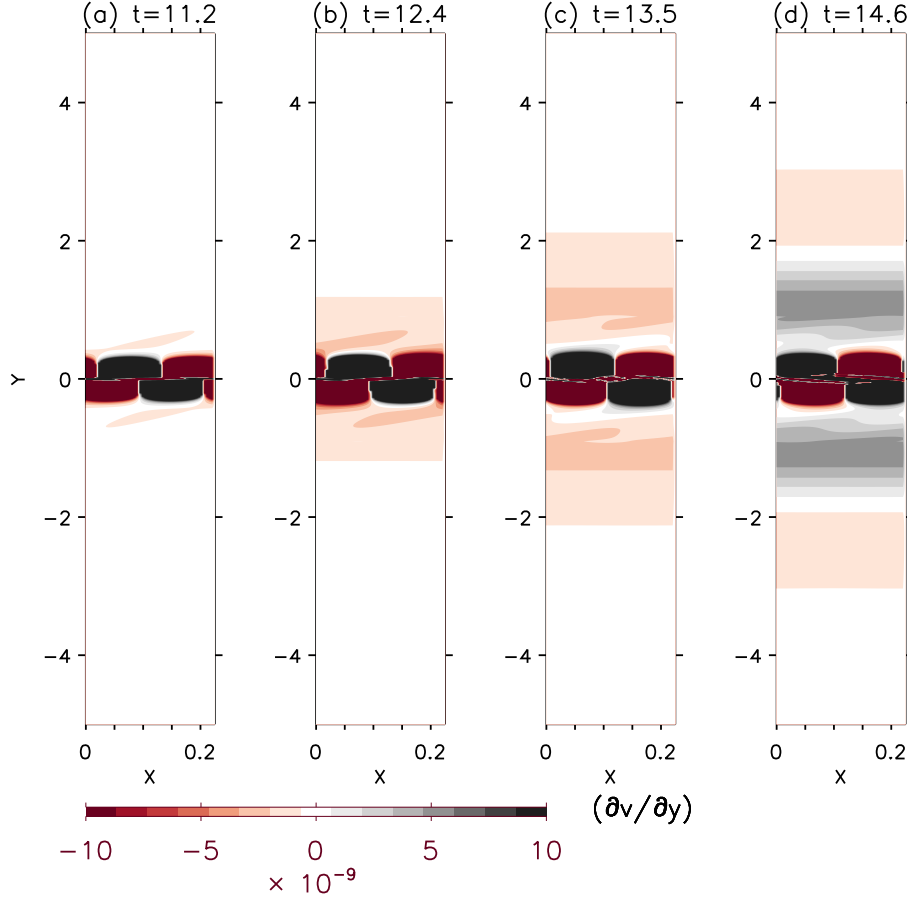
Figure 3.18: Same as fig. (3.16), but showing the far-field $\partial_y v$.

center of the cyclonic vortex is a region of fluid convergence. Again, we observe that the δ-field is dominated by the contribution from the zonal term $(\partial_x u)$ (see figs. (3.11) (d) and (3.12) (d)).

In summary, we observed that the near-field δ in simulated barotropic vortex undergoes oscillation in the intensity as the vortex continues to evolve. The near-field divergence δ field arises as a consequence of imbalance between the amplitude of meridional term $\partial_y v$ and zonal term $\partial_x u$. These terms have opposite sign, but the magnitude of $\partial_x u$ is always slightly greater than $\partial_y v$, thus resulting in the near-field δ to be non-zero. Later when we analyze the intermediate region

83
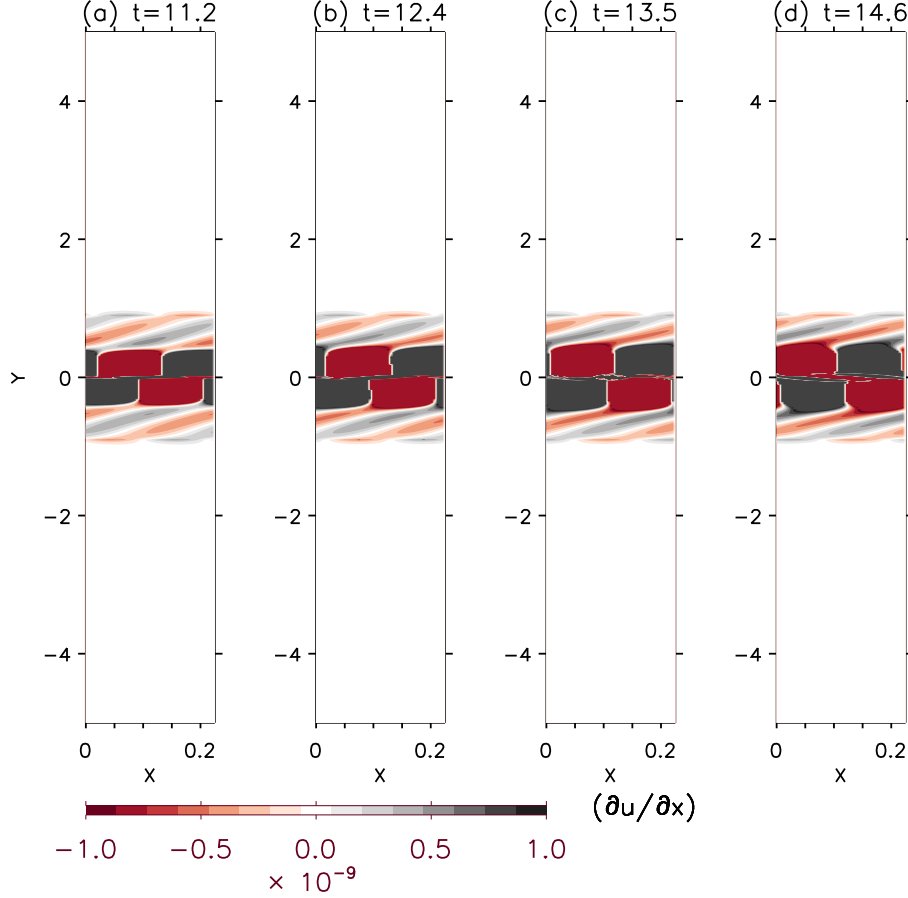
Figure 3.19: Same as fig. (3.17), but showing the far-field $\partial_x u$.

δ-field it will be shown that the roles have reversed, i.e., the amplitude of $\partial_y v$ dominates in the intermediate region, thus compensating for the excess $\partial_x u$ in the near-field. This is important because it assures the mass remains conserved. Our results also showed that more axisymmetric the flow, weaker the divergence δ field.

In order to gain some insight into the source of imbalance between $\partial_x u$ and $\partial_y v$ in the near-field, we look at the divergent wind field $\mathbf{v}_\chi$ associated with the near-field divergence δ. Fig. (3.13) shows the divergence field with the divergent wind field $\mathbf{v}_\chi$ overlaid on it, where $\mathbf{v}_\chi$ is defined as $\mathbf{v}_\chi = \nabla \chi$, such that $\nabla^2 \chi = \delta$, and χ is the velocity potential . Evident is the direction of wind vectors starting

84
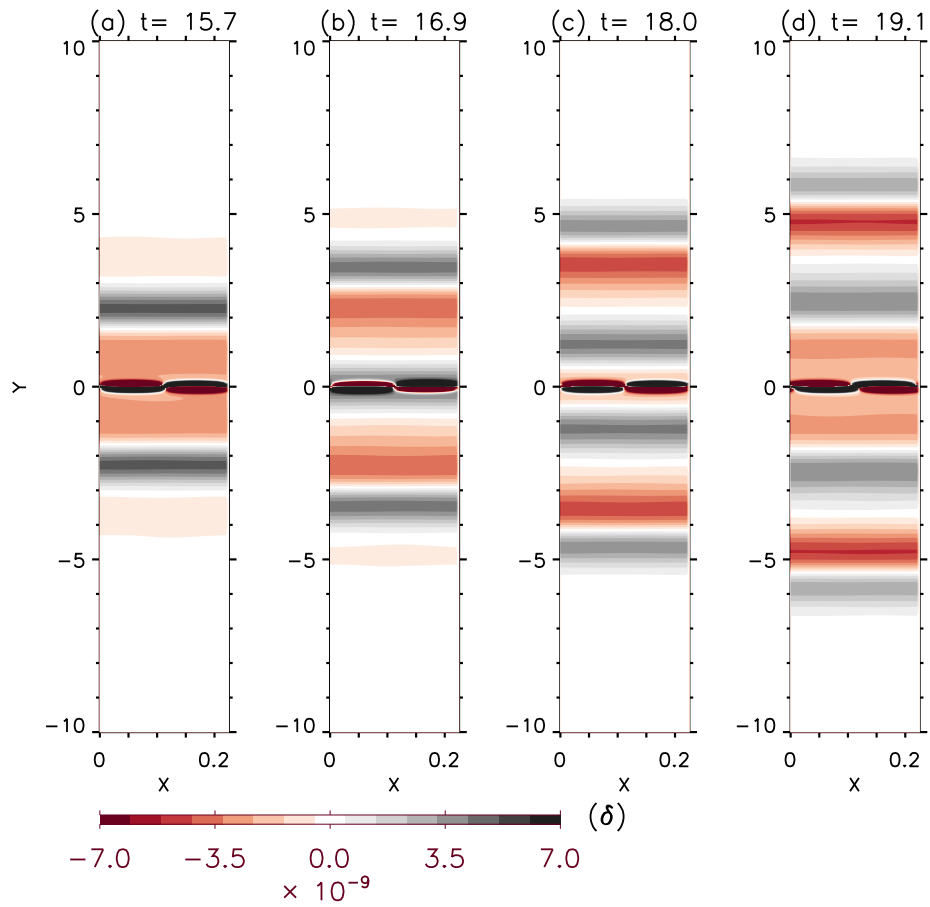
Figure 3.20: Same as figure (3.15), but now shown over a much wider meridional domain to show wave progress at later times.
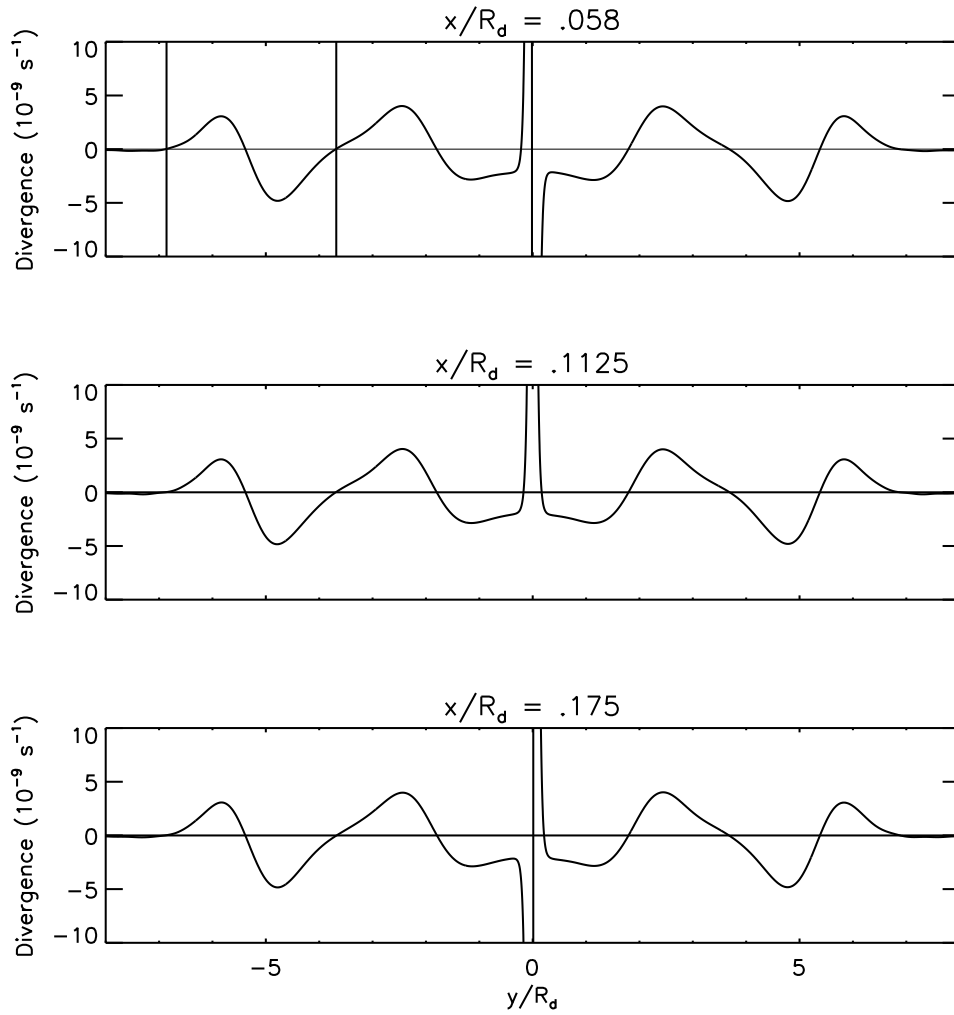
Figure 3.21: Figure showing the meridional cross-section of δ-wave along lines $x =$ .058, .114, and .17, respectively, in fig. 3.20 (d).

from regions of positive divergence, which can be indentified as *sources*, and ending in regions of negative divergence or convergence, which can be identified as *sinks*. Therefore, in each frame one can identify two pairs of *source* and *sink*, therefore, constituting a *quadrupole source* (see e.g., Lighthill, 1978). Furthermore, we observe that frames (a) to (c) show that wind diverging from the *source* region is stronger compared to the winds converging into the *sinks*, suggesting that mass is being expelled by the divergent wind to regions beyond the near-field region. Frame (d), in contrast, shows stronger wind vectors converging to the *sink* and
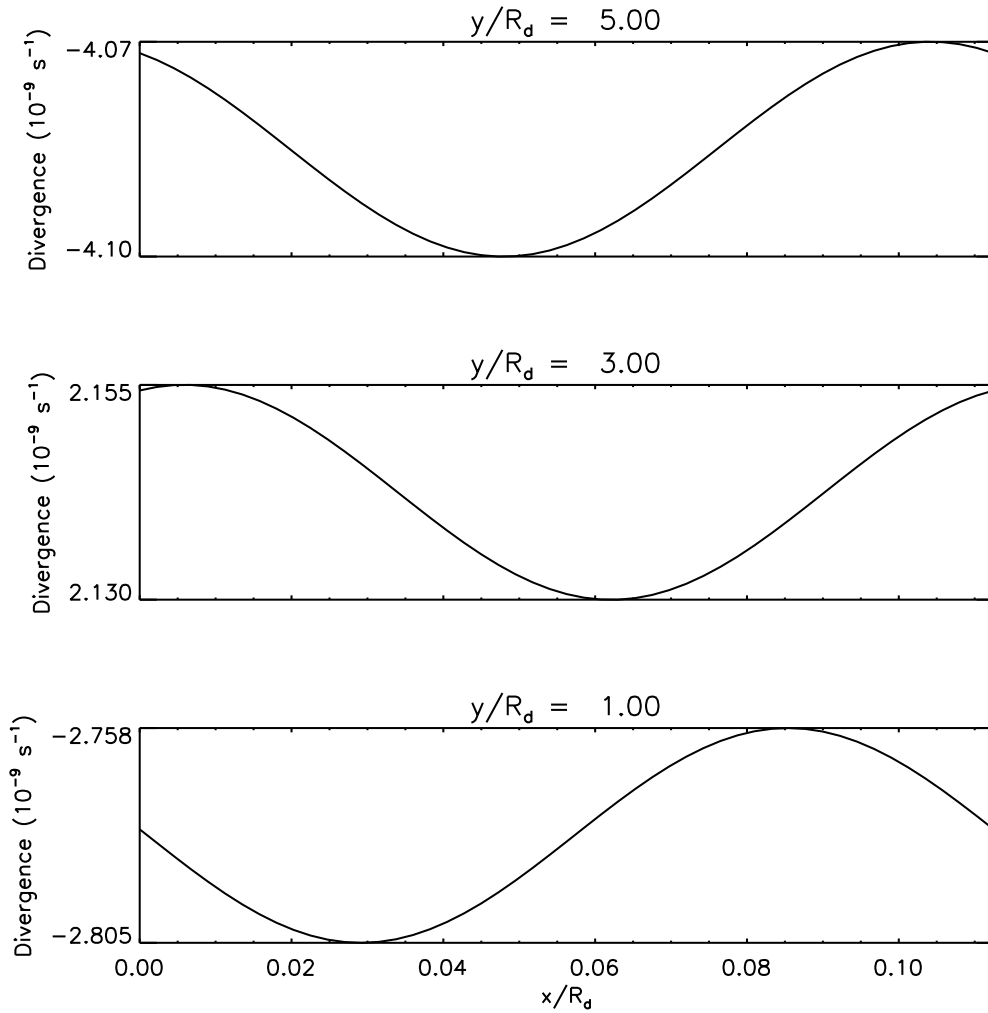
Figure 3.22: Figure showing the zonal cross-section of δ-wave along lines $y/R_d = 1$, 3, and 5, respectively, in fig. 3.20 (d).

the wind vectors diverging from the *sources* are relatively weaker.

An important characteristic of a *quadrupole source* is that it must conserve both mass and momentum (see e.g., Lighthill, 1952, 1978). The simulated vortex satisfies both this characteristics, because there is no source of external mass, nor is there an external force driving the oscillations. Now a static *quadrupole source* and the wind field associated with it cannot radiate. So, it is important that the strength or intensity of the sources and sinks fluctuate so that the wind field associated with them also fluctuates, making it possible for the quadrupole source
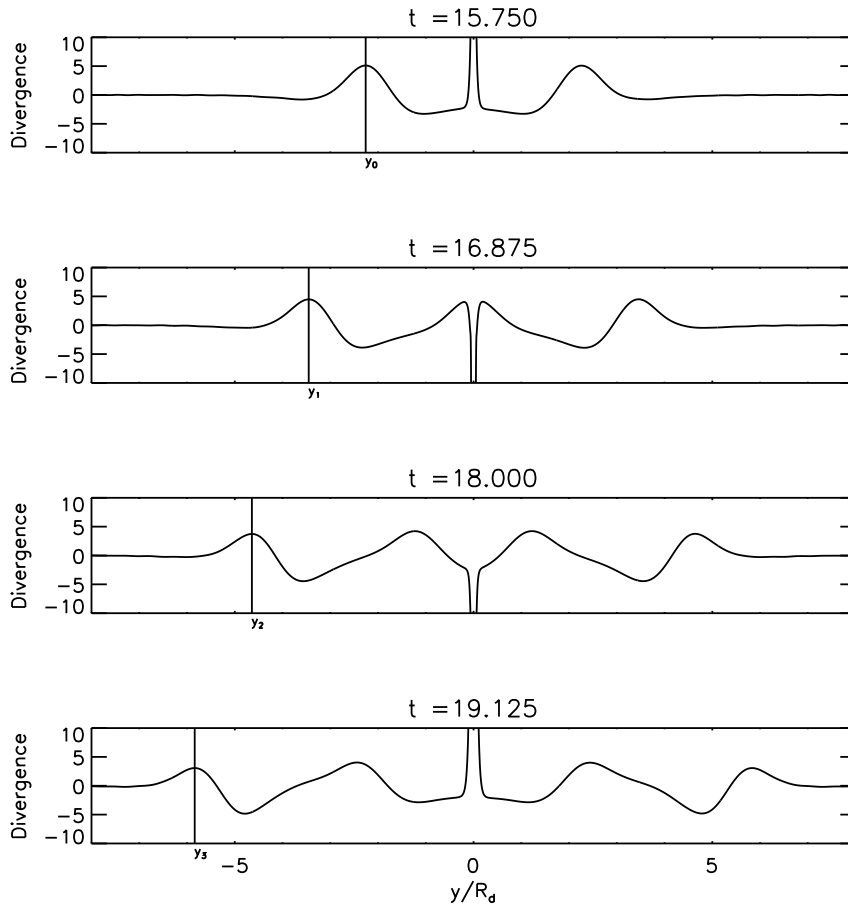
Figure 3.23: Figure showing the propagation of the δ-wave along line $x = .1125$ in fig. 3.20. The letters y_0, y_1, y_2, and y_3 indicate the position of the crest during propagation of the wave. $y_0 = $ -2.259R_d, $y_1 = $ -3.4515R_d, $y_2 = $ -4.64176R_d, $y_3 = $ -5.83875R_d.

to radiate.

Insight into whether the oscillations in the *quadrupole source* is the driving force responsible for producing the shallow-water gravity waves, or whether these oscillations in the divergence field arise as a consequence of some other forcing mechanism, will be obtained after we have performed a detailed investigation of the fluctuations in the perturbation field in section (3.4.3).

Importantly, in order to verify that the simulated δ-field is an integral feature associated with the evolution of an unstable PV-strip and not a consequence
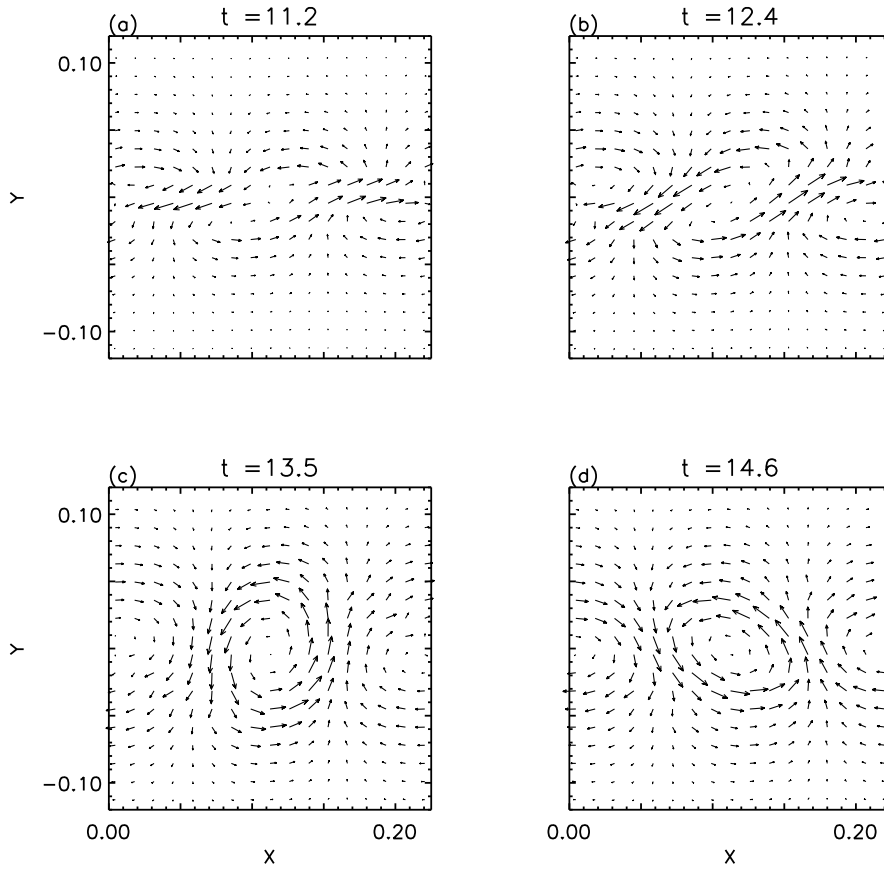
Figure 3.24: Figure shows the evolution of the perturbation wind field **v**′. The magnitude longest wind vector shown is ≈ 2.18 m/s.

of numerical errors, its sensitivity with respect to model resolution and dissipation is investigated in section (3.5).

3.4.2   Intermediate and far-field fluctuations

So far we have only looked at near-field features associated with the evolution of the vortices, which span distances well within the Rossby radius of deformation. We now look at features in the intermediate and far-field region, which dominate the region beyond the scale of the vortices. By *intermediate region* we are referring to distance within the Rossby radius, but outside the vortical region. Distances
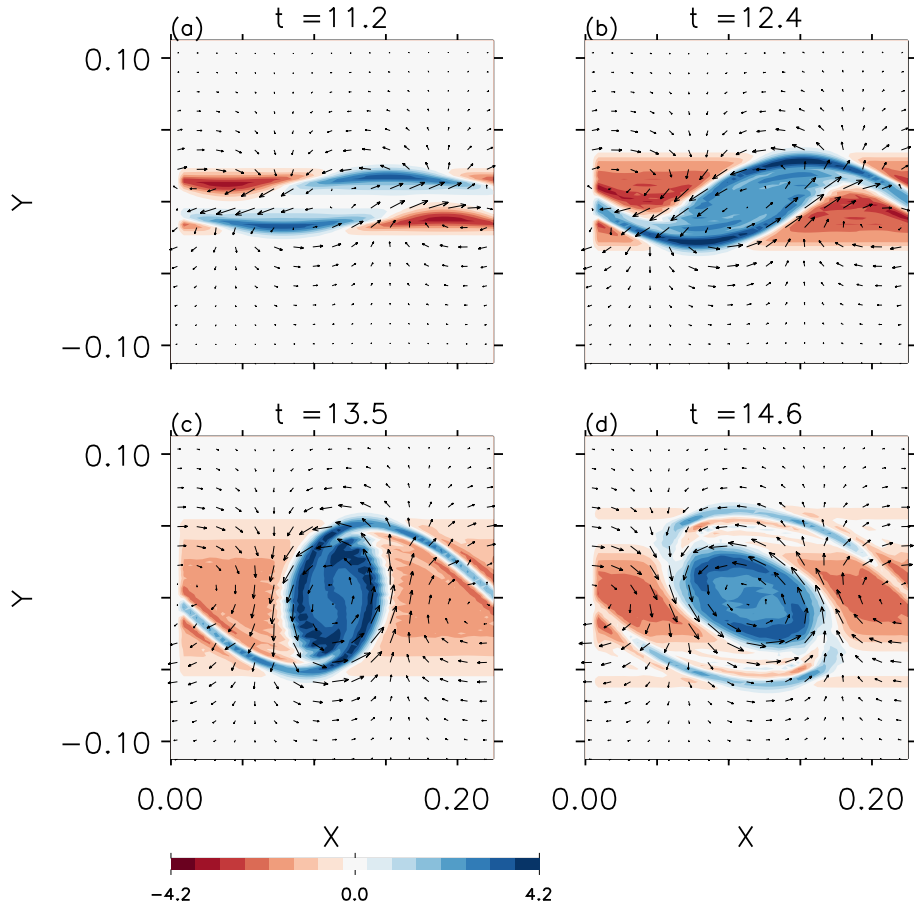
Figure 3.25: Figure showing the evolution of perturbation vorticity ζ' field, where $\zeta' = \zeta - \bar{\zeta}$. ζ' is in unit of f. The perturbation wind vector $\mathbf{v}'$ is overlaid on it.

beyond the Rossby radius will be referred to as the far-field region. Our reason for separating the region beyond the vortical region into intermediate and far-field region will soon become evident.

Fig. (3.14) shows the divergence in the intermediate-region at the same time as in fig. (3.10). We observe that the strong divergence field with magnitude on the order of 10^{-7} s^{-1} is confined to the near-field. However, when the contour value range is reduced by almost two orders of magnitude in fig. (3.15), we find in the intermediate region small amplitude shallow-water gravity waves with long
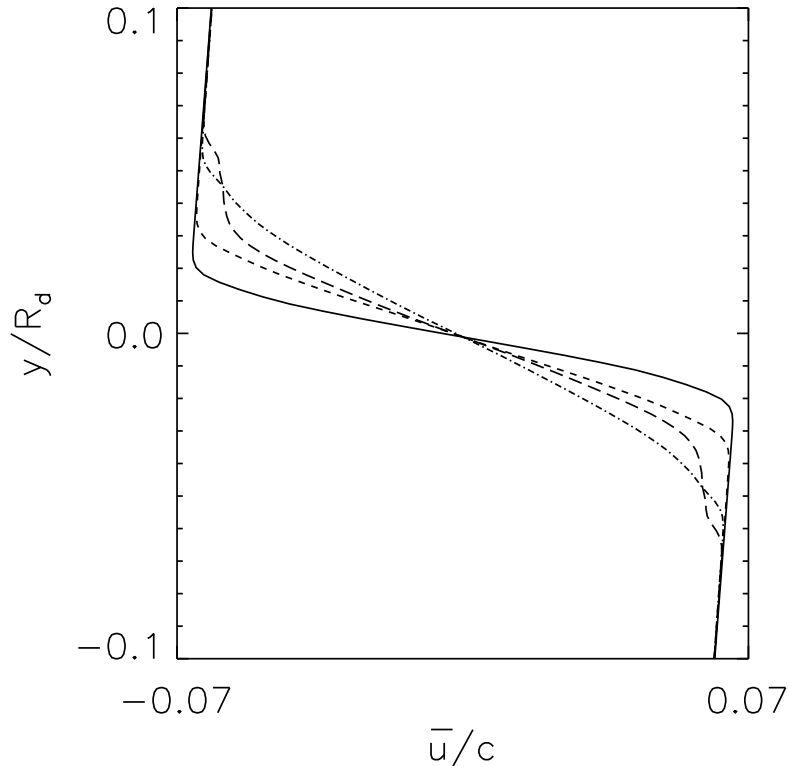
Figure 3.26: Plot showing the evolution of the mean zonal wind $\bar{u}$. Mean flows at times $t = 11.2$ (Solid line), $t = 12.4$ (Dotted line), $t = 13.5$ (Dashed line), and $t = 14.6$ (Dotted-dashed line) are shown. The maximum $\bar{u}/c = .0661$.

meridional wavelengths propagating away from the vortices in the near-field. (Note that in this figure divergence field with values outside this range have been assigned the extreme values of the new contour range.)

We also observe that the propagating waves tend to have relatively weak zonal variations, even though the near-field divergence showed strong zonal variations. In order to understand this, we again look at the contributions of $\partial_x u$ and $\partial_y v$ fields to the resulting δ field. Figs. (3.16) and (3.17) show the $\partial_y v$ and $\partial_x u$ fields, respectively, in the intermediate region. We observe that both $\partial_y v$ and $\partial_x u$ show strong zonal variations (though, smaller compared to the near-field) even in the intermediate region. The zonal variations associated with these field are
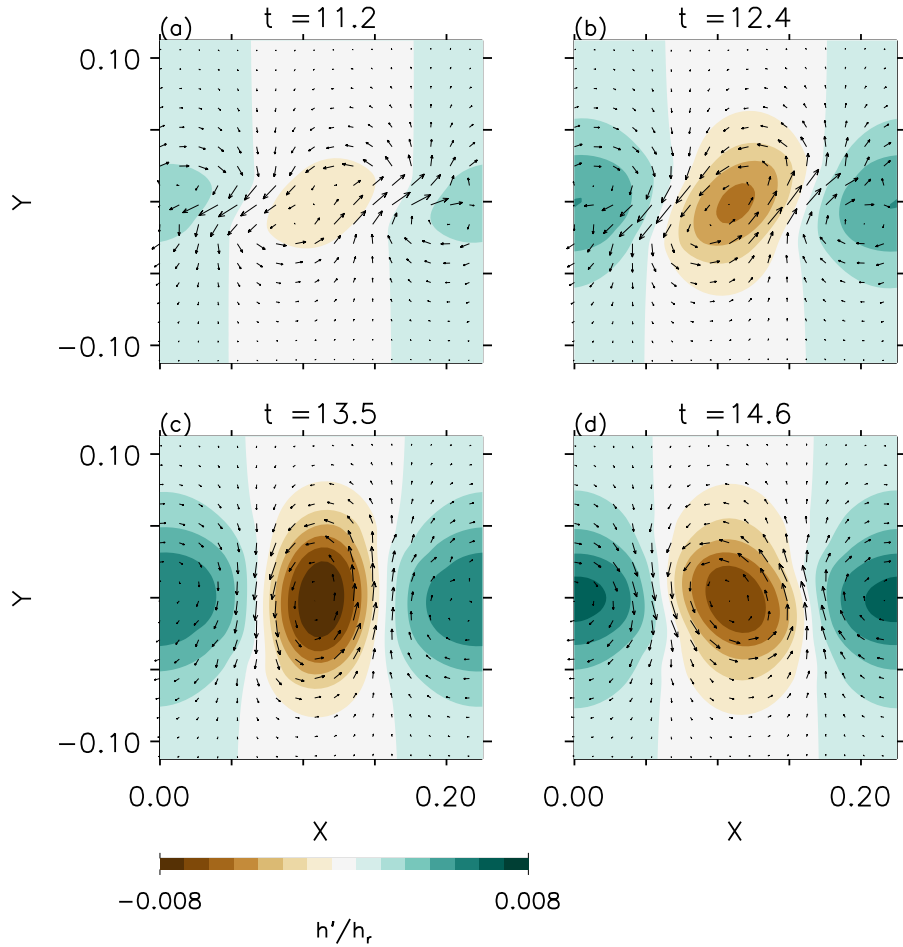
Figure 3.27: Figure showing the height fluctuation h'/h_r, where $h' = h[x, y, t]$ - $\bar{h}[y, t]$. Also shown is the perturbation wind field $\mathbf{v}'$.

such that they cancel each other, which explains the lack of zonal variation in the intermediate δ-field.

Importantly, contrary to the near-field, the contribution to the δ in the intermediate region comes primarily from $\partial_y v$. This implies that the divergent field is responsible for transport of mass beyond the near-field or the vortical region, but does so in a conservative manner.

Next we look at the far-field features. Figs. (3.18) and (3.19) show the $\partial_y v$ and $\partial_x u$, respectively in the far-field. Interestingly, we observe that fluctuations
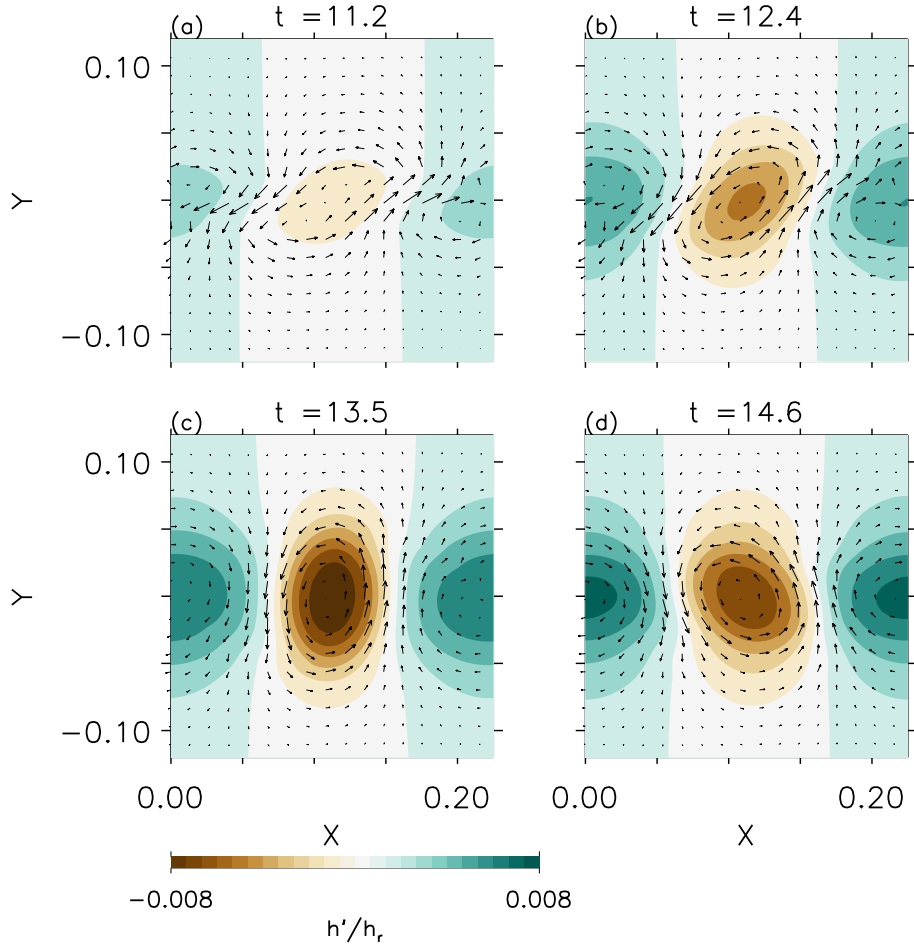
Figure 3.28: Same as fig. (3.27), but shown is the perturbation *rotational* wind $\mathbf{v}'_\psi$ is shown (see expression (3.58) for definition of $\mathbf{v}'_\psi$). The wind speed maximum is ≈ 2.18 m/s.

in the $\partial_x u$-field remain confined to the intermediate region, and does not extend any further. Even with the $\partial_y v$-field, we observe that zonally varying components remain confined to the intermediate region, and it's only the zonally independent component of $\partial_y v$ which contributes to the propagating shallow-water waves. This a very important result, because it implies that gravity waves originate as a consequence of forcing in the meridional direction. This inference is further supported, as will be shown later, by results in section (3.4.3).

Fig. (3.20) shows the meridional propagation of these waves at later times. Figs. (3.21) and (3.22) show the meridional and zonal cross-section, respectively,
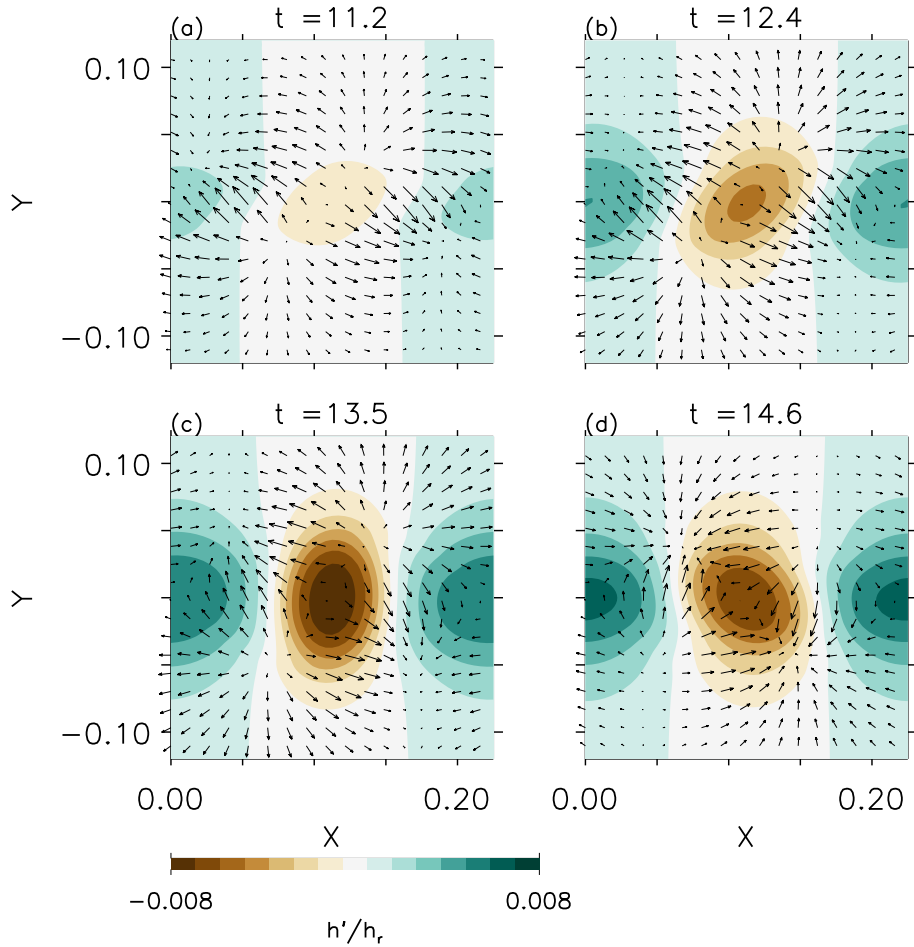
Figure 3.29: Same as fig. (3.27), but shown is the perturbation *divergent* $\mathbf{v}'_\chi$ wind (see expression (3.58) for definition of $\mathbf{v}'_\chi$). The wind speed maximum is $\approx$ .002 m/s.

of the waves shown in fig. (3.20) (d).

We observe some distinct features associated with these waves. These waves have long meridional wavelengths compared to the spatial scale of the vortical region. The meridional wavelength of the emitted wave is at least twice the Rossby radius R_d. In fig. (3.21) the distance between the vertical solid lines is equal to $3.18R_d$, which can be used to make an estimation of the wavelength. The zonal wavelength of the wave is equal to the length of the zonal domain, and the amplitude of the zonal variation is smaller by almost a factor of 10^2 in comparison
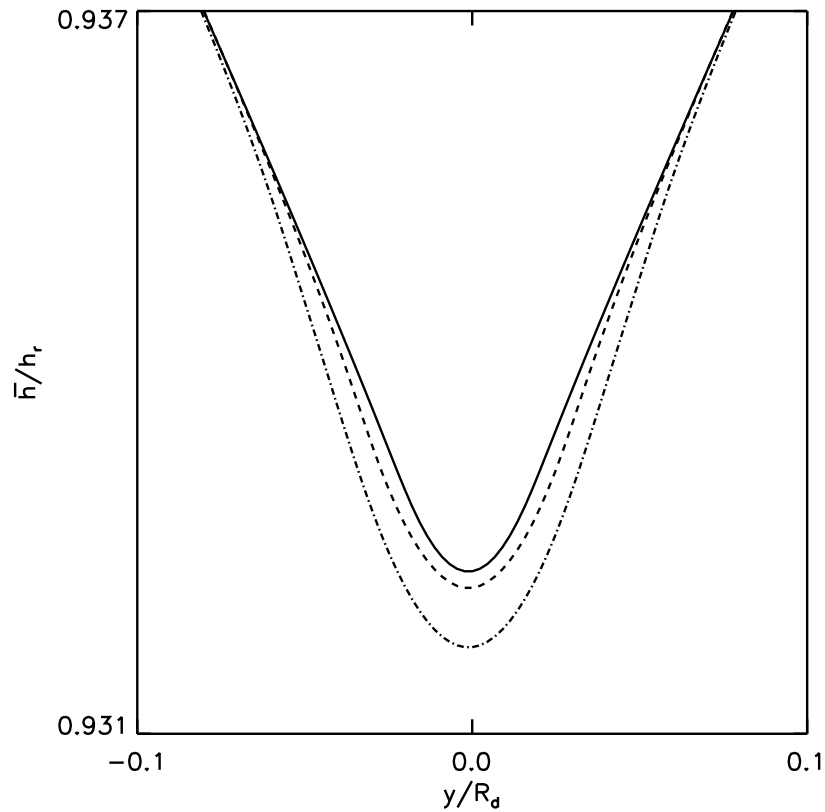
Figure 3.30: Plot showing the evolution of the meridional cross section of the normalized mean zonal height $\bar{h}/h_r$. Mean height at times $t = 11.2$ (Solid line), $t = 12.4$ (Dashed line), and $t = 13.5$ (Dot-dashed line) are shown.

to the meridional wave amplitude.

One can also make an estimate of the phase speed. Fig. (3.23), which tracks the location of the crest of the leading wave was used to make an estimate of the phase speed. The crest propagates with a speed of about 31.8 m/s, which compares well with the non-rotating shallow-water gravity wave phase speed $\sqrt{gh_r}$ = 30 m/s for an undisturbed fluid.
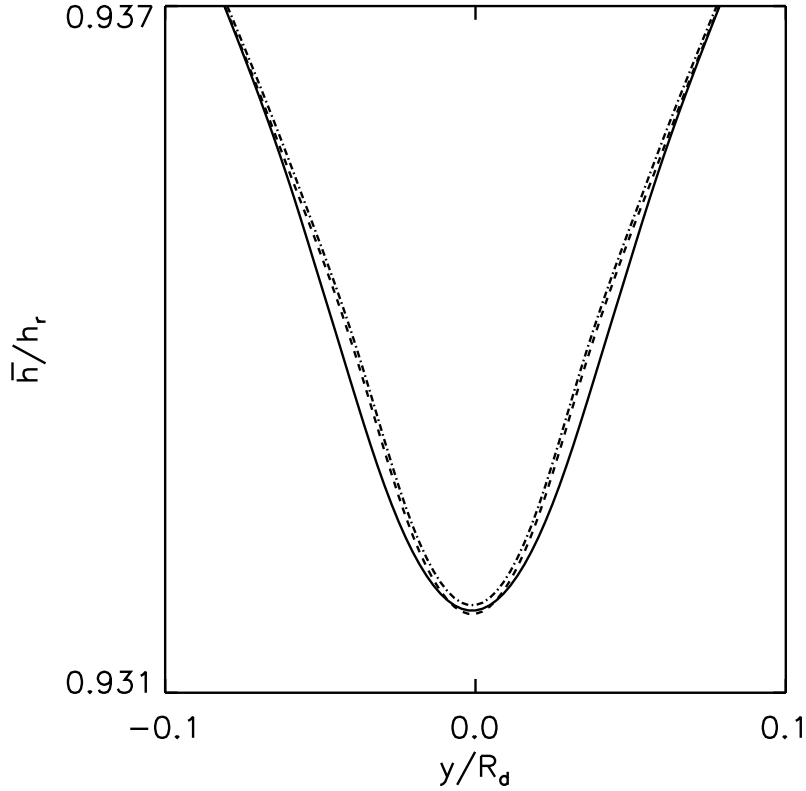
Figure 3.31: Same as fig. (3.30), but at later times showing the increase in the vortical region. Mean height at times $t = 14.6$ (Solid line), $t = 15.8$ (Dashed line), and $t = 17.0$ (Dot-dashed line) are shown.

3.4.3 Evolution of the perturbation fields and the wave forcing mechanism

So far our investigation into the mechanism of gravity wave generation have indicated oscillation in the near-field divergence as a possible source for driving gravity waves. However, it is not yet clear what drives these oscillations. In order to gain some insight, we now focus our attention towards understanding fluctuations in the vorticity field.

Fig. (3.8) showed the evolution of the ζ-field during the growth of the perturbations. The total vorticity field is comprised mainly of positive vorticity, but
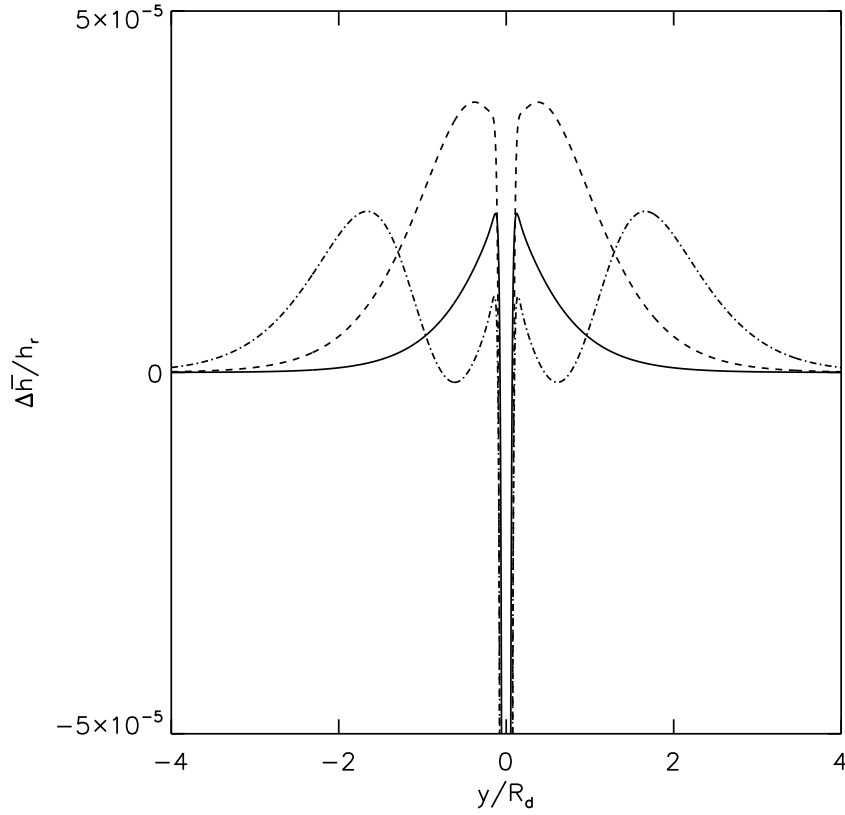
Figure 3.32: Plot showing the evolution of the difference in normalized mean zonal height $\Delta\bar{h}[t]/h_r$ ($= \bar{h}[t]/h_r$ - $\bar{h}[t=11.2]/h_r$). $\Delta\bar{h}$ at times $t = 12.4$ (Solid line), $t = 13.5$ (Dashed line), and $t = 14.6$ (Dot-dashed line) are shown.

also showed thin regions with negative vorticity (visible as faint brown lines on either side of the braids in frames (b), (c), and (d)). Positive vorticity is associated with cyclonic wind circulation and negative vorticity with anticyclonic wind circulation. The anticyclonic circulations associated with this negative vorticity were not evident in the wind field. However, they become visible when the zonal mean flow ($\bar{u}$) is subtracted from the wind field $\mathbf{v}$. Fig. (3.24) shows evolution of the perturbation wind field vector $\mathbf{v}'$, where

$$\mathbf{v}'[x, y, t] = (u[x, y, t] - \bar{u}[y, t], v[x, y, t])).\qquad(3.55)$$

The perturbation wind field is comprised of a cyclonic circulation at the center

97

and anticyclonic circulations on the sides. These circulations are initially weak (see frames (a) and (b) of fig. 3.24), but intensify with time during the roll-up of the vorticity strip. This indicates that significant features associated with the evolution of the flow field were masked by the mean zonal flow. This motivates us to discuss features associated with the evolution of the perturbation flow field.

Fig. (3.25) shows the evolution of the perturbation vorticity field ζ', where

$$\zeta'[x, y, t] = \zeta[x, y, t] - \bar{\zeta}[y, t] \tag{3.56}$$

The perturbation wind field $\mathbf{v}'$ has been overlaid on the ζ'-plots. Frame (a) shows that initially the perturbation vorticity is concentrated along thin regions on either side of the $y = 0$ axis. Definition (3.56) implies that the zonally-averaged ζ' is zero, which further implies that integral of ζ' over the entire domain is also zero. This implies that the circulation C' associated with the perturbation wind field $\mathbf{v}'$ is zero, where $C' = \oint \mathbf{v}' \cdot \mathbf{dx}$, and $\mathbf{x}$ indicates the position vector.

The next frame, i.e., fig. (3.25) frame (b), shows that both the cyclonic and anticyclonic circulations have intensified, and so has the perturbation wind field $\mathbf{v}'$. Since C' is again zero, it implies that the intensification of the cyclonic perturbation circulation must be accompanied by intensification of equal amount of anticyclonic perturbation circulation. This indicates that the evolution of the C' follows *Kelvin's circulation theorem*. *Kelvin's circulation theorem* states that in a barotropic fluid, i.e., fluids in which density is a function of pressure alone, the circulation is conserved, in the absence of viscosity (see e.g., Holton 2004).

The increase in intensity of the perturbation wind field $\mathbf{v}'$ implies that the perturbations have gained kinetic energy. Fig. (3.26) shows the evolution of the zonal mean wind $\bar{u}$. The zonal mean wind $\bar{u}$ decreases during the intensification of the circulations, indicating that the perturbations are intensifying at the expense

98

of the zonal mean kinetic energy.

Now the intensification of the cyclonic circulation must be accompanied by expulsion of mass and deepening of the low-pressure center, and the anticyclonic circulations by accumulation of mass. Fig. (3.27) shows the evolution of the perturbation height field h', where

$$h'[x, y, t] = h[x, y, t] - \bar{h}[y, t], \tag{3.57}$$

and $\bar{h}$ is the zonal averaged height field. Figure shows that the intensification of cyclonic circulation is indeed accompanied by deepening of the low-pressure center, and the anticyclonic circulations are accompanied by accumulation of mass.

The subsequent evolution of the perturbation height field h' can be understood as follows. In frames (a) and (b) of fig. (3.27), the perturbation wind can be seen spiraling out of the deepening low-pressure center, and then blowing across contours of constant h', and feeding into the intensifying high-pressure regions. After the initial intensification phase of the vortices, the perturbation wind pattern continues to evolve, as is evident in the transition from frame (b) to (c). Frame (c) shows that the perturbation wind is flowing more closely along the lines of constant h'-contours, indicating that the vortices have reached their mature stage and no further intensification of h' can occur.

Importantly, during this phase we also observe that the meridional wind v' is now blowing right across lines of mean zonal height $\bar{h}$ (not visible in Fig. (3.27)). Such cross-isobaric flow must result in some transfer of mass and produce fluctuations in mean zonal height in the near-field region. As will be demonstrated shortly, this indeed results in significant meridional transfer of mean zonal mass.

Since the perturbation wind field ($\mathbf{v}'$) shown in figure (3.27) comprises both
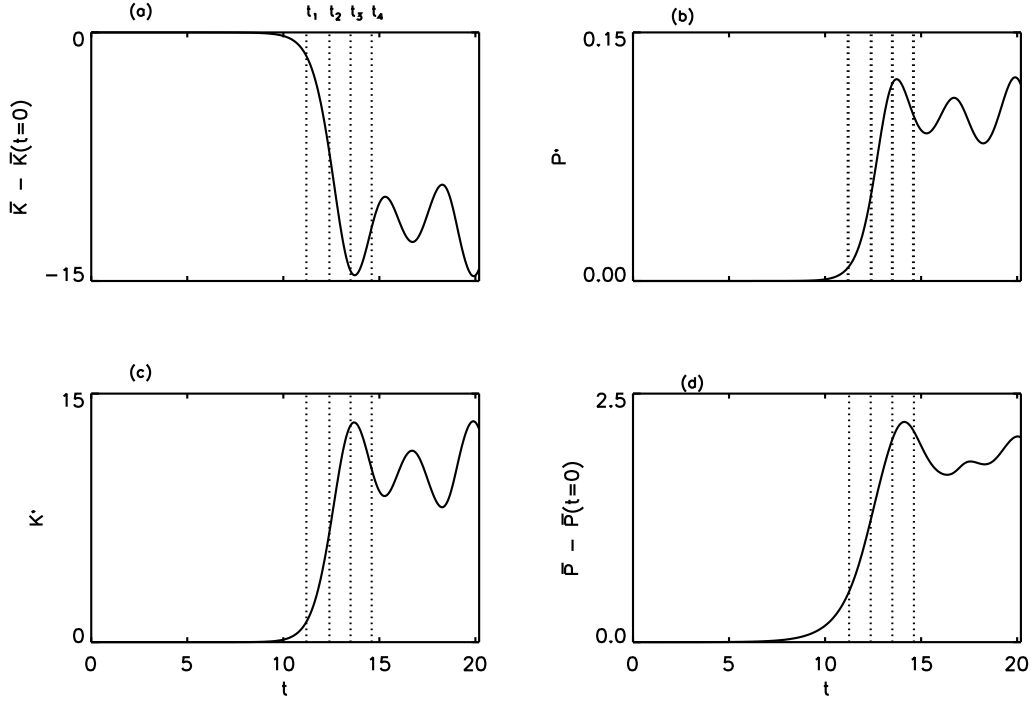
Figure 3.33: Temporal variations of the (a) $\bar{K} - \bar{K}(t=0)$, (b) P', (c) K', (d) $\bar{P} - \bar{P}(t = 0)$. Letters t_1, t_2, t_3, and t_4 indicate the times $t = 11.2, 12.4, 13.5, 14.6$, respectively.

the vortical and divergent wind component, the fluctuation in the perturbation height (h') must arise as a consequence of both the vortical and divergent fluid motions. Figs. (3.28) and (3.29) show the evolution of the h'-field with the wind fields $\mathbf{v}'_\psi$ and $\mathbf{v}'_\chi$ overlaid on it, respectively, where

$$\mathbf{v}' = \mathbf{v}'_\psi + \mathbf{v}'_\chi, \tag{3.58}$$

$\mathbf{v}'_\psi = (\hat{\mathbf{k}} \times \nabla \psi)$ and $\mathbf{v}'_\chi = \nabla \chi$, ψ is a stream function for the rotational part of $\mathbf{v}'$ and χ is a velocity potential for the divergent part of $\mathbf{v}'$, so that $\nabla^2 \psi$ and $\nabla^2 \chi$ are vorticity (ζ) and divergence (δ), respectively.

It is evident from figs. (3.27) and (3.28) that the wind fields $\mathbf{v}'$ and $\mathbf{v}'_\psi$ are

100

almost identical. This is because $|\mathbf{v}'_\chi|$ is smaller by a factor of almost 10^3 compared to $|\mathbf{v}'_\psi|$, indicating that almost all of the adjustment in the near-field mass/pressure field is produced by rotational fluid motions, and the divergent component of the wind $\mathbf{v}'_\chi$ aids in small but further adjustment of the mass field. Also evident is that the wind field $\mathbf{v}'_\psi$ is more confined to the center of the domain, and weakens considerably in the meridional direction. In contrast, $\mathbf{v}'_\chi$, which is very small in magnitude compared to $\mathbf{v}'_\psi$, doesn't show signs of weakening in the meridional direction.

However, the subsequent frame of fig. (3.27), i.e., frame (d) at $t = 14.6$, shows that the perturbation height field continues to evolve. Furthermore, since there is no boundary to obstruct the meridional transport of mass, it can be expected that a small portion of the fluid propagates deeper into the meridional direction, beyond the meridional domain shown in fig. (3.27).

When the perturbation wind pattern in fig. (3.27), frame (b) is compared with the wind pattern in frame (d), we observe that the direction of mass transfer has reversed. In the latter case, wind (i.e., $\mathbf{v}'_\psi$) can be seen spiraling out of the high-pressure region and feeding into the low-pressure center, indicating that this is a decaying phase for the vortices.

Next we investigate the fluctuations in the near and intermediate field mean zonal height $\bar{h}$ produced by the cross-isobaric flows.

Since the zonal domain is periodic, if mass transfer occurred only along the zonal direction, then this would imply that mean zonal height $\bar{h}$ will remain unchanged during this process. Fig. (3.30) shows the evolution of the meridional cross-section of the mean zonal height $\bar{h}$. The plot shows that $\bar{h}$ decreases during the intensification phase of the vortices, which implies that the domain shown in fig. (3.27) is losing mass.

The change in local $\bar{h}$ is caused by the meridional transport of mass by the rotational component of the wind and is too small to be visible in the $\bar{h}$-plot. In order to view the transport of mass in the meridional direction, the change in the zonal mean height $\Delta\bar{h}$ is plotted. Fig. (3.32) shows the meridional cross-section of change in mean zonal height $\Delta\bar{h}$, where

$$\Delta\bar{h}(t) = \bar{h}(t) - \bar{h}(t = 11.2). \tag{3.59}$$

Figure shows that from time $t = 11.2$ to 12.4 mass is being expelled from the vortical region. This is evident from the positive value of $\Delta\bar{h}$ in the region immediately outside the vortical region. Earlier, our analysis of the *rotational* and *divergent* winds showed that the rotational wind remain confined to the near-field, whereas divergent wind propagates deep into the intermediate region. Therefore, the near-field fluctuation in the mean height $\bar{h}$ must have been produced by the cross-isobaric flow of the rotational wind, and the meridional transport in the intermediate region must have been caused by the divergent wind.

The subsequent evolution of $\Delta\bar{h}$, i.e., at $t \approx 13.5$ (indicated by dashed line), shows that more mass is expelled from the vortical region, which is evident from the further increase in $\Delta\bar{h}$ in the region around the vortices. Figure also shows that although bulk of the expelled mass is confined to the region around the vortices, the leading edge has spread over a distance of almost $3R_d$ (indicated by the dashed-line).

The $\Delta\bar{h}$-plot at a later time, i.e., at $t = 14.6$, indicates that the expulsion of mass from the vortical region has ceased. This is evident from the observed drop in $\Delta\bar{h}$ in the region immediately outside the vortices (indicated by the transition from dashed line to dot-dashed line). Furthermore, since fig. (3.31) shows that after time $t = 13.5$ the zonal mean height $\bar{h}$ is increasing in the vortical region,

this implies that the mass that was expelled is now receding back to the vortices. Since $\Delta\bar{h}$ indicates the change in the value of $\bar{h}$ relative to value of $\bar{h}$ at $t = 11.2$, then the fact that the value of $\Delta\bar{h}$ remains negative in the vortical region in fig. (3.32) implies that the lost mass fails to completely recover. As is shown later, this interpretation is further supported by the potential energy plots.

Note that the vortical region is confined to a narrow region around the line $y = 0$ and spans a distance of less than $0.2R_d$ relative to the scale of the y-axis range of fig. (3.32) which spans of distance of $8R_d$.

As the mass recedes back to the vortices following the reversal of the divergence field, the disturbance continues to propagate towards the meridional boundaries as shallow-water gravity waves, as is evident from the subsequent evolution of $\Delta\bar{h}$ in fig. (3.32). The positive $\Delta\bar{h}$ bump visible in the dot-dashed line of fig. (3.32) nicely captures the propagation of the leading edge of the wave front. Therefore the fluid system is losing energy in the form of gravity waves, while total mass remains conserved.

In the following subsection, we look at the energetics associated with the evolution of the simulated vortex.

3.4.4   Energetics

The expression for the energy per unit area (E) of the shallow-water equations is

$$E \;=\; \frac{1}{2}h(u^2 + v^2) + \frac{1}{2}gh^2, \tag{3.60}$$

where the first term represents kinetic energy (K) and the second term represents potential energy (P). The field variables and the energies may be separated into

zonally-averaged and perturbation parts. Then substituting $u = \bar{u}[y,t] + u'[x,y,t]$, $v = v'[x,y,t]$, and $h = \bar{h}[y,t] + h'[x,y,t]$, in the expression in (3.60), we get

$$
\begin{aligned}
E &= \frac{1}{2}(\bar{h} + h')\left((\bar{u} + u')^2 + v'^2\right) + \frac{1}{2}g(\bar{h} + h')^2 \\
&= \frac{1}{2}\bar{h}\bar{u}^2 + \bar{h}\bar{u}u' + \frac{1}{2}\bar{h}(u'^2 + v'^2) + \frac{1}{2}h'\bar{u}^2 + h'\bar{u}u' + \frac{1}{2}h'(u'^2 + v'^2) \\
&\quad \frac{1}{2}g\bar{h}^2 + g\bar{h}h' + \frac{1}{2}gh'^2
\end{aligned}
\tag{3.61}
$$

where overbar indicate zonal averaging and prime indicate deviation from the zonal mean. Upon domain averaging, the terms $\bar{h}\bar{u}u'$, $h'\bar{u}^2/2$, and $g\bar{h}h'$ disappear because they are linear in perturbation variables. In what follows the domain averaged terms will be denoted by angle brackets $\langle ... \rangle$. Therefore the domain averaged mean kinetic energy $(\bar{K})$ is

$$
\bar{K}[t] = \left\langle \frac{1}{2}\bar{h}\bar{u}^2 \right\rangle,
\tag{3.62}
$$

perturbation kinetic energy (K'),

$$
K'[t] = \left\langle \frac{1}{2}\bar{h}(u'^2 + v'^2) \right\rangle + \left\langle \frac{1}{2}h'(u'^2 + v'^2) \right\rangle + \langle \bar{u}h'u' \rangle,
\tag{3.63}
$$

mean potential energy $(\bar{P})$,

$$
\bar{P}[t] = \left\langle \frac{1}{2}g\bar{h}^2 \right\rangle,
\tag{3.64}
$$

and perturbation potential energy (P') is

$$
P'[t] = \left\langle \frac{1}{2}gh'^2 \right\rangle,
\tag{3.65}
$$

where the averaging operators $\langle \ \rangle$ and is defined as

$$\langle \ \rangle = \frac{1}{2L_x L_y} \int_0^{L_x} \int_{-L_y}^{L_y} (\ )dydx \tag{3.66}$$

where L_x is the length of zonal domain and $2L_y$ is meridional extent of the domain.

Fig. (3.33) shows the evolution of $\bar{K}$, K', $\bar{P}$, and P' for simulation $S1$. Plot (3.33) (a) shows that $\bar{K}$ remains undisturbed initially for a certain period of time and then begins to decrease in amplitude. This decrease in $\bar{K}$ occurs due to decrease in both $\bar{u}$ and $\bar{h}$ in the near-field or vortical region. In the far-field region, $\bar{u}$ remains unchanged, but $\bar{h}$ shows a slight increase, indicating that the contribution to the loss in $\bar{K}$ comes entirely from the near-field or the vortical region. The decrease in $\bar{K}$ is accompanied by simultaneous increase in K', P', and $\bar{P}$, which indicates that $\bar{K}$ is the primary source of energy. A significant portion of the mean kinetic energy $\bar{K}$ is transferred to the perturbation kinetic energy K', a small portion of which is utilized in increasing the mean potential energy $\bar{P}$ and perturbation potential energy P'.

We saw earlier that the mean zonal mass that is lost by the vortical region, as indicated by decrease in $\bar{h}$, is transported by meridional wind perturbation v' to the far-field region. As the mass spreads in the meridional direction, it is also gaining height because the basic state height h_0 is increasing in the meridional direction. Consequently, the fluid is gaining potential energy as it propagates further in the meridional direction. Although $\bar{P}$ is lost by the near-field region, as indicated by the near-field $\bar{h}$-plot (see fig. 3.30), the domain averaged mean potential energy $\bar{P}$ still increases, which indicates that mean potential energy must be gained at the expense of the kinetic energy.

After the perturbation energies K' and P' have reached their first maximum, they begin to transfer energy back to the mean flow, as indicated by increase

in $\bar{K}$. This phase is accompanied by, as was seen in fig. (3.27) (d), decrease in meridional perturbation wind v' and the perturbation wind $\mathbf{v}'$ spiraling out of the high-pressure centers and feeding into the low-pressure region, and thus resulting in the weakening of the vortices. This explains the decrease in P' after its has attained its first maximum. This phase is also accompanied by transfer of initially expelled mass back to the vortices, as indicated by the loss in $\bar{h}$ in the region outside the vortices, and a gain in $\bar{h}$ by the vortices, which explains the decrease in $\bar{P}$. During this process, not all of the mass that was expelled recedes back to the vortical region. Consequently, not all of perturbation kinetic energy K' is transferred back to the zonal mean flow. The fluid system has thus been transferred into a state which possess less kinetic energy and more potential energy in comparison to its initial state. This new state is not steady, but is quasi-periodic, i.e., the near-field begins to undergo slow oscillations in which energy is transferred back and forth between the mean flow and the perturbations.

In summary, we observe that zonal mean kinetic is the primary source of energy which drives the circulations associated with the vortices. The initially parallel unstable flow undergoes an adjustment during which the mean kinetic energy is transferred to perturbation kinetic energy and potential energy. It is during this adjustment that a small fraction of the energy leaks as gravity waves. The final state of the fluid is a quasi-periodic state. This quasi-periodic state contains less kinetic energy and more potential energy compared to its initial state. In this respect the instability is very similar to a non-divergent barotropic instability.

3.5   Sensitivity of simulation $S1$ to resolution and dissipation

In this section we compare the effect of varying numerical discretization parameters on the evolution of the near-field and far-field features. Specifically, we consider the effect of varying resolution and dissipation.

In section (3.4.1), while discussing the near-field features of simulation $S1$, we saw that the nonlinear advection led to development of over-shoots along the leading edge of PV-front. These over-shoots are numerical errors which arises as a consequence of insufficient resolution and lack of meridional dissipation.

Fig. (3.34) shows the evolution of the meridional cross-section of the PV-front associated with the growth of the perturbations for simulation S1-R4. Simulation S1-R4 is identical to simulation S1, except for the numerical discretization parameter values, as can be seen in Table (3.3). Simulation S1-R4 illustrates the effect of increasing the resolution, i.e., grid spacing along both the x and y-directions is reduced by half compared to simulation S1, and also adding dissipation along the y-direction. Fig. (3.34) should be compared with fig. (3.7) of simulation S1 to see the significant reduction in the numerical errors as a consequence of increased resolution in the meridional (y) direction and also the effect of adding dissipation in the y-direction.

We perform two more simulations: S1-R6 and S1-R7. Simulation S1-R6 is same as S1-R4, but considers the effect of increasing dissipation. Simulation S1-R7 considers the effect of using uniform resolution and dissipation along the x and y-directions.

Fig. (3.35) compares the meridional evolution of PV-anomaly for simu-

lation S1, S1-R4, S1-R6, and S1-R7 along the line $x = .08R_d$ at approximately around the same time of the evolution. The figure shows that the amplitude of the over-shoots and oscillations visible in S1 have considerably reduced in S1-R4. S1-R6 shows that there is further improvement. S1-R7, which is expected to show the best result because of the use of higher resolution and uniform grid-spacing and dissipation properties, shows that a significant improvement in the reducing the oscillation along the trailing edge, when compared to S1, S1-R4, and S1-R6. However, we do observe that the amplitude of the spike in the leading edge has increased when compared to S1-R4 and S1-R6, but has decreased when compared to S1.

Fig. (3.36) compares the PV-field for simulations S1, S1-R4, S1-R6, and S1-R7 at time $t = 10.125$. Which helps to draw a better comparison between S1-R7 and the rest. Although we observe that R1-S7 is remarkably similar to S1-R4, we think the result in S1-R7 is still superior because the width of the spike in PV-anomaly along the leading edge (indicated by the dark blue strip) is thinnest in S1-R7.

Fig. (3.37) compares the near-field divergence field for simulations S1, S1-R4, S1-R6, and S1-R7 at time $t = 10.125$. The figure shows that the near-field divergence field is almost insensitive to the changes in resolution and dissipation. These results indicate that the observed near-field divergence are robust features associated with the intensification of vortices.

Finally, and importantly, we look at the effect of changes in resolution and dissipation on the emitted gravity waves. Fig. (3.38) compares the meridional cross-section of the gravity wave field emitted in simulations S1, S1-R4, S1-R6, and S1-R7 at time $t = 19.12$ along the line $x = 0.058R_d$. The figure shows that the oscillations observed in fig. (3.35) have negligible effect on emitted waves.

Numerical discretization parameters	Simulation			
	S1	S1-R4	S1-R6	S1-R7
Δy	675 m	337.5 m	337.5 m	337.5 m
Δx	$2\Delta y$	$2\Delta y$	$2\Delta y$	Δy
M	51	101	101	201
N	10001	20001	20001	17777
L_x	$0.225R_d$	$0.225R_d$	$0.225R_d$	$0.225R_d$
$2L_y$	$22.5R_d$	$22.5R_d$	$22.5R_d$	$19.9R_d$
Δt	5.625 s	4 s	2 s	2 s
α	.02	.02	.02	.02
D	$2.25R_d$	$2.25R_d$	$2.25R_d$	$2.25R_d$
C_n	0.25	0.36	0.18	0.18
γ_x	0.25×10^{-4}	0.022×10^{-4}	$.0625 \times 10^{-4}$	0.25×10^{-4}
γ_y	0	0.044×10^{-4}	0.25×10^{-4}	0.25×10^{-4}

Table 3.3: Table compares the numerical discretization parameter values used in simulation S1 and S1-R4, S1-R6, S1-R7

This indicates that the gravity waves observed in the numerical simulations are an integral feature associated with the instability of an unstable parallel flow in a barotropic divergent fluid, and not a consequence of numerical errors.

3.6 Summary and concluding remarks

Simulations demonstrating the emission of shallow-water gravity waves associated with the instability of an initially parallel jet were performed in a rotating (constant f-plane) shallow-water model to investigate the gravity wave generation mechanism. This chapter aimed at shedding light on the physical mechanism through which rotational wind associated with vortices result in generate wave-like

disturbances in the divergence field.

The current study revisited the problem investigated by Ford (1994a). Our aim was to perform a more detailed investigation of gravity wave emission. Consequently, important new details have been revealed, which have provided valuable new insights about the evolution of a barotropic vortex, and the process of gravity wave generation associated with an evolution of the barotropic vortex.

Specifically, our study showed that the transport of mass associated with the intensification of the vorticity field after the onset of instability is almost entirely produced by the *rotational* wind field. The rotational wind field remains confined to the near-field or vortical region, and therefore is responsible only for fluctuation in the pressure/mass field and the corresponding fluctuations in the vorticity field associated with the evolution of the vortex. More importantly, for the purpose of understanding of the source of wave forcing, this study showed that the meridional component of the *rotational* wind associated with the evolution of the vorticity field flows cross-isobaric to the zonal mean height or pressure lines. It is this cross-isobaric flow which is responsible for producing forcing for the generation of the gravity wave. This cross-isobaric flow produces fluctuation in the zonal mean height $\bar{h}$, which subsequently results in transfer of mass from the near-field region into the intermediate region. The fluctuations in this mass transfer subsequently results in generation of shallow-water gravity waves.

Our study also showed that this redistribution of mass (specifically produced by the rotational wind) occurs at the expense of the kinetic energy and results in the increase of both perturbation and mean potential energy. The fluctuation in the perturbation potential energy is associated with the intensification and relaxation of the cyclonic and anti-cyclonic circulations. But the fluctuation in the mean potential energy is produced by *rotational winds* which flow cross-

110

isobaric to the zonal mean height or pressure lines. This transports mass to the intermediate region. Therefore increasing the mean potential energy.

Our study also showed the near-field divergence field resembles a quadrupole source, i.e., it comprises of two pairs of *source* and *sink*. The study also showed that the location of these *sources* and *sinks* do not coincide with the low and high-pressure centers associated with the centers of the cyclonic and anti-cyclonic circulations, respectively, which indicates that the low and high pressure centers are not *sources* and *sinks*, and are not formed as a consequence of the intensification of the cyclonic and anticyclonic circulations and the mass transfer associated with it. Furthermore, the intensity of these *sources* and *sinks* are not stationary, but oscillate with time, and these oscillations coincide with the evolution of the vorticity field.

Our study also showed that the *divergent* wind field aids with further redistribution of the mass field, though the transport is not in the direction of the *rotational* wind. The direction of the *divergent* wind field is such that it transports mass from *source* to *sink*. In contrast to the *rotational* wind field which remains confined to the near-field region, the divergent wind is responsible for transport of mass not just in the near-field region, but also in the intermediate region.

Furthermore, our investigation into the properties of the emitted gravity wave indicated that

1. the wave showed negligible variation in the zonal direction

2. the divergence field of the propagating waves was comprised only of $\partial_y v$-field.

The fact the divergence field of the wave was comprised only of the $\partial_y v$ term further confirms that the cross-isobaric flow produced by the meridional component of the *rotational* wind is the main mechanism responsible for generating the gravity

wave. However, this study also showed that the wave forcing associated with cross-isobaric rotational flow is not uniformly distributed along the zonal direction, yet we observe that the propagating shallow-water gravity waves show negligible zonal variation.

The lack of zonal variation in the emitted shallow-water gravity wave can to some extent be understood as follows: The cross-isobaric wave forcing occurs in both the meridional directions; two oppositely directed jets could be identified between the counter-rotating vortices. The cross-isobaric flow transfers mass and produces fluctuations in the divergence fields. It is quite likely that the region where this mass got accumulated becomes a *source* and the region which has lost mass in the process acts as *sink*. Since in the case of the simulated vortex, such cross-isobaric flows are occurring on either side of the cyclonic vortex, though in opposite directions, has resulted in formation of two pairs of *source* and *sinks*. Once these pairs are formed, mass can also get transferred from *source* of one pair to the *sink* of the other pair. This would mean that the excess mass gets distributed evenly in the zonal direction, and therefore, reduces the effect of zonal variation in the wave forcing function. Such a reasoning is also supported by the observation that in the intermediate region both the $\partial_x u$ and $\partial_y v$ showed strong zonal variations, but the combined field, i.e., δ, showed negligible zonal variation. Such an inference also implies that the wind field associated with the formation of source and sinks, i.e., the *quadrupole source*, tends to diffuse the effect of the wave forcing in one particular direction.

Our study showed that the zonal term $\partial_x u$ dominates the meridional term $\partial_y v$ in the near-field region. The amplitude of zonal term $\partial_x u$ was found to be opposite in sign, but slightly greater than the meridional component $\partial_y v$. This excess of $\partial_x u$ in the near-field divergence was compensated by excess $\partial_y v$ in the intermediate field. This compensation is important, because it assures that mass

112

remains conserved.

Furthermore, the present study also investigated the effect of numerical errors, which arise as a consequence of nonlinear advection, on the wave emission mechanism. Such tests were not performed in earlier studies. The present study compared the simulation results with simulations Ai and Aii of Ford (1994a), which have the closest initial state parameters to our simulation S1. Our study showed that during the growth of the disturbance, the PV-anomaly is subject to nonlinear advection, and during this advection the slope of the anomaly steepens. This steepening is not resolved properly by the meridional grid resolution, and, consequently, leads to development of over-shoots and oscillations which extend to the trailing side of the advecting front. These over-shoots and oscillations are numerical errors.

The sensitivity of the gravity wave generation mechanism to these numerical errors was also investigated. The characteristics of the emitted waves were found to be insensitive to the increased resolution and dissipation, which indicates that errors in the evolution of the near-field potential vorticity are not important to the wave generation mechanism. This is another important finding based on our study which provides an additional insight into the wave generation mechanism observed in barotropic vortices. This insensitivity is in contrast to the gravity waves emitted by baroclinic vortices, which were found to be highly sensitive to resolution and dissipation (see e.g., Plougonven and Snyder 2005, 2006).
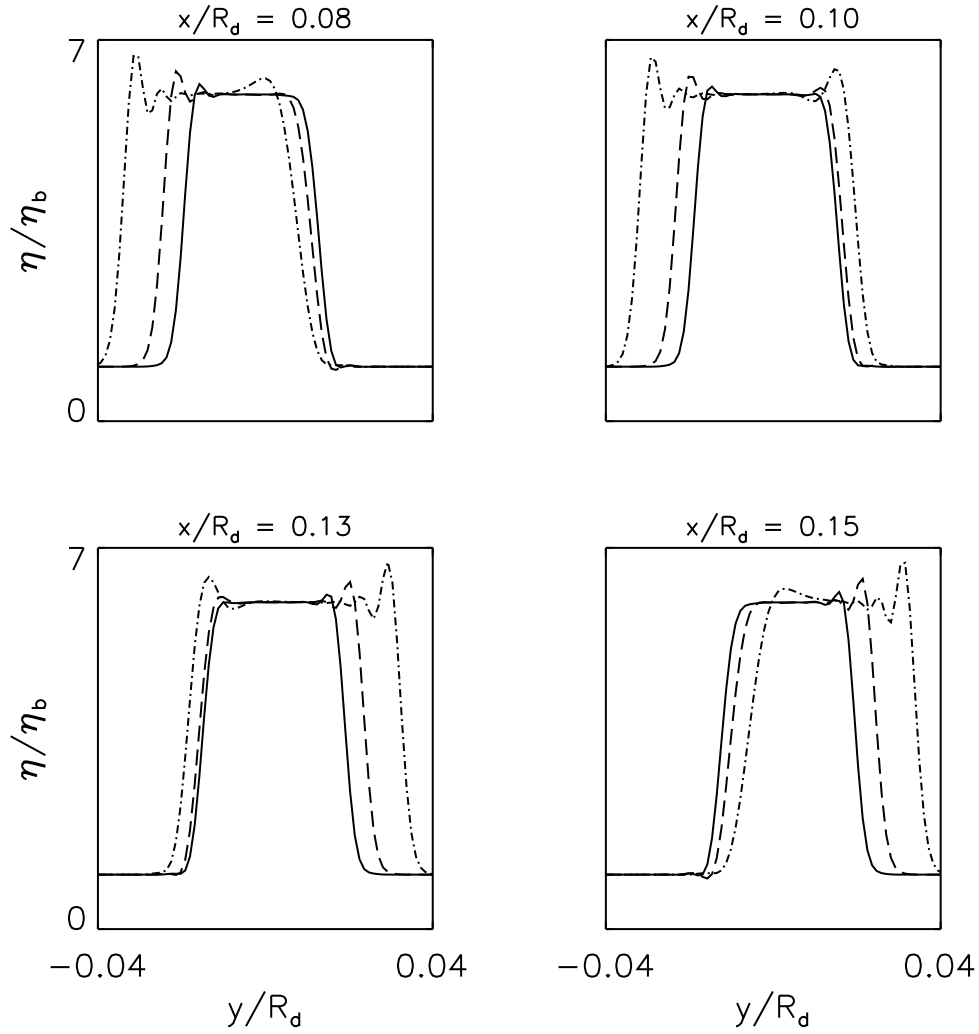
Figure 3.34: Plot showing evolution of the meridional cross-section of PV (η/η_b) for simulation S1-R4 along lines $x = 0.08$, 0.1, 0.13, and 0.15, respectively. Plots times are $t = 10.8$ (Solid-line), 11.6 (Long dash line), 12.4 (Dot-dash line).
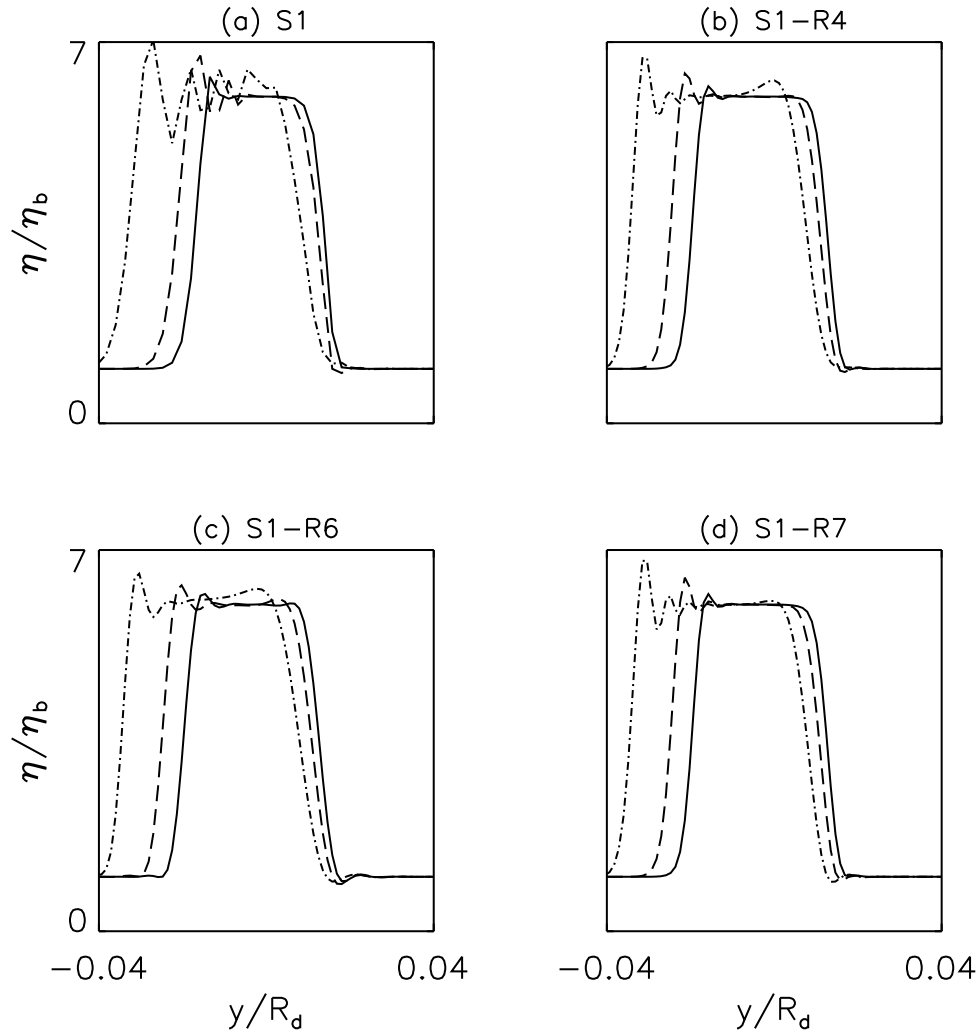
Figure 3.35: Plot comparing the evolution of the meridional cross-stream PV (η/η_b) for simulation S1, S1-R4, S1-R6, and S1-R7 along lines $x = .08$. **(a)** Plots times are $t = 10.125$ (Solid-line), 11.25 (Long dash line), 12.375 (Dot-dash line); **(b)**, **(c)**, and **(d)** Show plots at times $t = 10.8$ (Solid-line), 11.6 (Long dash line), 12.4 (Dot-dash line)
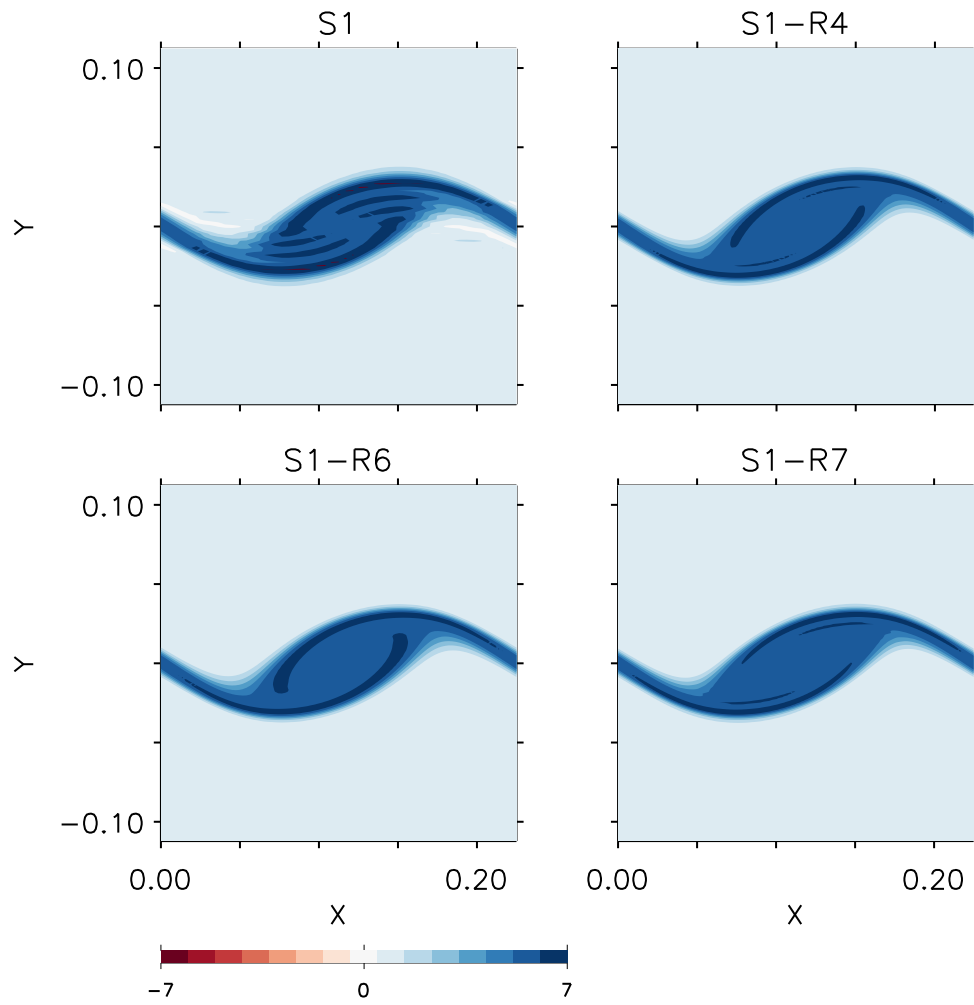
Figure 3.36: Plot comparing the normalized potential vorticity η/η_b for simulation S1, S1-R4, S1-R6, and S1-R7 at time $t = 10.125$.
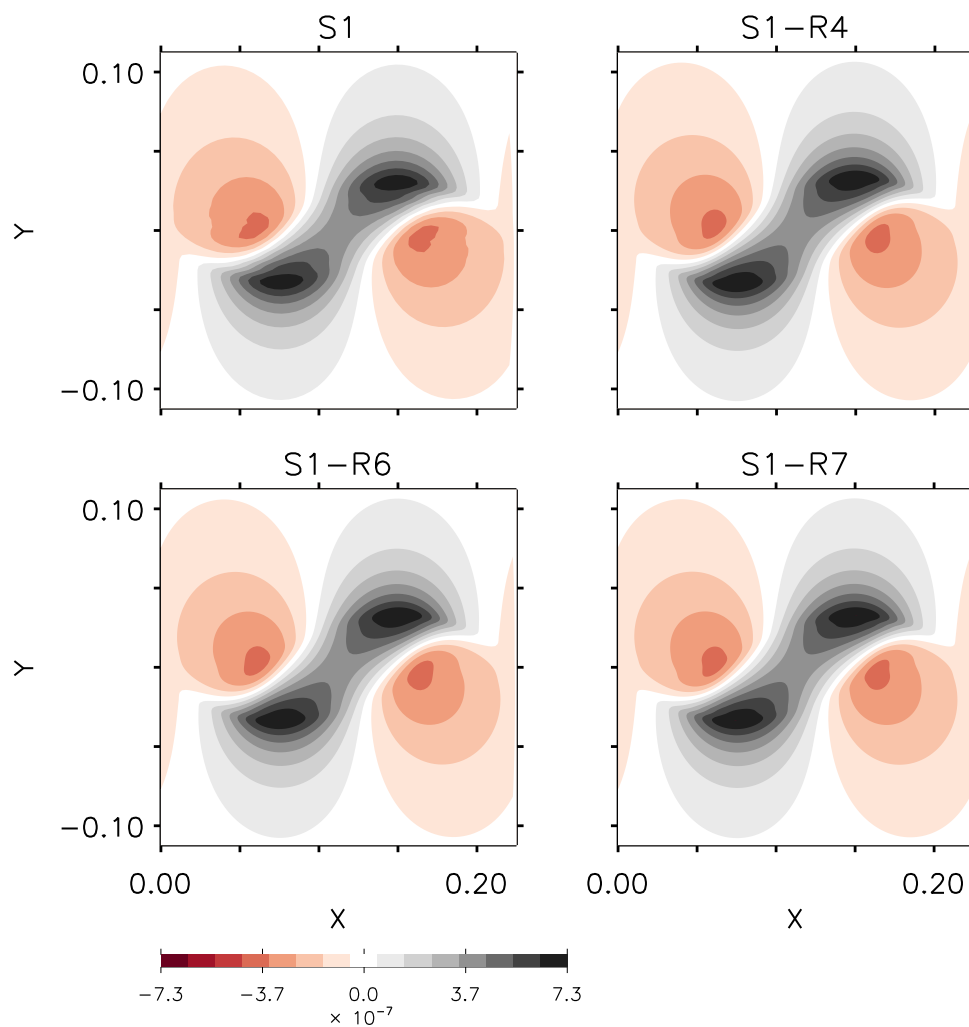
Figure 3.37: Plot comparing the divergence field δ for simulation S1, S1-R4, S1-R6, and S1-R7 at time $t = 10.125$.
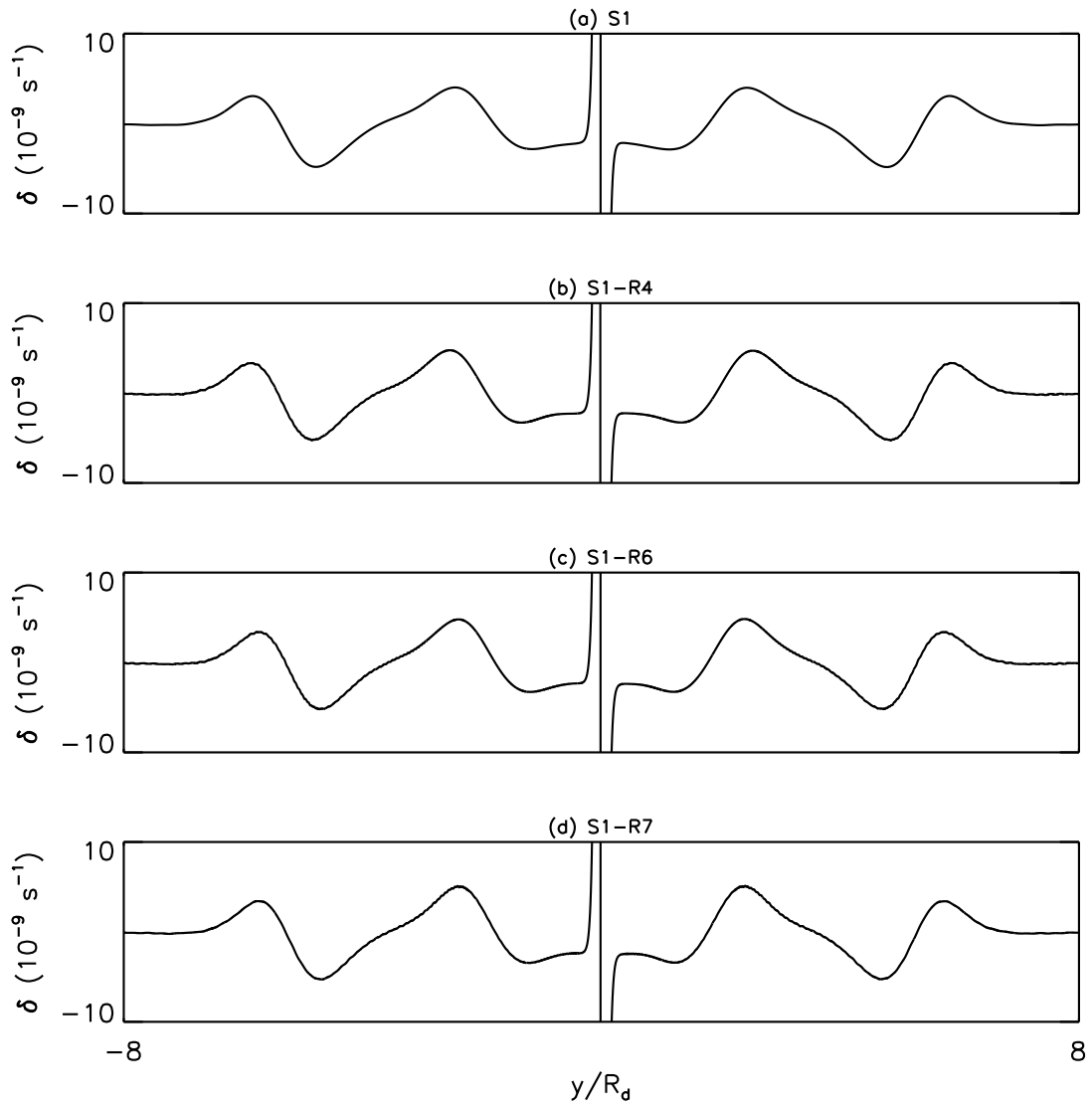
Figure 3.38: Plot comparing the meridional cross-section of simulated divergence field for simulation S1, S1-R4, S1-R6, and S1-R7 at time $t = 19.12$ along lines $x = .058R_d$.

Chapter 4

Comparison of simulated results with theory

4.1 Introduction

Ford (1994a) extended Lighthill's (1952) theory to rotating shallow-water flows. The gravity wave field predicted using the theory matched with the simulated gravity wave field. So it was concluded that the problem of wave emission in rotating flows can also be described within the framework of Lighthill's (1952) theory. Furthermore, his study showed that the effect of planetary vorticity severely inhibits shallow-water gravity wave emission from vortices with Rossby number of order one.

Ford explained the damping mechanism as follows: The effect of planetary vorticity ensures that gravity waves with frequency lower than the inertial frequency f are cannot propagate. Therefore, if more of the forcing spectrum shifts to frequencies below f, the effect of low-frequency cutoff is increased, thereby de-

creasing the amplitude of the emitted waves. This explanation was also supported by Sugimoto et al.'s (2008) study. They looked at the spectrum of the forcing terms in the Ford-Lighthill equation, and found that when a significant portion of the spectrum fell below the inertial frequency f, the wave amplitude decreased.

The equation governing the motion of a linear rotating shallow-water gravity wave is

$$\left(\partial_{tt}^2 + f^2 - c^2\nabla^2\right)\partial_t h = 0, \tag{4.1}$$

and the dispersion relation is

$$\omega^2 = f^2 + c^2k^2. \tag{4.2}$$

The effect of planetary vorticity f has rendered linear shallow-water gravity waves dispersive, and this effect has been introduced specifically by the presence of the term $f^2(\partial_t h)$ in (4.1). The dispersion relation also tells us that gravity waves with frequency lower than the inertial frequency f cannot propagate away from the source region. Therefore, Ford's (1994a) explanation of rotation inhibiting wave emission by means of low-frequency cut-off appears reasonable.

However, it is the aim of this chapter to show that Ford's (1994a) explanation of the inhibiting effect of rotation, and therefore, our understanding of the action of planetary vorticity on fluid motions is incomplete, because his explanation only considers the effect of the inertial cut-ff on wave emission. We will demonstrate that there are other rotational effects that directly inhibit gravity wave emission.

In chapter (2), we reviewed in detail the basis of Lighthill's (1952) formulation, and Ford's (1994a) extension to rotating shallow-water flows. We high-

lighted that Ford's formulation of the wave emission problem introduced a new term $f\epsilon_{3ki}\partial_k(\partial_j hu_i u_j)$, which was included in the wave forcing or non-homogeneous side of the wave equation. The significance of this term for the wave forcing mechanism is not clear and has not been investigated in the past. It is also our aim to gain insight into this term and its significance for the wave forcing mechanism. Specifically, since this term contains f as one of its factors, it clearly represents a direct effect of planetary vorticity f on the wave forcing terms. This chapter aims to seek answer to these question: What is the role of this term in the wave generation mechanism ?

The rest of the chapter is organised as follows: First we demonstrate the effectiveness of Ford-Lighthill equation in the description of the shallow-water gravity wave field in a rotating fluid: In subsection (4.2.1), the technique that is used to calculate the gravity wave field from the Ford-Lighthill non-homogeneous wave equation is reviewed. Lighthill's *compact source* approximation and its usefulness in evaluating the integral is discussed in subsection (4.2.2). The solution of the Ford-Lighthill equation is compared with the numerically simulated gravity wave field in subsection (4.2.3). The consequences of the *compact source* approximation for the description of the gravity wave field is then investigated. The inhibiting effect of the term $f\epsilon_{3jk}\partial_j(\partial_l hu_k u_l)$ is demonstrated in subsection (4.3.1). The effect of dispersion on wave characteristics is investigated in subsection (4.3.2). In subsection (4.3.3), the inhibiting mechanism represented by the term $f\epsilon_{3ki}\partial_k\partial_j(hu_i u_j)$ is investigated. Finally, we make some concluding remarks in section (4.4).

4.2 Solution of Ford-Lighthill equation (2.1)

4.2.1 Green's function solution

Since the simulation results showed that the emitted waves had relatively small zonal variations (i.e., x-dependent features) compared to the meridional variations, the non-homogeneous wave equation (2.1) is x-averaged before it is solved to assist comparison with simulated waves. The x-averaged equation (2.1) reads as

$$\left(\partial_{tt}^2 + f^2 - c^2\partial_{yy}^2\right)\partial_t\overline{h}^x = \partial_{yy}^2\overline{T_{22}}^x \tag{4.3}$$

where

$$\overline{T_{22}}^x = \partial_t\overline{(hv^2)}^x - f(\overline{huv}^x) + \frac{1}{2}g\partial_t\overline{(h-h_0)^2}^x \tag{4.4}$$

The Green's function $G[(y-y'), (t-t')]$ solution of (4.3) is

$$\overline{\frac{\partial h}{\partial t}}^x [y,t] = \int_{-\infty}^{\infty}\int_{t_0}^{t_r}\frac{\partial^2\overline{T_{22}}^x}{\partial y'^2}[y',t']G[(y-y'), (t-t')]dt'dy' \tag{4.5}$$

where $t_r = t - |y-y'|/c$, and variable y' indicates the position of the wave source, variable y indicates the position of the observer, t is the observation time, and t' indicates the time at which wave is emitted from the position y'. The Green's function $G[y,t]$ is obtained as a solution to the following non-homogeneous wave equation

$$\left(\frac{\partial^2}{\partial t^2} + f^2 - c^2\frac{\partial^2}{\partial y^2}\right)G = \delta[y]\delta[t] \tag{4.6}$$

122

where δ is the Dirac's delta function. The expression for $G[(y - y'), (t - t')]$ is (Ford, 1994a)

$$G[(y - y'), (t - t')] = \frac{1}{2c} J_0 \left[f \sqrt{(t - t')^2 - (y - y')^2/c^2} \right], \qquad (4.7)$$

where J_0 is the zero-order Bessel function. Then substituting for $G[y, t]$ in (4.5), we get

$$\overline{\frac{\partial h}{\partial t}}^x [y, t] = \frac{1}{2c} \int_{-\infty}^{\infty} \int_{t_0}^{t_r} \frac{\partial^2 \overline{T_{22}}^x}{\partial y'^2} [y', t'] J_0 \left[f \sqrt{(t - t')^2 - \frac{(y - y')^2}{c^2}} \right] dt' dy' \quad (4.8)$$

The integration of (4.8) can be performed in a straight forward manner provided the forcing function $\partial_{yy}^2 \overline{T_{22}}^x [y, t]$ is known. However, in the next section, we review Lighthill's (1952) *compact source* approximation, which is often used to reduce (4.8) into a form which is more suited to making an order of magnitude estimation of the emitted wave, and is also intended to provide some insight about the wave forcing terms.

4.2.2   Lighthill's compact source approximation

The first step in Lighthill's approach is to transform the spatial derivatives with respect to the source coordinate y' to the observation coordinate y. This can be done by making use of the identity,

$$\frac{\partial^2 T_{22}[y']}{\partial y'^2} G[y - y'] = \frac{\partial^2}{\partial y^2} \left(T_{22}[y'] G[y - y'] \right). \qquad (4.9)$$

Proof of this identity can be found in Crighton (1975) (see page 91, expressions (A-7) to (A-8)). Using this identity, (4.5) can be written as

$$\overline{\frac{\partial h}{\partial t}}^x [y, t] = \frac{1}{2c} \frac{d^2}{dy^2} \int_{-\infty}^{+\infty} \int_{t_0}^{t_r} T_{22}[y', t'] G[(y - y'), (t - t')] dt' dy' \qquad (4.10)$$

Substituting for $G[(y - y'), (t - t')]$ in the last expression, we get

$$\overline{\frac{\partial h}{\partial t}}^x [y, t] = \frac{1}{2c} \frac{d^2}{dy^2} \int_{-\infty}^{+\infty} \int_{t_0}^{t_r} T_{22}[y', t'] J_0 \left[f \sqrt{(t - t')^2 - (y - y')^2/c^2} \right] dt' dy' (4.11)$$

Both (4.8) and (4.11) give identical results, but the advantage (4.11) has over (4.8) is that it provides a better order of magnitude estimate, when the *compact source*[1] approximation is made.

For instance, if the compact source approximation is made in (4.8), then J_0 in (4.8) can be approximated as

$$J_0 \left[f \sqrt{(t - t')^2 - y^2/c^2} \right].$$

Using this approximation, (4.8) becomes

$$\overline{\frac{\partial h}{\partial t}}^x [y, t] = \frac{1}{2c} \int_{t_0}^{t - |y|/c} \left(\int_{-\infty}^{\infty} \frac{\partial^2 \overline{T_{22}}}{\partial y'^2} [y', t'] dy' \right) J_0 \left[f \sqrt{(t - t')^2 - y^2/c^2} \right] dt'. (4.12)$$

Now if the *divergence theorem* is applied to the integral

$$\int_{-\infty}^{\infty} \frac{\partial^2}{\partial y'^2} T_{22}[y', t'] dy', \qquad (4.13)$$

we get a null result, because T_{22} is extended over finite region in space.

---

[1] A source is said to be *spatially compact* if the phase difference between two interfering waves from two different points in the source region can be neglected. This assumption is particularly true when the period of waves are large compared to the phase difference arising due to spatial distribution of these two points.

On the other hand, (4.10) does not suffer from this error. After making the compact source approximation (4.10) becomes

$$
\overline{\frac{\partial h}{\partial t}}^x [y, t] = \frac{1}{2c} \frac{d^2}{dy^2} \int_{-\infty}^{+\infty} \int_{t_0}^{t-|y|/c} T_{22}[y', t'] dy' J_0 \left[f \sqrt{(t - t')^2 - \frac{y^2}{c^2}} \right] dt' \quad (4.14)
$$

The last expression can be written as

$$
\overline{\frac{\partial h}{\partial t}}^x [y, t] = \frac{1}{2c} \frac{d^2}{dy^2} \int_{t_0}^{t-|y|/c_0} S[t'] J_0 \left[f \sqrt{(t - t')^2 - y^2/c^2} \right] dt' \quad (4.15)
$$

where

$$
\begin{aligned}
S[t'] &= \int_{-\infty}^{\infty} \overline{T_{22}}^x [y'] dy' \\
&= \int_{-\infty}^{\infty} \overline{\frac{\partial (hv^2)}{\partial t}}^x dy' - \int_{-\infty}^{\infty} f(\overline{huv}^x) dy' + \int_{-\infty}^{\infty} \frac{1}{2} g \overline{\frac{\partial (h - h_r)^2}{\partial t}}^x dy' \\
&= S_A[t'] + S_B[t'] + S_C[t'] \quad (4.16)
\end{aligned}
$$

4.2.3 Comparison of the gravity wave field with the simulated wave

Both expressions (4.8) and (4.15) can be used to evaluate the gravity wave field, provided S is known. And in order to evaluate $S[t]$, the values of field variables u, v and h, which vary with both space and time, have to be known. Since the Lighthill-Ford formulation does not predict the evolution of these field variables in the wave forcing region, these values have to be supplied externally. For example, in the earlier studies (e.g., Ford 1994a; Sugimoto et al. 2008), these value were obtained from the numerical solution of the fully nonlinear shallow-water equations. Here too we obtain these values based on the numerical solution of the nonlinear shallow-water equations.

Figure (4.1) compares the simulated wave with solution (4.15) of the Ford-Lighthill equation. It can be observed that the solution (4.15) slightly underestimates the simulated wave at the crests and troughs. Figure (4.2) shows the same wave as fig. (4.1) in the near-field. Therefore, our results, in common with Ford (1994a) and Sugimoto et al. (2008), show that solution (4.15) of the Ford-Lighthill equation provides a very good description of the far-field gravity wave field. In addition, however, our result also show that solution (4.15) is a bad approximation to the simulated near-field. Next we show that these errors are a consequence of making the *compact source* approximation in evaluating the integral (4.8). Solution (4.15) was derived by making Lighthill's *compact source* approximation in (4.8).

Figure (4.3) compares the simulated wave with the exact solution (4.8), and figure (4.4) shows the same wave in the near-field. We now observe that the agreement between the simulated wave and the solution (4.8) is very good in both the near and far-field, and the errors that were visible in fig. (4.1) and (4.2) have now disappeared. This is because (4.8) does not make the compact source approximation.

4.3 Discussion

4.3.1 The nature of the term $f\epsilon_{3ki}\partial_k(\partial_j hu_iu_j)$

Expression (4.16) shows that the wave forcing term S comprises of three terms: S_A $(=\int_{-\infty}^{\infty} \partial_t \overline{(hv^2)}^x dy')$, S_B $(= -\int_{-\infty}^{\infty} f(\overline{huv}^x)dy')$, and S_C $(=\int_{-\infty}^{\infty} \frac{1}{2}g\partial_t \overline{(h-h_r)^2}^x dy')$. In order to investigate the contribution of the term $f\epsilon_{3ki}\partial_k(\partial_j hu_iu_j)$ to wave forcing, we compare the individual contribution of these terms to the forced gravity
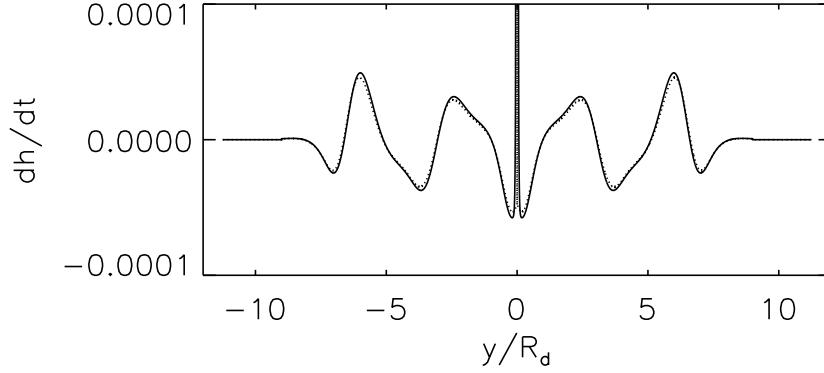
Figure 4.1: Figure compares the simulated gravity wave (solid line) with that predicted by (4.15) (dotted line). The result is based on simulation $S1$.

wave field.

Fig. (4.5) (a) shows the contribution of these individual terms to (4.15). The forcing due to S_A alone (indicated by dashed line) dominates, followed by S_B (dot-dashed line). Term S_C (long-dashed line) appears to have negligible contribution; it is smaller by a factor of almost 10^{-2} compared to the other two term (see fig. (4.5) (b), which shows the wave forcing due to term S_C)

Notice that the forcing due to S_A alone overestimates the simulated wave amplitude (indicated by solid line). It is the cumulative effect of S_A and S_B which provides a better approximation to the simulated wave. Furthermore, fig. (4.5) (a) also shows that the term S_B contributes by counter acting the effect due to the dominant term S_A.

Therefore, our study shows that term $f\epsilon_{3ki}\partial_k(\partial_j h u_i u_j)$ acts as a direct inhibiting term, and that this effect is significant, because its exclusion can introduce significant errors in the predicted gravity wave field.

The investigation of the inhibiting mechanism due to $f\epsilon_{3ki}\partial_k(\partial_j h u_i u_j)$ will
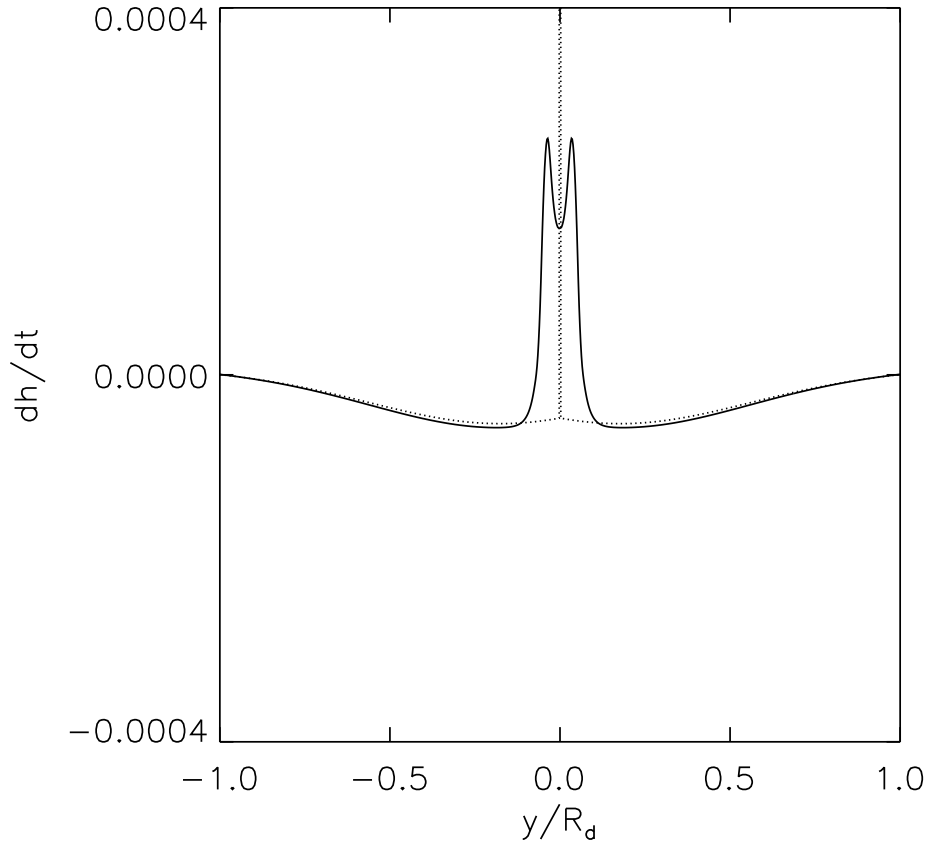
Figure 4.2: Same as fig. (4.1), but showing the near-field. The maximum value of dh/dt predicted from solution of Ford-Lighthill equation is of the order of 10^{-2}.

be continued in subsection (4.3.3). But first, in the next subsection, we investigate the effect of dispersion on wave emission, so that it can be compared to the direct inhibiting effect produced by the $f\epsilon_{3ki}\partial_k(\partial_j h u_i u_j)$ term.

4.3.2   Effect of dispersion on wave emission

In order to estimate the contribution of dispersion to damping, we will calculate the wave forcing due to the term $\partial^2_{yy}\overline{T_{22}}^x$ in the Ford-Lighthill wave equation (2.1), but with the effect of dispersion switched off. That is, we seek solution to the wave

128
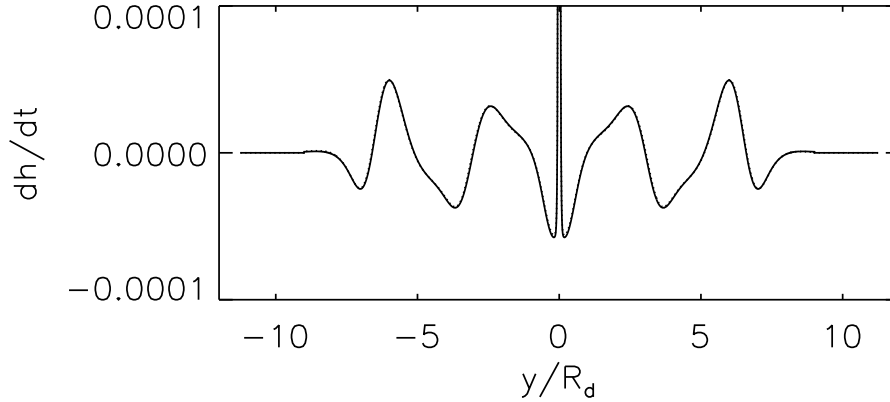
Figure 4.3: Same as fig. (4.1), but showing the Green's function solution (4.8).

equation

$$\left(\partial_{tt}^2 - c^2\partial_{yy}^2\right)\partial_t\overline{h}^x = \partial_{yy}^2\overline{T_{22}}^x \tag{4.17}$$

where

$$\overline{T_{22}}^x = \partial_t(\overline{hv^2}) - f(\overline{huv}^x) + \frac{1}{2}g\partial_t\overline{(h-h_0)^2} \tag{4.18}$$

The Green's function solution of (4.17) is

$$\frac{\overline{\partial h}^x}{\partial t}[y,t] = \int_{-\infty}^{\infty}\int_{t_0}^{t_r}\frac{\partial^2\overline{T_{22}}^x}{\partial y'^2}[y',t']G[(y-y'),(t-t')]dt'dy' \tag{4.19}$$

where $t_r = (t-|y-y'|/c)$, and the Green's function $G[(y-y'),(t-t')]$ now takes the form (see e.g., Morse and Feshback, 1953)

$$G[(y-y'),(t-t')] = \frac{1}{2c}H\left[c^2(t-t')^2 - (y-y')^2\right], \tag{4.20}$$

129
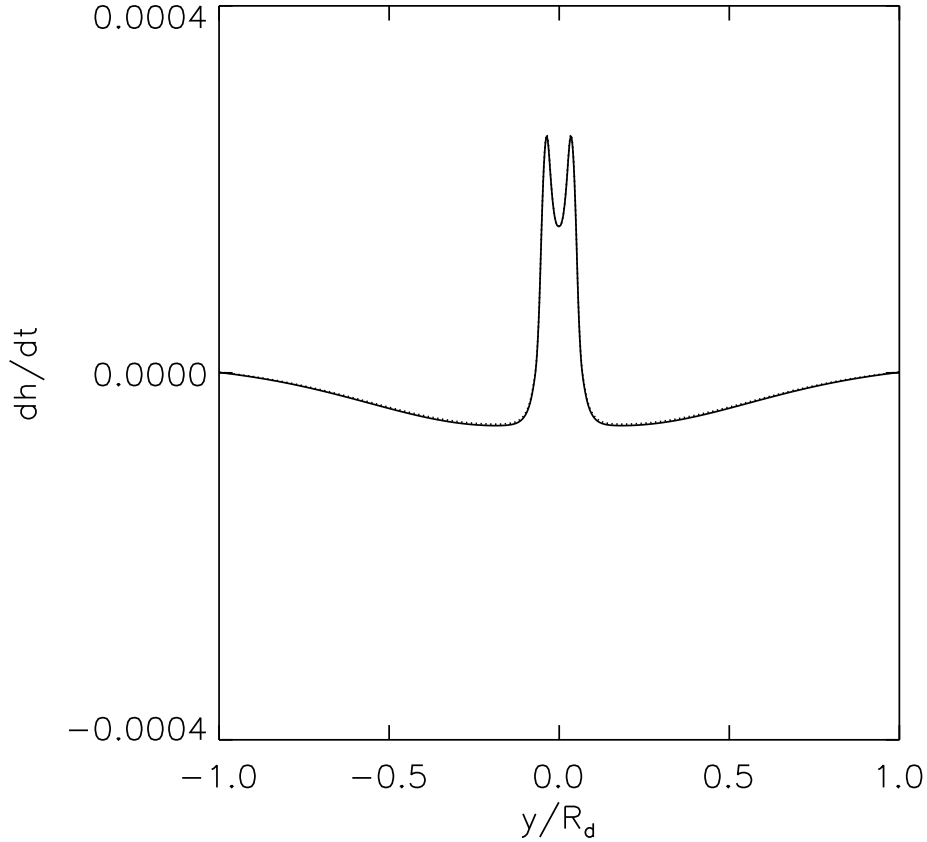
Figure 4.4: Same as fig. (4.3), but showing the near-field Green's function solution
(4.8).

where H is the *Heaviside* function. Then, as in section (4.2.2), after making the
Lighthill's *compact source* approximation, expression (4.19) reduces to

$$\overline{\frac{\partial h}{\partial t}}^x [y, t] \;\; = \;\; \frac{1}{2c}\frac{\partial^2}{\partial y^2}\int_{t_0}^{t_r} S[t']H[c^2(t-t')-y^2]dt' \qquad (4.21)$$

where $S[t'] = \int_{+\infty}^{-\infty} \overline{T_{22}}^x(y', t')dy'$. In the discussions to follow, we will refer to this
solution as the *non-dispersive* wave. The Lighthill's *compact source* approximation
has been made to reduce the computation time.

Figure (4.6) compares the solution (4.21) with the x-averaged simulated
wave, which we shall refer to as the *dispersive* wave, at various times during the

130

propagation. Figure clearly shows the effect of dispersion on the propagating wave, and this effect becomes more evident as time progresses. Initially, the phase and amplitude difference between the dispersive and the non-dispersive counterpart is small, but as time progresses, differences become evident. The distortion of the wave-packet due to dispersion occurs because the longer wave components of the wave packet propagate at a faster speed compared to the shorter wave components and their non-dispersive counterparts. The shorter components can be seen making up the leading edge of the dispersive wave packet. The difference between the amplitudes of the dispersive and non-dispersive packets is relatively minor and can be explained on the basis of constructive/destructive interference in the dispersive wave packet. The dominant wave number is $kR_d \approx 0.54$, yielding $\omega \approx 1.14f$.

4.3.3 Investigation of inhibiting effect represented by the term $f\epsilon_{3ki}\partial_k(\partial_j h u_i u_j)$

In order to study the dependence of the term $f\epsilon_{3ki}\partial_k(\partial_j h u_i u_j)$ on the time-scale of evolution in the wave forcing region, we conduct two more simulations: S2 and S3. Our aim is to see how the contribution of the term $f\epsilon_{3ki}\partial_k(\partial_j h u_i u_j)$ varies with the 1) time-scale and 2) amplitude of the wave forcing terms. The details of simulations S1 to S3 are provided in Table (4.1).

Simulation S2 is conducted with the purpose of increasing the time-scale, while keeping the scale of the vortex close to simulation S1. This is achieved by decreasing the amplitude of the PV-anomaly by 40%, but keeping the width of the anomaly of the basic state same as in simulation S1. This reduces both Ro and F to 60% of their S1 values.

Initialization parameters		Simulation		
		S1	S2	S3
Height of fluid at rest	h_r	3 km	3 km	3 km
Reduced gravity	g'	0.3	0.3 m s^{-2}	0.3 m s^{-2}
Coriolis parameter	f	10^{-4} s^{-1}	10^{-4} s^{-1}	10^{-4} s^{-1}
Gravity wave phase speed	$c \; (=\sqrt{gh_r})$	30 m s^{-1}	30 m s^{-1}	30 m s^{-1}
Rossby radius	$R_d \; (= c/f)$	300 km	300 km	300 km
Half-width of PV-anomaly	y_0	$.014625R_d$	$.014625R_d$	$.075375R_d$
Amplitude of PV-anomaly	A	5	3	5
Rossby number	Ro	4.568	2.817	3.402
Froude number	F	.066681	.0412	0.2564
Wave number of fastest growing mode	k_x	$27.94/R_d$	$27.99/R_d$	$5.4357/R_d$

Table 4.1: Table lists the initialization parameter values used in simulations S1, S2, and S3.

In simulation S3, we consider the effect of increasing both the timescale and scale of the vortex. This is achieved by increasing the width of the anomaly, but keeping the amplitude of the anomaly the same as in simulation S1. This reduces Ro but increases F by almost a factor of 4.

Figure (4.7) compares the evolution of the forcing function $S[t]$ for simulations S1, S2, and S3. Figure (4.7) (b) shows the consequence of decreasing the amplitude of the PV-anomaly by 40%. The amplitude of the forcing terms has reduced by almost a factor of 100, and the time-scale of fluctuation has increased compared to simulation S1. The decrease in vortex amplitude and background shear would alone be expected to produce a modest (e.g., $\sim 40\%$) reduction in the forcing terms. It is clear that the increase in vortex timescale is primarily responsible for the drastic reduction in the efficiency of wave forcing.

Numerical discretization parameters		Simulations		
		S1	S2	S3
Meridional grid spacing	Δy	$0.00225R_d$	$0.00225R_d$	$0.00225R_d$
Zonal grid spacing	Δx	$2\Delta y$	$2\Delta y$	Δy
Total grid points in x-direction	M	51	51	515
Total grid points in y-direction	N	10001	10001	10001
Zonal domain length	L_x	$0.225R_d$	$0.225R_d$	$1.1655R_d$
Meridional domain length	$2L_y$	$22.5R_d$	$22.5R_d$	$22.5R_d$
Time step	Δt	5.625 s	5.625 s	5.625 s
Robert-Asselin filter	α	.02	.02	.02
Width of damping layer	D	$2.25R_d$	$2.25R_d$	$2.25R_d$
Courant number	C_n	0.25	0.25	0.25
Zonal dissipation parameter	γ_x	0.25×10^{-4}	0.25×10^{-4}	1.0×10^{-4}
Meridional dissipation parameter	γ_y	0	0	0

Table 4.2: Table lists the spatial and temporal discretization, and dissipation parameters values used in simulation S1, S2, and S3. The Courant number $C_n = c(\Delta t/\Delta y)$ and $c = \sqrt{gh_r}$ is the non-rotating gravity wave phase speed at rest. $\gamma_x = \nu_x/\Delta x^6$, and $\gamma_y = \nu_y/\Delta y^6$, where ν_x and ν_y are the diffusivity along x and y-direction, respectively.

Figure (4.7) (c) shows the effect of increasing the width of the anomaly by a factor of about 5. The amplitude of the forcing terms has increased compared to simulations S1 and S2, and the time-scale has significantly increased when compared with simulation S1, but only slightly when compared to S2. In this case the stronger shear has more than compensated for the reduced efficiency in wave forcing associated with the longer timescale.

Now, in order to measure how the damping effect varies with time-scale of evolution of the forcing terms, we define a ratio r_d as

$$r_d = \frac{|S_B|}{|S_A + S_C|}, \tag{4.22}$$

133

	t_a	t_b	t_c
S1	27.1%	26.3%	24.7%
S2	46.3%	44.4%	41.9%
S3	49.9%	45.4%	46.6%

Table 4.3: The above matrix list the value of r_d. Rows correspond values of r_d for simulations: S1, S2, S3, and columns corresponds to values of r_d at times: t_a, t_b and t_c. The values of r_d have been calculated at times when the amplitude of the forcing S_A reached its first maxima (i.e., time $= t_a$), first minima (time $= t_b$), and second maxima (time $= t_c$) in fig. (4.7). The values of t_a, t_b and t_c have been provided in the caption of fig. (4.7).

which gives an estimate of the damping relative to the amplitude of the forcing terms. The values of r_d for simulations S1, S2, and S3, have been listed in Table (4.3). The increase in value of r_d as we move from simulations S1 to S3, therefore indicates that the damping due to term $f\epsilon_{3ki}\partial_k\partial_j hu_iu_j$ increases with time-scale of the wave forcing terms.

Figure (4.8) compares the gravity wave field in simulations S1, S2, and S3. The results are consistent with the strengths of the wave forcing terms shown in fig. (4.7).

The above results thus indicate that the term $f\epsilon_{3ki}\partial_k\partial_j hu_iu_j$ opposes the dominant forcing $\partial_{ij}^2\partial_t(hu_iu_j)$ and therefore the rotation of the Earth provides a inhibiting effect on wave emission for the flow parameters considered here.

4.4 Summary and concluding remarks

In this chapter, the technique used to solve the Ford-Lighthill equation (2.1) was reviewed. The solution of the Ford-Lighthill equation was then compared with the simulated shallow-water gravity wave field. In common with Ford (1994a) and

Sugimoto et al. (2008), our study also demonstrated that Lighthill-like formulation can be very effective at describing the far-field gravity wave. Furthermore, our study highlighted the error that arises in the description of the gravity wave field as a consequence of making the Lighthill's *compact source* approximation. Specifically, it was shown that huge errors arise in the description of the near-field wave when the *compact source* approximation is made.

The significance of this term $f\epsilon_{3ki}\partial_k\partial_j hu_i u_j$ to the wave generation mechanism, which arose as a consequence of Ford's (1994a) extension of Lighthill's (1952) theory was investigated. Results showed that excluding this term introduced significant error in the amplitude of the predicted gravity wave field. Results also showed that this term contributes by opposing the dominant nonlinear forcing. Therefore, it was concluded that this term is important in the formulation of the wave generation problem.

It was also demonstrated that in the case of simulation S1, the effect of dispersion produces significant distortion as the wave continues to propagate.

Lastly, the study focused on investigating the inhibiting mechanism represented by the term $f\epsilon_{3ki}\partial_k\partial_j(hu_i u_j)$. For this purpose, two more simulations were conducted. In the first case, the effect of decreasing the Rossby number compared to simulation S1 was considered. In the second case, the effect of increasing the Froude number was considered. These simulations showed that the damping represented by the $f\epsilon_{3ki}\partial_k\partial_j(hu_i u_j)$ increases with the time-scale of the evolution of the the wave forcing terms.

In conclusion, our study suggests that both the term: $f\epsilon_{3ki}\partial_k\partial_j(hu_i u_j)$ and $f^2(\partial_t h)$, contribute to the effect of rotation of Earth on fluid motions. The latter contributes to dispersion only, while the former represents a direct inhibiting effect of rotation of the Earth's rotation on fluid motions and wave forcing.

135
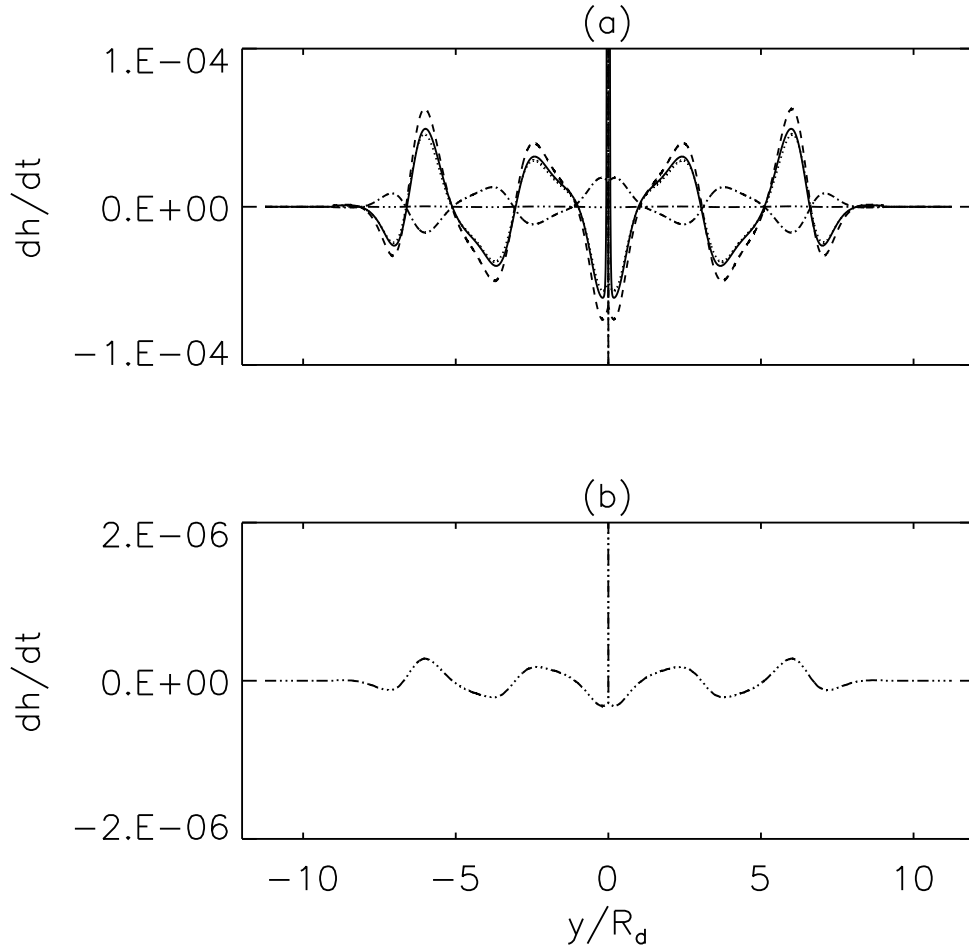
Figure 4.5: (**a**) Figure showing the contribution to (4.15) due to terms S_A, S_B, and S_C in expression (4.16). Solid line represents the simulated field. Dotted line represents the response due to total forcing S, i.e, the solution (4.15). Dashed line represents the response due to forcing S_A alone. Dot-dashed line is the response due to forcing S_B alone, and dot-dot-dot-dash is the response due to S_C alone. Results are from simulation $S1$; (**b**) Same as in frame (**a**), but highlights the contribution due to term S_C, which appeared to have negligible contribution in (**a**). The y-axis range has been reduced by a factor of 10^2 in comparison to the y-axis range in (a).
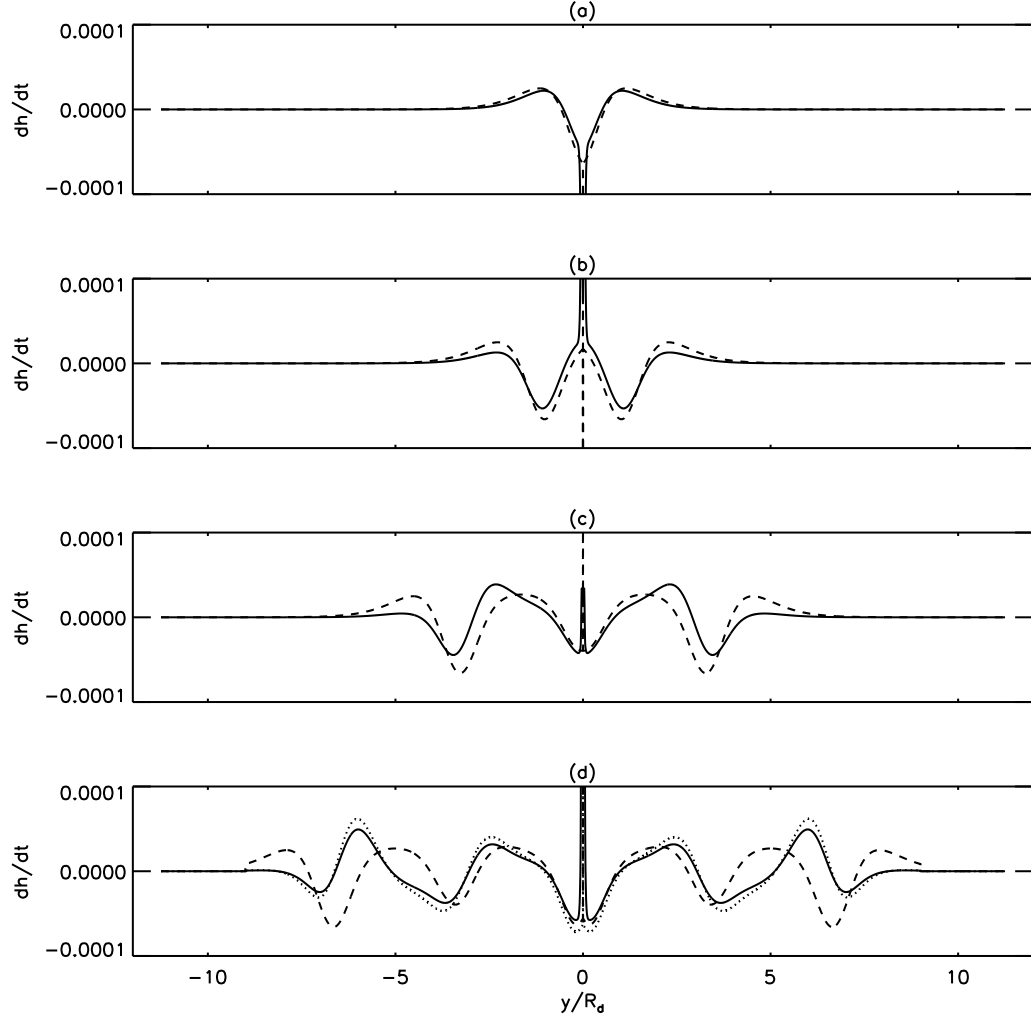
Figure 4.6: Figure illustrates the effect of dispersion on the propagating waves. Frames (a)-(d) show evolution with time. Solid line is the simulated (dispersive) gravity wave , and dashed line shows the propagation of the non-dispersive counterpart, indicated by (4.21). Also shown in frame (d), for purposes of comparison, is the solution (4.15) with the damping term $f\epsilon_{3ki}\partial_k(\partial_j h u_i u_j)$ excluded from the forcing function (dotted-line).
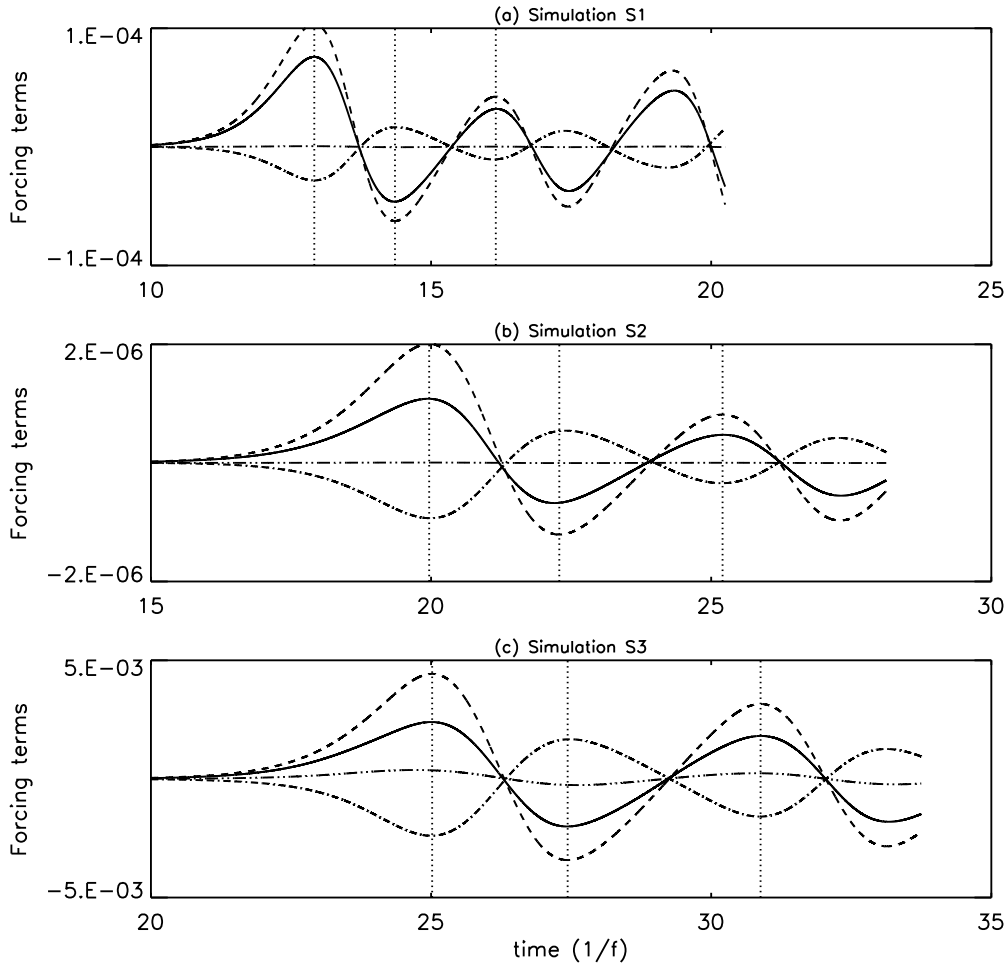
Figure 4.7: Figures compare the temporal variation of the forcing function S[t] $(= \int_{-\infty}^{+\infty} \overline{T_{22}}^x dy)$ for simulations: S1, S2 and S3. Solid line indicates S $(= S_A + S_B + S_C)$, dashed line indicated S_A, dot-dashed line shows S_B, and dot-dot-dashed line shows S_C. Dotted lines indicate the location of the maxima and minima. **(a)** $t_a = 12.9$, $t_b = 14.3$, $t_c = 16.1$. **(b)** $t_a = 19.9$, $t_b = 22.2$, $t_c = 25.2$. **(c)** $t_a = 25.0$, $t_b = 27.43$, $t_c = 30.8$.

138
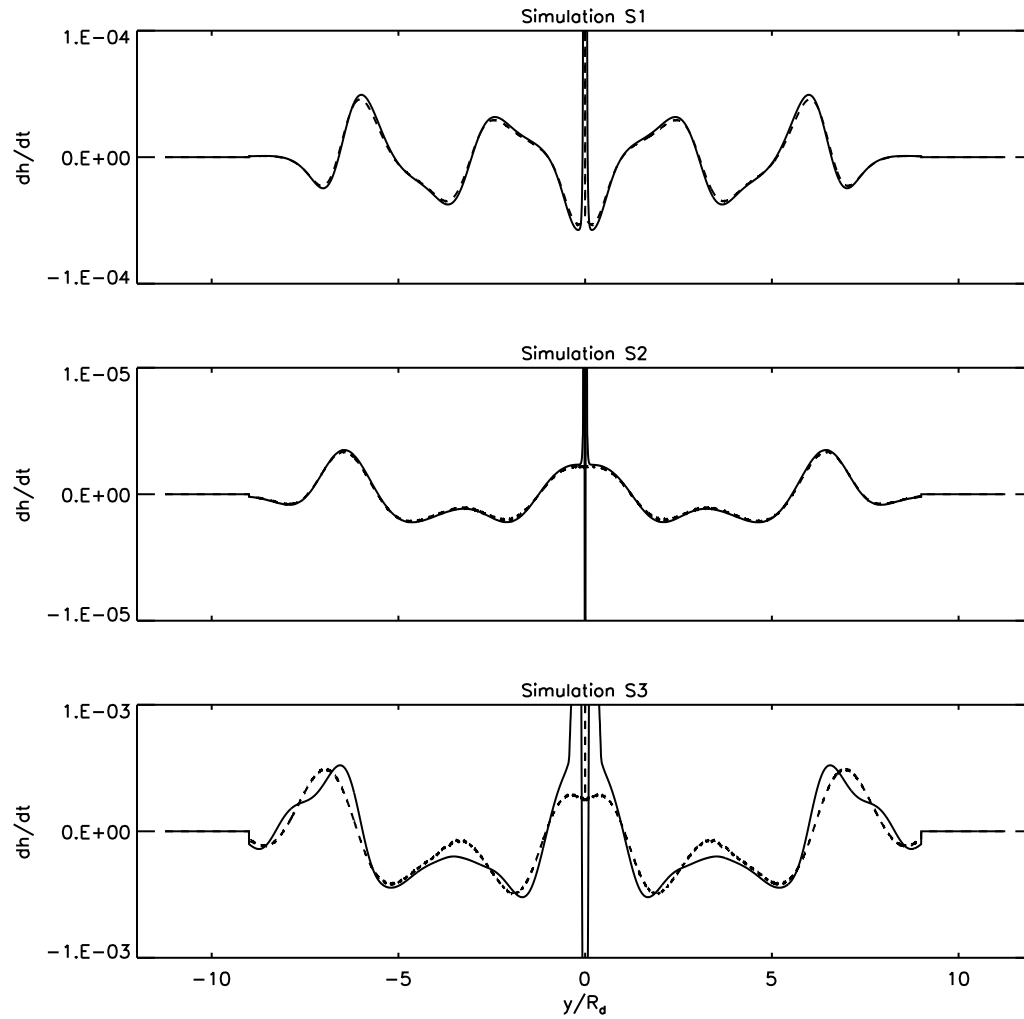
Figure 4.8: Figures compare the gravity wave field for simulations: S1, S2 and S3. Solid line indicates simulated field, and dashed line indicates the solution based on the Ford-Lighthill equation.

Chapter 5

Wave emission due to vortex merging

5.1 Introduction

In chapter 3, shallow-water gravity wave emission associated with the evolution of a single vortex was investigated. In this chapter, we study the process of merging of vortices and the gravity wave emission associated with this process in the context of a rotating (constant f-plane) shallow-water model. It is known (e.g., Klaassen and Peltier 1989) that the merging results in increase of the size and amplitude of vortices. On that basis one might expect stronger wave emission. The mechanism associated with the merging of vortices and how this affects the process of gravity wave generation will be investigated.

Initialization parameters	Simulation
	VM
Height of fluid at rest h_r	3 km
Reduced gravity g'	0.3 m s^{-2}
Coriolis parameter f	10^{-4} s^{-1}
Gravity wave phase speed $c\ (=\sqrt{gh_r})$	30 m s^{-1}
Rossby radius $R_d\ (=c/f)$	300 km
Half-width of PV-anomaly y_0	.014625R_d
Amplitude of PV-anomaly A	5
Rossby number Ro	4.568
Froude number F	.06681
Wave number of fastest growing mode k_x	27.94/R_d

Table 5.1: Table lists the initialization parameter values used in simulation VM.

5.2   Simulation details

The basic state used to simulate merging of vortices is the same as that used in simulation $S1$: It comprises a thin region of PV-anomaly embedded over an extensive region of uniform background potential vorticity. In order to allow vortex merging, the stream-wise model domain length is doubled.

Table (5.1) lists the model initialization parameters used to simulate merging of shallow-water vortices, and Table (5.2) lists the numerical discretization parameters used. Since the zonal domain length used is double of that used in simulation S1, the instability generates a pair of vortices which can subsequently undergo merging.

The simulation is initiated by disturbing the zonal basic state flow with small amplitude sinusoidal disturbance in height field with wavelength equal to

Numerical discretization parameters	Simulation
	VM
Δy	$.00225 R_d$
Δx	Δy
M	201
N	10001
Δt	2 s
α	.02
N_d	1000
$c\ (\Delta t/\Delta y)$	0.08
γ_x	0.25×10^{-4}
γ_y	0.25×10^{-4}

Table 5.2: Table lists the numerical discretization parameter values used in simulations VM.

the fastest growing mode, as in simulation S1 (hereafter, this disturbance will be referred to as the primary disturbance). The basic state is also disturbed with a secondary disturbance with the wavelength equal to double that of the primary disturbance. The primary disturbance assures that a pair of vortices are formed, and the secondary disturbance, which grows at a much slower rate compared to the primary disturbance, assists with the merging of the vortices, by displacing the primary vortices in opposite cross-stream directions (the cross-stream direction y is orthogonal to the streamwise direction x).

5.3   Results and discussion

As in simulation S1, the initial phase of the simulation is dominated by the evolution of the primary disturbance, the details of which were discussed in Chapter 3. Therefore, in this chapter, our discussions will focus mainly on the evolution of the secondary disturbance, and how its evolution results in merging of the primary vortices.

Fig. (5.1), illustrates the process of merging when viewed in the potential vorticity field. Frame (a) shows an instant when the primary disturbance has already rolled-up into a pair of vortices, and the amplitude of the secondary disturbance has grown sufficiently large that it has started to disturb the location of the primary vortices, the left upward and right downward. Frame (b) shows that the vortices have been further displaced. The subsequent frames show the the two vortices begin to orbit each other as they merge.

Fig. (5.2) shows the height or pressure fluctuations associated with the merging of the vortices. Clearly seen are the two separate low pressure centers associated with the vortex pair before the merging takes place. As the secondary disturbance begins to grow, the vortex on the right in frame (b) is advected towards the North (positive y-direction) and the one on the left is advected towards the South (negative y-direction), i.e., the two vortices begin a cyclonic orbit. Frames (b-c) show that the low-pressure centers have started to merge into single low-pressure center. Therefore, the merging of vortices must be also be accompanied by expulsion of the mass between the low-pressure centers, therefore increasing the depth and area of the low-pressure region.

The wind field pattern also indicates that the initially separate cyclonic circulations have merged into a single large cyclonic circulation. Once the low-pressure centers have merged the cyclonic circulation continues to evolve, i.e., it continues to rotate in an anti-clockwise fashion. After the vortices have merged, the dynamics is similar to the evolution of a single vortex, which was considered in detail as in Chapter 3. The only significant difference being the size of the vortex, which now has a scale that is almost doubled. How this increase in size has an effect on the process of gravity wave emission in rotating fluid will be discussed later.

Further insight into the process of merging can be obtained by analyzing the perturbation height field (h'). Figure (5.3) shows the evolution of h' associated with the merging of the vortices. Clearly visible in frame (a) are the high-pressure centers which were masked by the mean zonal pressure field in fig. (5.2). Two high-pressure centers can be identified in frame (a): One in between the low-pressure centers, and one-half on the right or East and other one-half on the left or West of the central high-pressure center.

The direction of the perturbation wind $\mathbf{v}'$ pattern indicates that the vortex pair is in the middle of the intensification phase. Frames (a) and (b) show that the perturbation wind is spiraling out of the low-pressure centers and feeding into the high-pressure region on the sides, although not towards the central high-pressure center. This indicates that the low-pressure centers are losing mass, and the high pressure regions on the sides are gaining mass. In contrast, we observe that the central high pressure region is also losing mass (see frames (a) and (b)). Frames (a) and (b) also shows that the anti-cyclonic circulation over the high pressure region is weakening. This effect must be a consequence of the presence of the secondary long wave disturbance, as it is a new effect which was not observed in the single vortex case.

Since the perturbation wind field ($\mathbf{v}'$) shown in figure (5.3)) comprises both the vortical and divergent wind component, then, as in the case with single vortex, the fluctuation in the perturbation height (h') must arise as a consequence of both the vortical and divergent fluid motions. Figs. (5.4) and (5.5) show that the evolution of the h'-field with the wind fields $\mathbf{v}'_\psi$ and $\mathbf{v}'_\chi$ overlaid on it, respectively, where

$$\mathbf{v}' = \mathbf{v}'_\psi + \mathbf{v}'_\chi, \tag{5.1}$$

$\mathbf{v}'_\psi = (\hat{\mathbf{k}} \times \nabla\psi)$ and $\mathbf{v}'_\chi = \nabla\chi$, ψ is a stream function for the rotational part of $\mathbf{v}'$ and χ is a velocity potential for the divergent part of $\mathbf{v}'$, so that $\nabla^2\psi$ and $\nabla^2\chi$ are vorticity (ζ) and divergence (δ).

Again, as in the single vortex case, it is evident from figs. (5.4) and (5.5) that the wind fields $\mathbf{v}'$ and $\mathbf{v}'_\psi$ are almost identical, because $|\mathbf{v}'_\chi|$ is smaller by a factor of almost 10^3 compared to $|\mathbf{v}'_\psi|$, indicating that almost all of the adjustment in the mass needed for the low-pressure centers to merge is produced by rotational wind, while the divergent wind $\mathbf{v}'_\chi$ aids in further minor adjustment of the mass field. Again, we observe that the centers of low and high pressure regions do not coincide with location of *sources* and *sinks*. These *sources* and *sinks* are easier to identify in divergence field plots.

Fig. (5.6) shows the evolution of the divergence (δ) field. The divergence field in frame (a) is very similar to the one observed in the case of simulation S1 (see frame (b) of fig. (3.10)). Clearly visible are the pair of *quadrupole* sources in frame (a). As the vortices begin to merge, the pair of *quadrupole* sources begin to merge too into a single *quadrupole* source. Frame (d) clearly shows that the merging of the sources is complete, as only a single *quadrupole* source is visible. But the intermediate stage, as seen in frame (c), shows that this merging takes place by formation of a combination of source and sinks which does not resemble a *quadrupole*. Thereafter the divergence field resembles that of a single evolving vortex. We again observe that frame (c), which shows the weakest divergence field, is associated the most *axisymmetric* wind field.

Fig. (5.7) shows the divergence in the intermediate field. Figs. (5.8) and (5.9) show the contribution of $\partial v/\partial y$ and $\partial u/\partial x$,respectively, in the intermediate region. Just as in the single vortex case, here too we observe that both the $\partial u/\partial x$ and $\partial v/\partial y$-fields show strong zonal variations, and $\partial v/\partial y$ dominates in

the intermediate region. In contrast to the single vortex case, we observe that both the fields are stronger in intensity. Some effect of vortex merging can be observed in the intermediate fields. We observe that the near-field high intensity region extends deeper into the meridional direction, though not beyond the Rossby radius (see the transition from frames (a) to (d)).

Figs. (5.10) and (5.11) show the corresponding fields in the far-field region. Interestingly, we observe that the mass transport does not extend beyond the Rossby radius, indicating that Rossby radius puts a strong constraint on the distance to which the mass gets transported by the divergent wind. Just as in the single vortex case, clearly visible are propagating shallow-water gravity waves, which are comprised entirely of $\partial v/\partial y$-field. Also can be recognized is the lack of zonal variation, outside the intermediate region.

Fig. (5.12), shows the gravity waves propagating further in the meridional direction. Fig. (5.13) shows a meridional cross-section of the wave in fig. (5.12). We observe that no significant change in the amplitude of shallow-water gravity waves has occurred following the merging of the vortices when compared to the wave amplitude observed in simulation S1. Even though we observe that merged vortex is bigger and stronger compared to the vortex in S1 case, surprisingly there isn't much difference in the emitted gravity wave.

In order to understand why this has occurred, we compare the magnitude of the near-field divergence δ in the single vortex case and after the merging of vortices (compare the value of δ in figs. (3.10) and (5.6)). Results show the maximum amplitude of δ during and after merging has barely changed compared to the single vortex case; the amplitudes are still of the same order of magnitude.

In order to gain more insight into this problem, we look at the temporal evolution of components of Lighthill's forcing terms S_A, S_B, and S_C (see expression

146

(4.16) for definition of S_A, S_B, and S_C) in Ford-Lighthill equation, which is shown in fig. (5.14). The figure shows that although the amplitude of the forcing function S_A (indicated by dashed line) has increased following the merging, however, so has the damping effect of rotation indicated by term S_B (represented by dot-dashed line). Fig. (5.14) also shows that the time-scale of fluctuations of Lighthill's forcing terms has increased after the merging of vortices, hence contributing to the increased effect of rotation of Earth.

Figure (5.15) shows the exchange of energy associated with the merging of vortices. It shows that initially the exchange of energy between the mean flow and the perturbations is identical to the result of simulation S1 (see fig. (3.33)). This phase is associated with the roll-up of the primary disturbance, and therefore, will not be discussed further.

The development of the secondary disturbance, which is responsible for vortex merging, is associated with further increase in the perturbation kinetic energy K'. The paired K' is stronger than in the case of simulation S1. A corresponding fall in mean kinetic energy $\overline{K}$, increase in perturbation potential energy P', and mean potential energy $\overline{P}$ can also be observed. Here too, as in the case of simulation S1, we observe that after the vortices have merged the system attains a quasi-periodic state, after which it continues to undergo oscillation about this new state.

5.4   Summary and concluding remarks

The process of merging of vortices was studied using a rotating (constant f-plane) shallow-water model.

Our study showed how the adjustment of near-field mass takes place to

accommodate the merging of vortices, and how the near-field mass fluctuations differ from the case of a pair of non-merging vortices. It was observed that merging of vortices results in the release of more mean kinetic energy from the background zonal shear. However, after the vortices have merged, the subsequent evolution strongly resembles that of a single vortex, which was considered in simulation S1.

As in the case with simulation S1, the system, after an initial adjustment, attains a quasi-periodic state and continues to undergo oscillations about this new state. It is during these oscillations that a small fraction of the energy leaks away as shallow-water gravity waves. One would have expected the wave amplitudes and wavelengths to increase since the merged vortex is larger and stronger. However, it was observed that merging of vortices did not produce any discernible change in the characteristics of the emitted gravity wave.

The lack of increase in the amplitude of the gravity waves following the merging was attributed to lack of significant increase in maximum amplitude near-field divergence δ. The study further showed that that the time-scale of fluctuation of the wave forcing terms increased following the merging compared to the single vortex case, hence increasing the inhibiting effect of rotation of Earth.
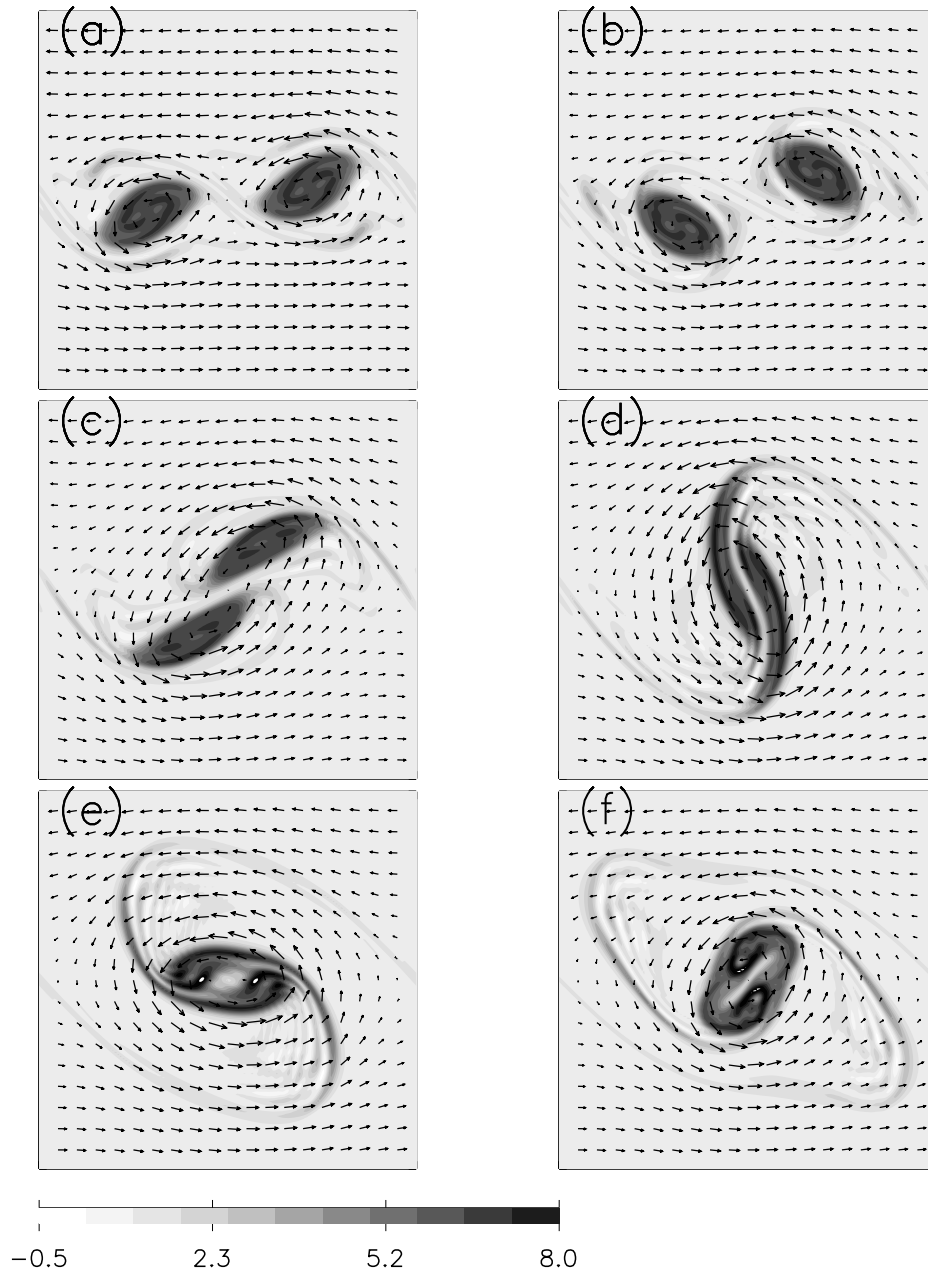
Figure 5.1: Figure illustrating merging of vortices. The gray-scale indicates the potential vorticity field η/η_b, where $\eta_b = h_r/f$. The horizontal and the vertical axes represents the downstream distance (x) and the cross-stream (y) distances, respectively, in units of R_d. The x-domain range is $(0, 0.45)$ and y-domain range is $(-0.2, 0.2)$. Frames (a), (b), (c), (d), (e), and (f) corresponds to times $t = 19.2$, 20.8, 22.4, 24.0, 25.6, and 27.2, respectively. Time is in units of $1/f$. Wind field vector $\mathbf{v}$ has been overlaid on it. The magnitude of longest wind vector is ≈ 3.55 ms^{-1}. Results are from simulation VM.
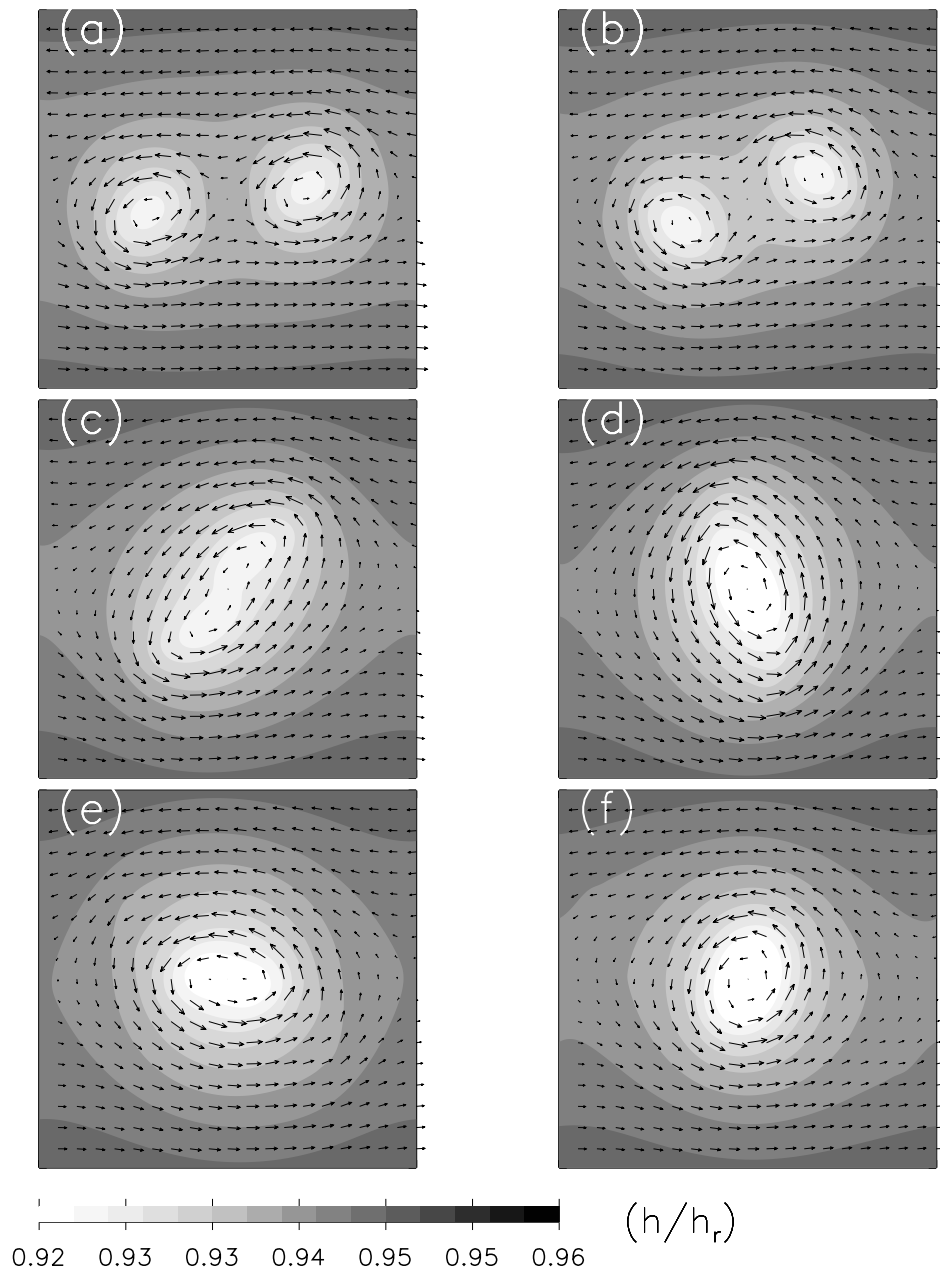
Figure 5.2: Same as fig.(5.1), but showing the fluctuation in the pressure field associated with merging of vortices.
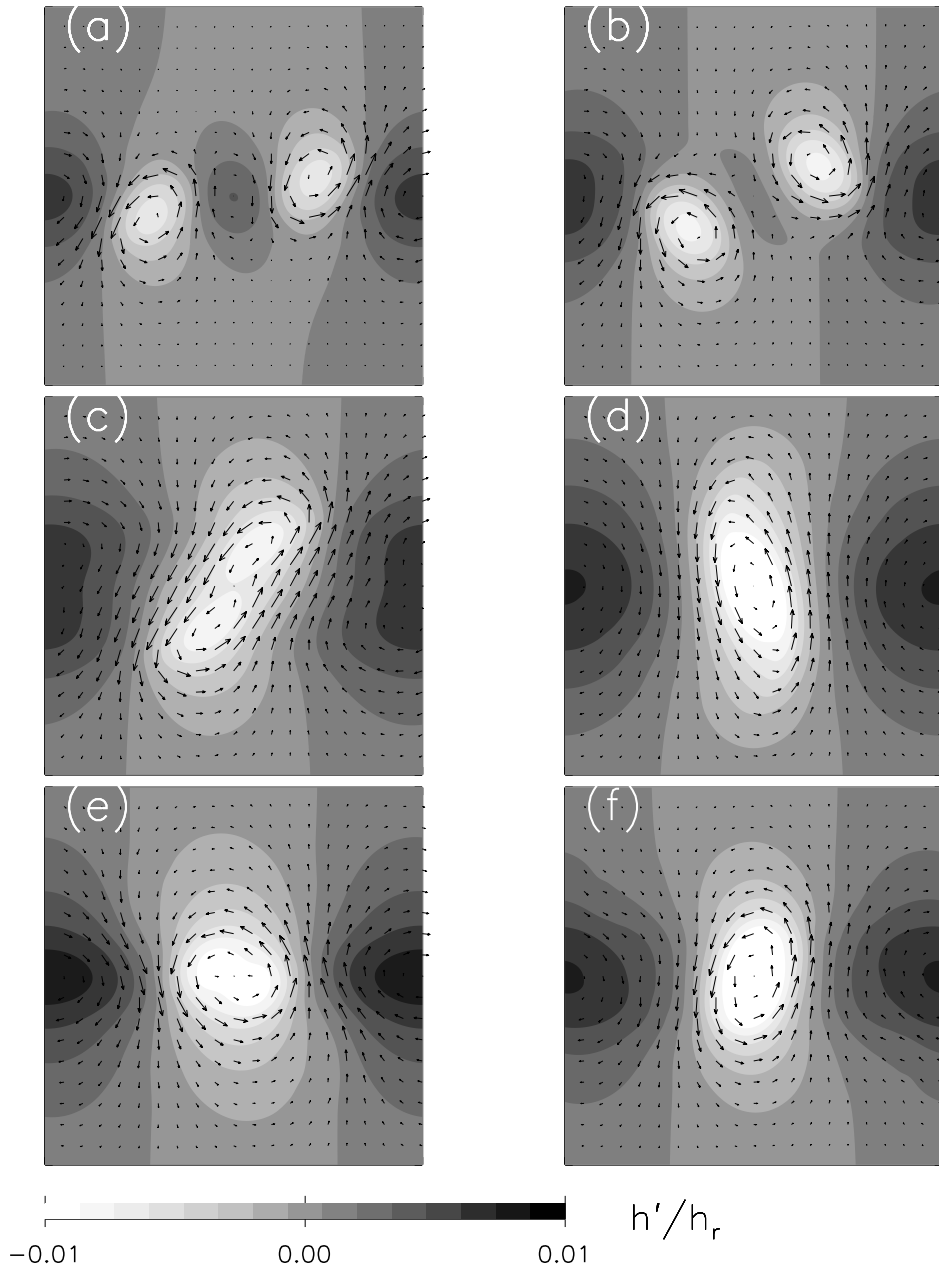
Figure 5.3: Same as fig. (5.1), but showing the fluctuation in the perturbation pressure (h'). Also shown is the perturbation wind $\mathbf{v}'$.

151
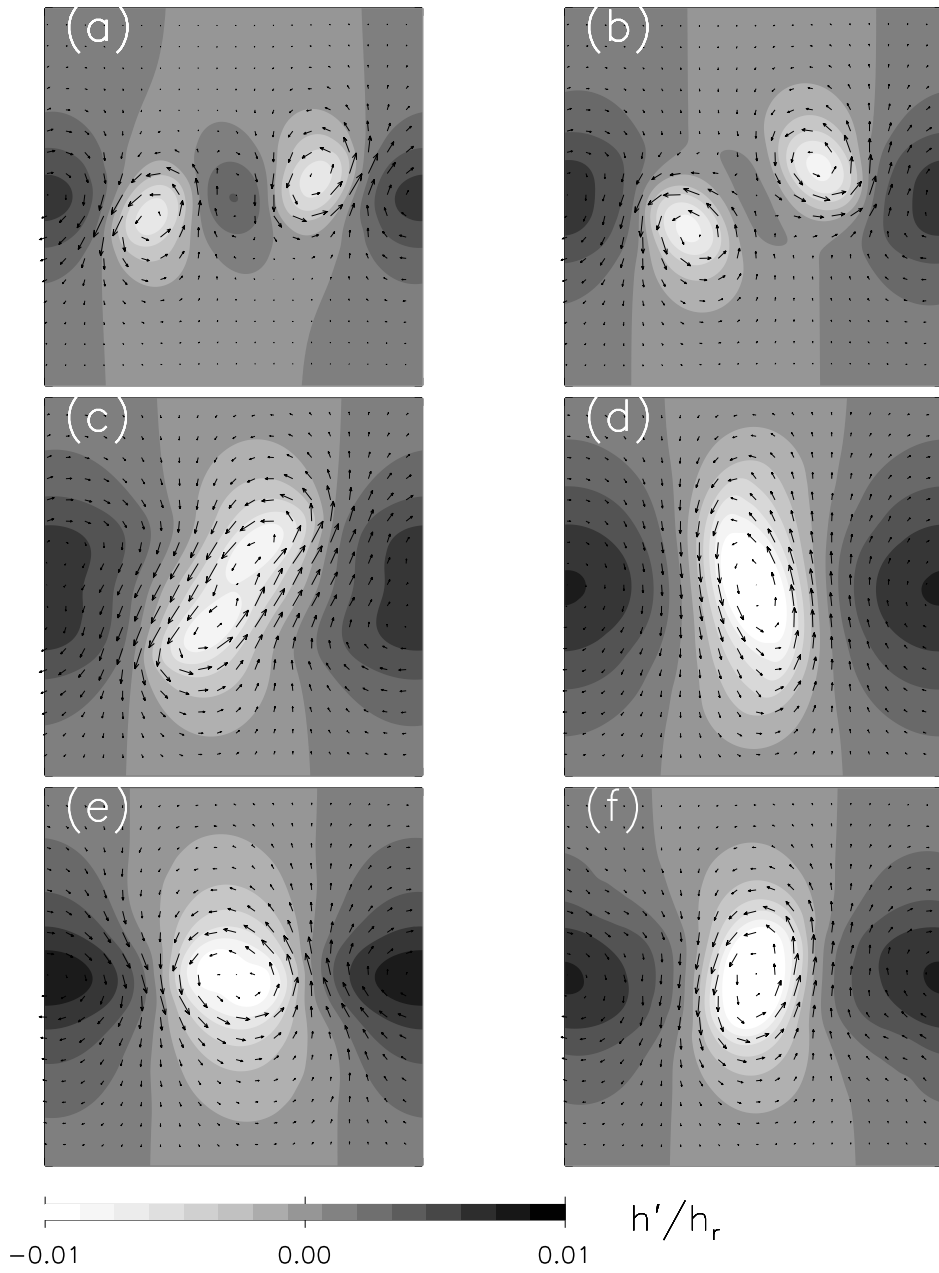
Figure 5.4: Same as fig. (5.3), but shown is the perturbation *rotational* wind $\mathbf{v}'_\psi$. The wind speed maximum is ~ 3.0 m/s, where $\mathbf{v}'_\psi = (\hat{\mathbf{k}} \times \nabla\psi)$, and $\nabla^2\psi = \zeta$.
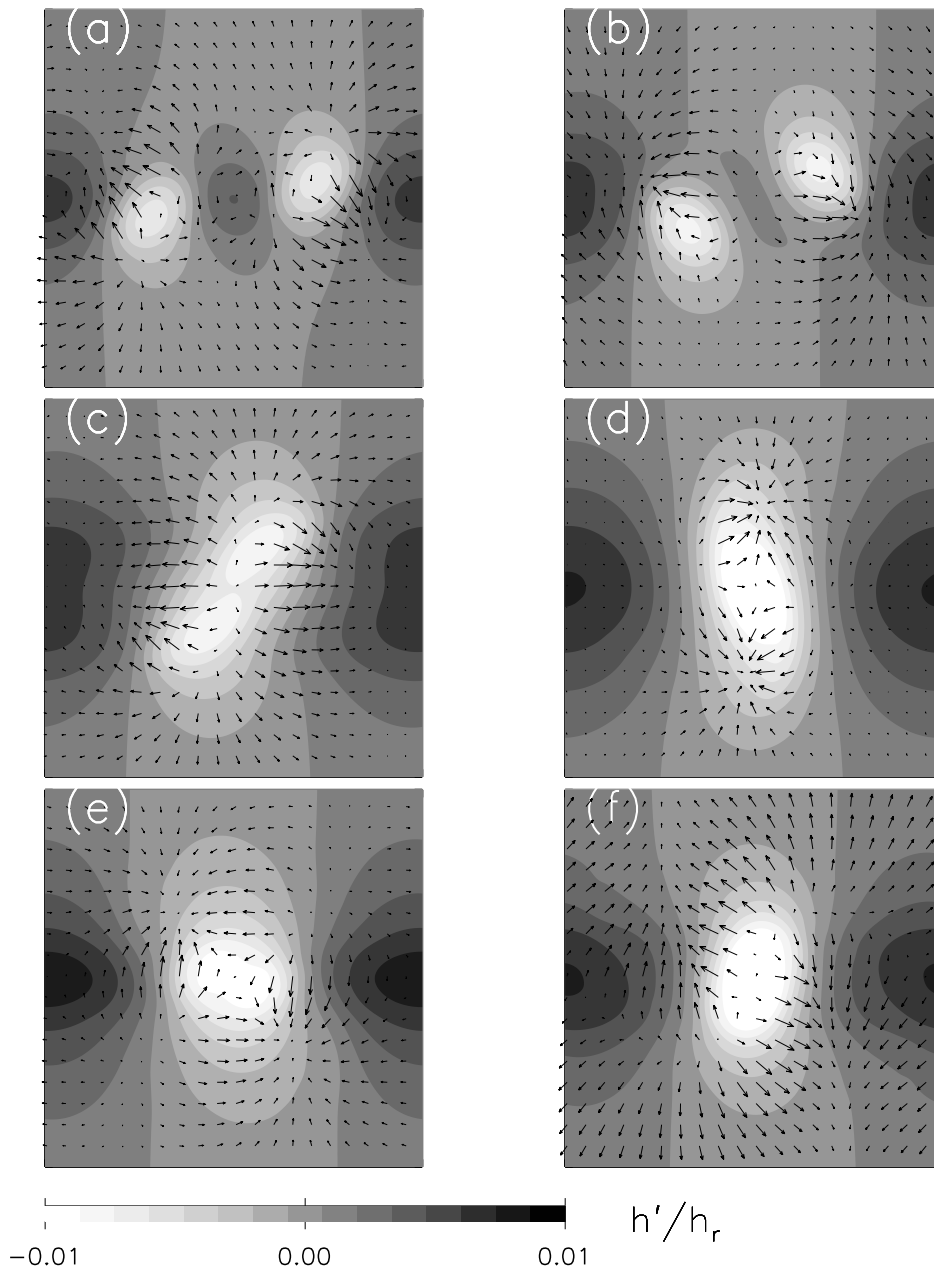
Figure 5.5: Same as fig. (5.3), but shown is the perturbation *divergent* wind $\mathbf{v}'_\chi$. The wind speed maximum is .005 m/s, and wind amplitude $|\mathbf{v}'_\chi|$ is of the order of magnitude 10^{-3} smaller than $|\mathbf{v}'_\psi|$, where $\mathbf{v}'_\chi = \nabla\chi$, and $\nabla^2\chi = \delta$.

153
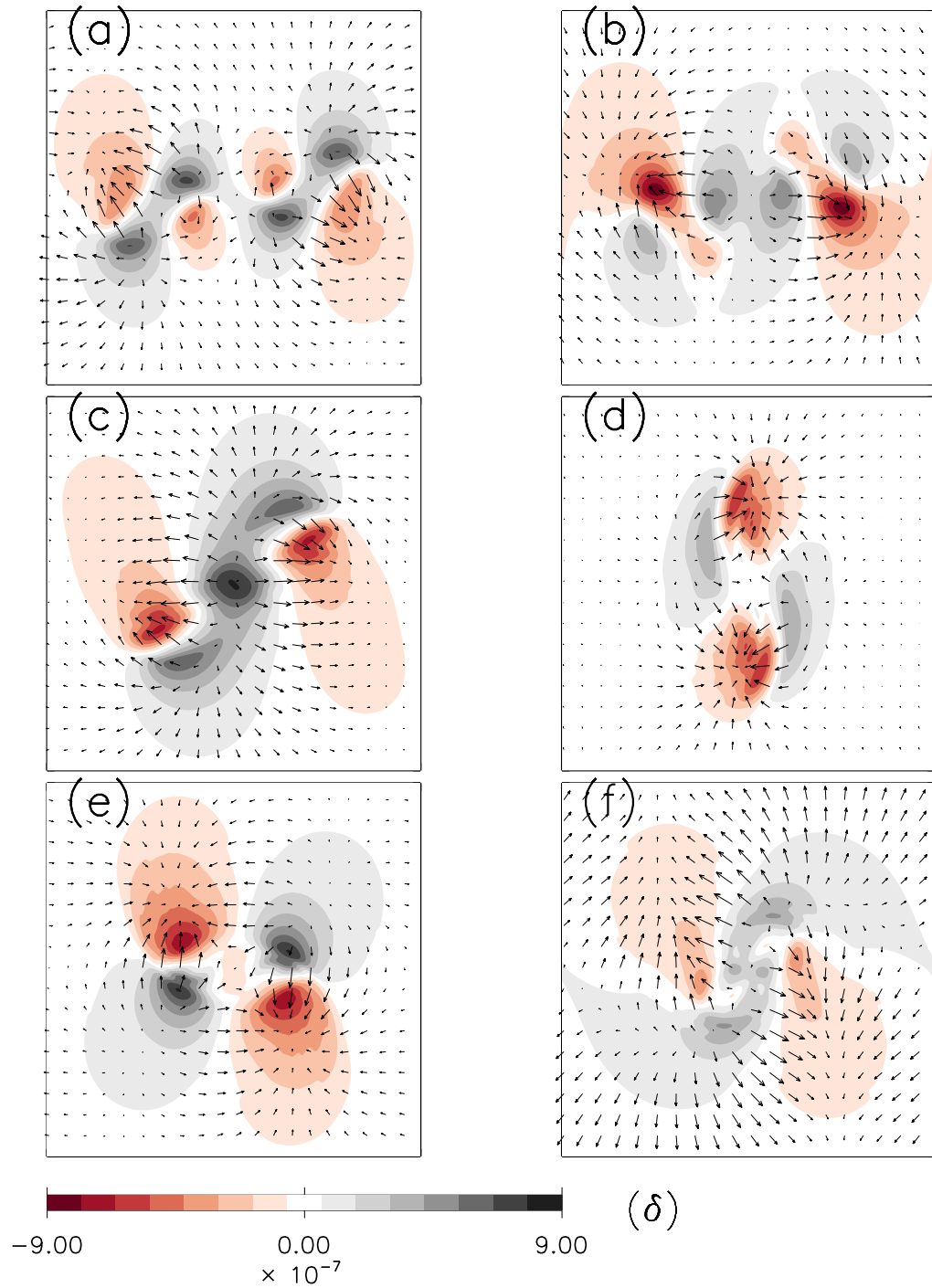
Figure 5.6: Same as fig. (5.1), but showing near-field divergence (δ). Unit of δ is s^{-1}. Also shown is $\mathbf{v}'_\chi$

.
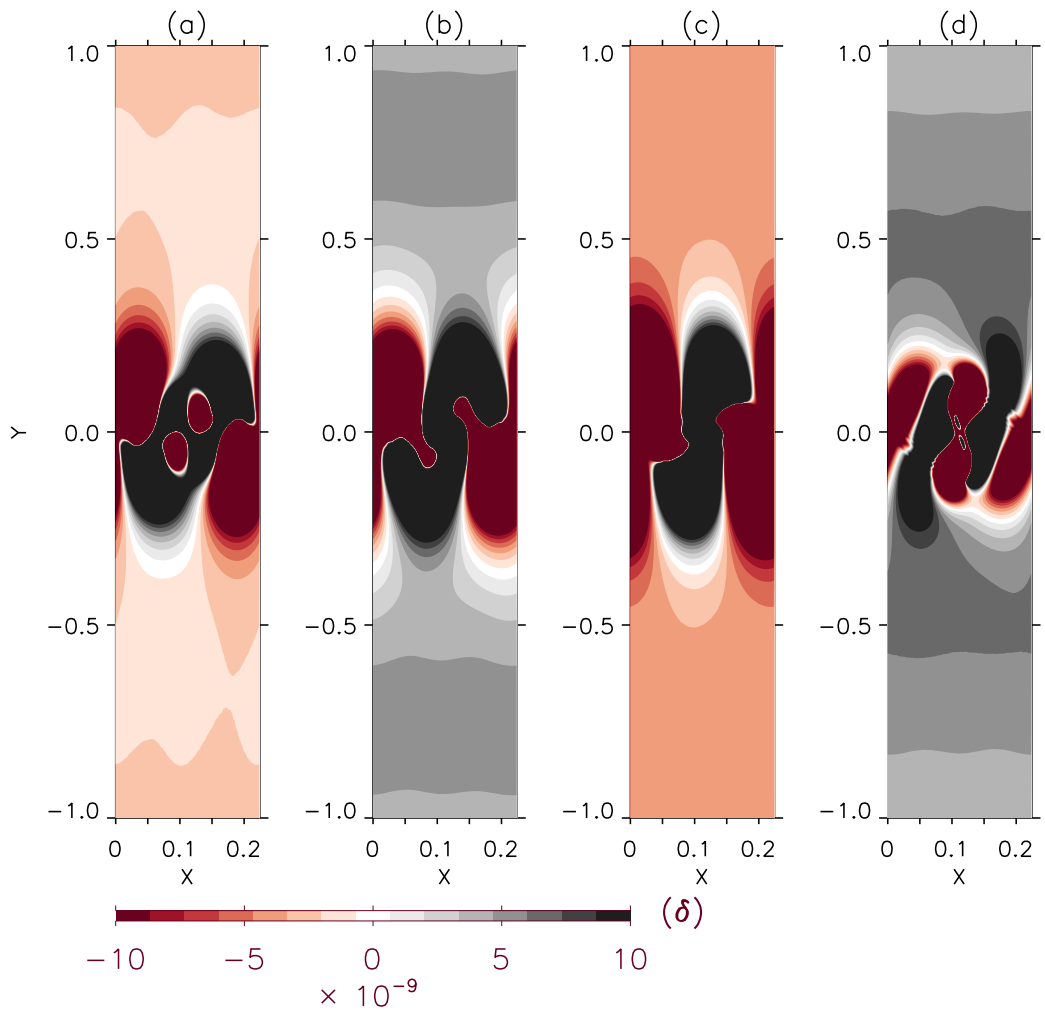
Figure 5.7: Figure showing the *intermediate* field divergence δ. Unit is s^{-1}. Note that the plot times of frames (a) – (d) corresponds to the plot times of frames (a)–(d) of fig. (5.6).
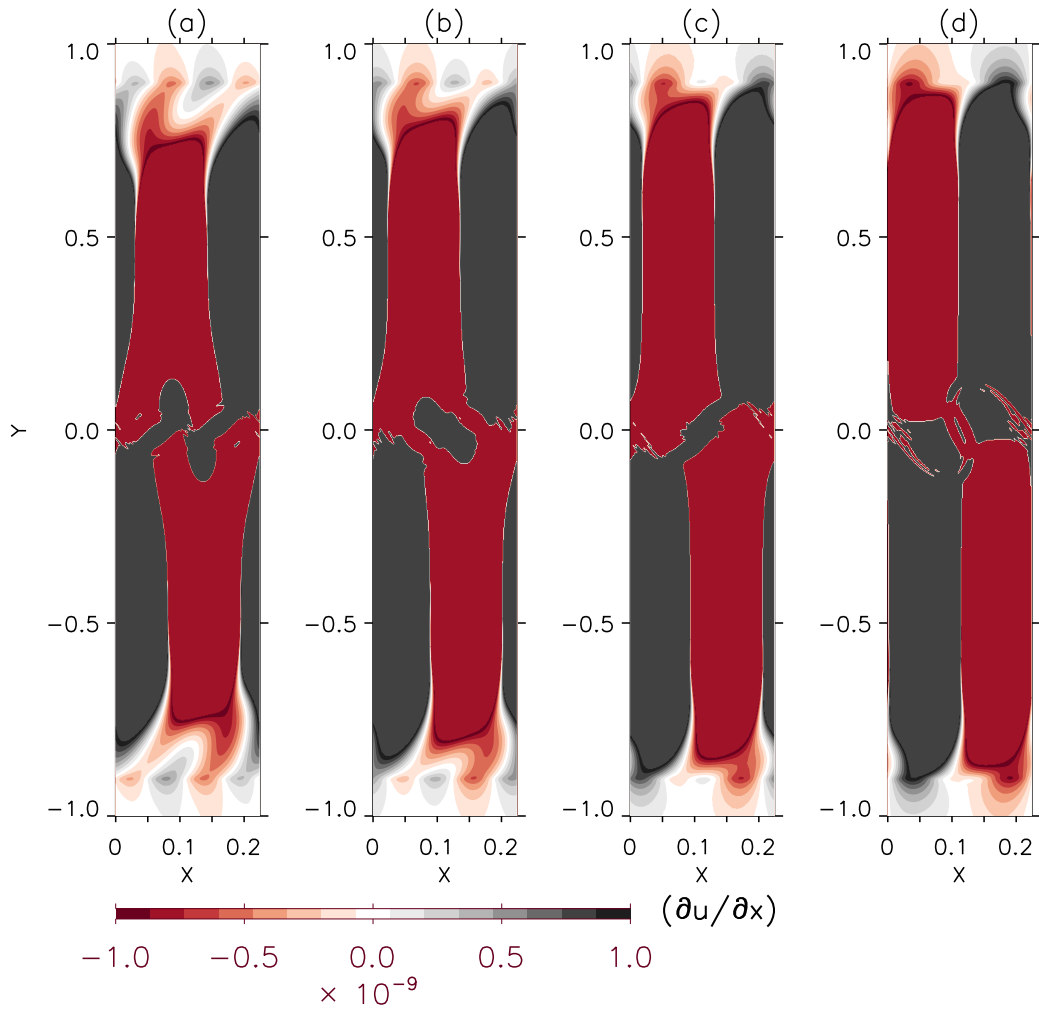
Figure 5.8: Same as (5.7), but showing $(\partial u/\partial x)$.
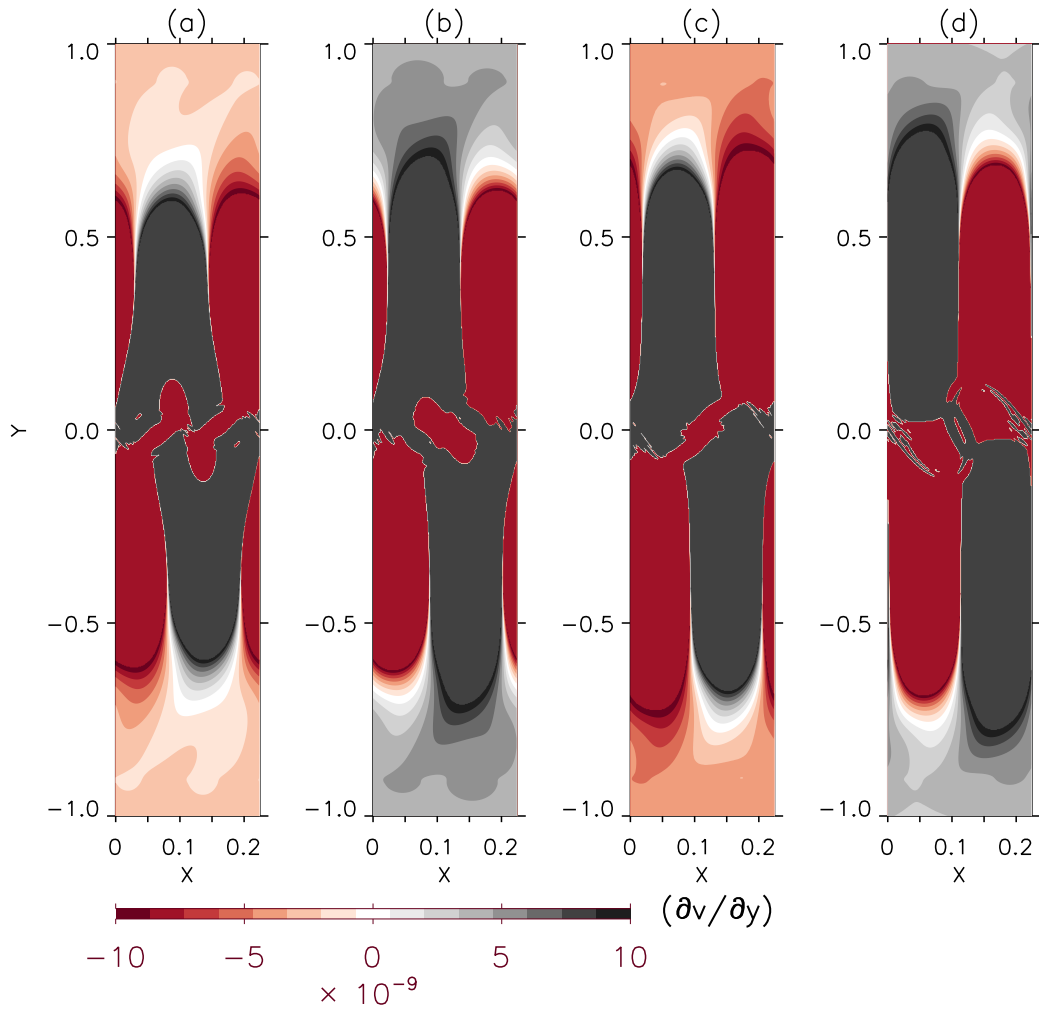
Figure 5.9: Same as fig. (5.7), but showing $(\partial v/\partial y)$.
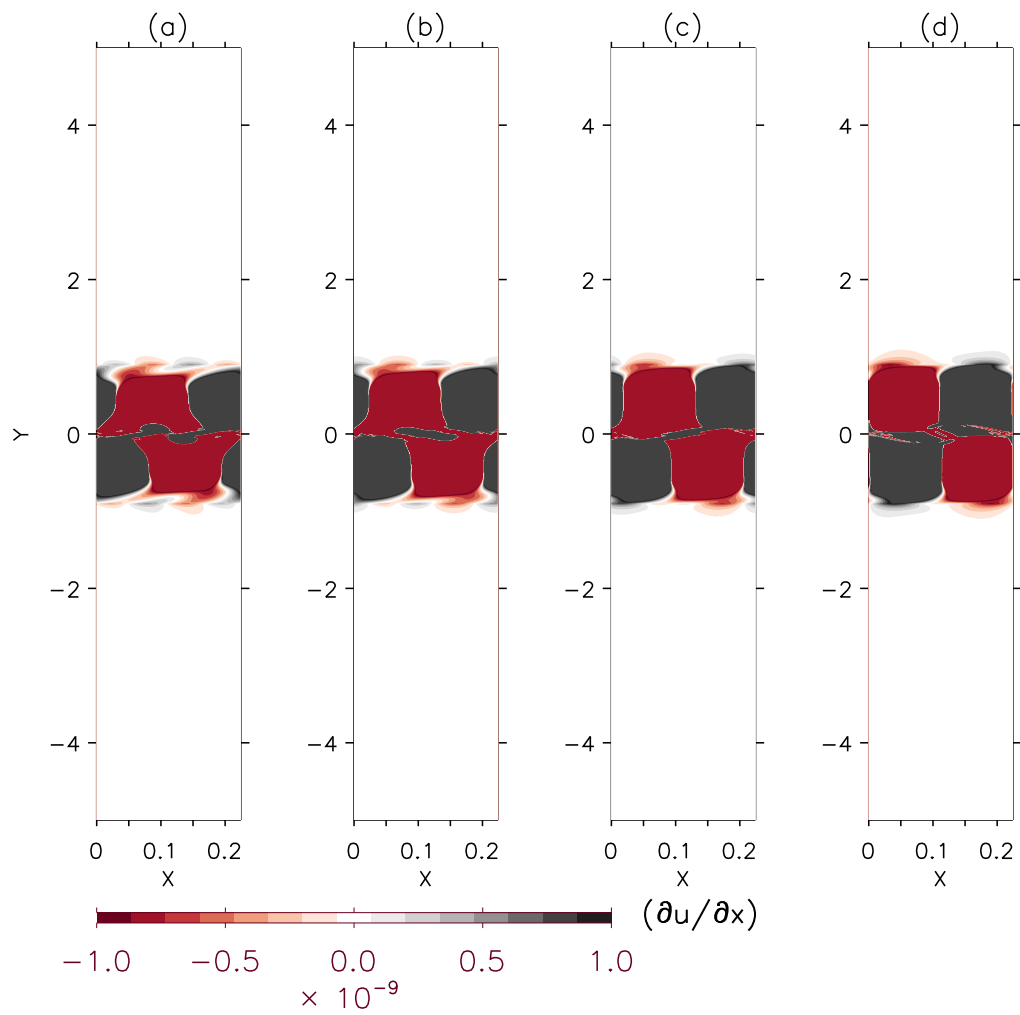
Figure 5.10: Same as fig. (5.8), but showing the far-field $(\partial u/\partial x)$.
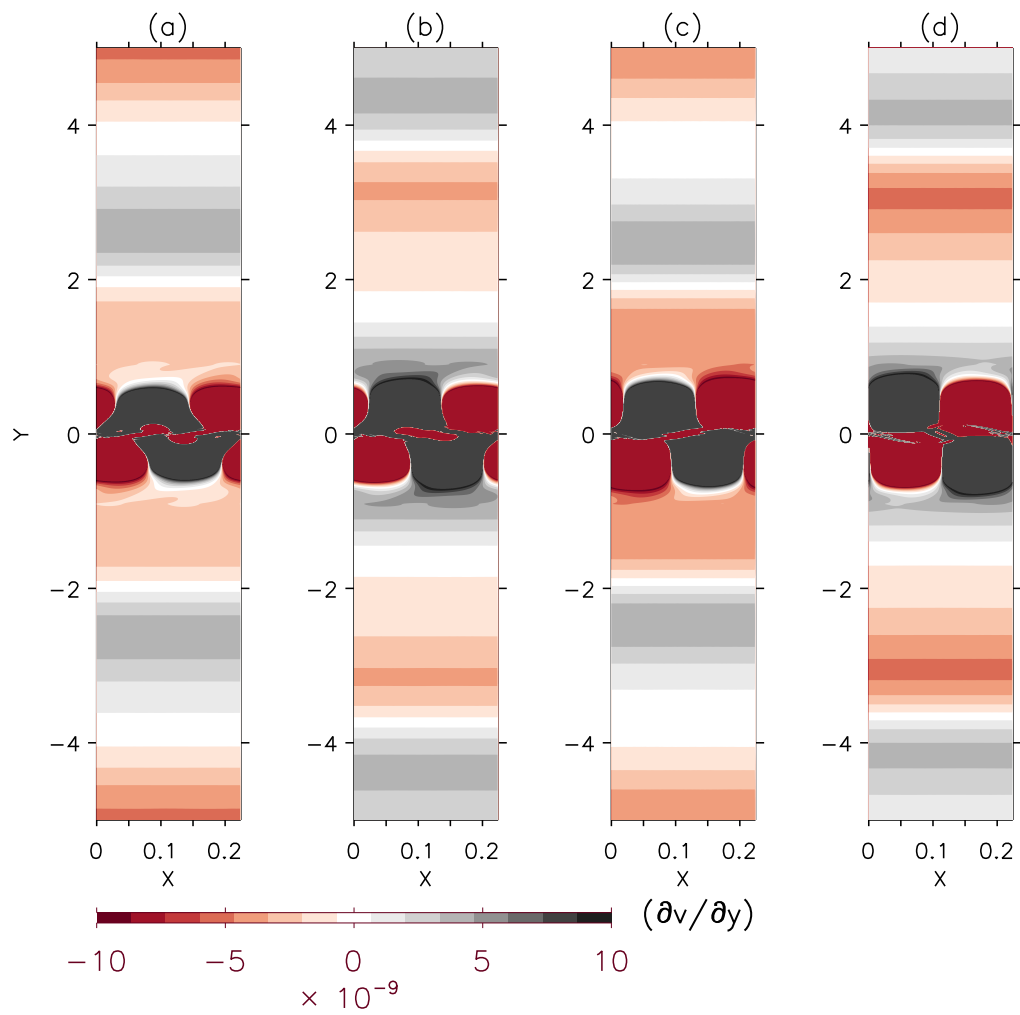
Figure 5.11: Same as (5.10), but showing $(\partial v/\partial y)$.

159
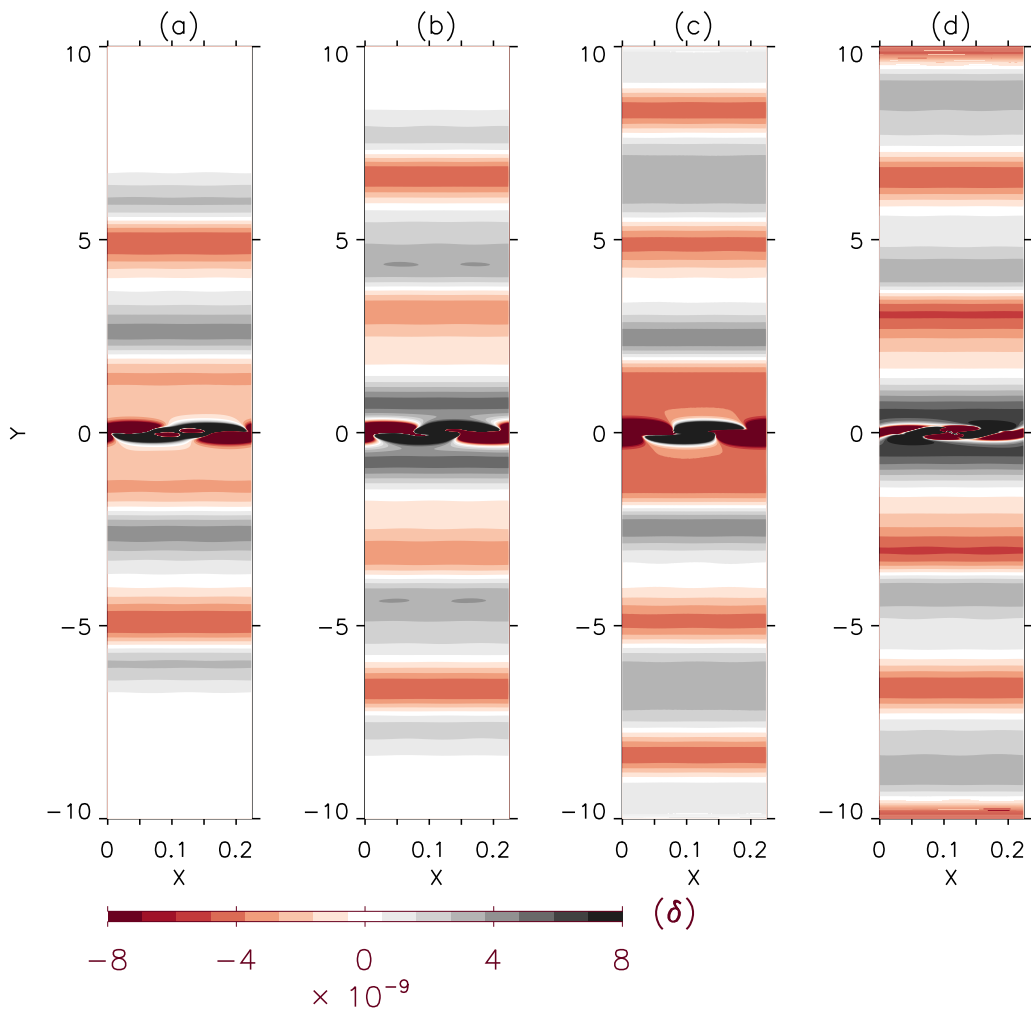
Figure 5.12: Figure showing the propagation of the gravity in the divergence (δ) field. Frames (a) - (d) corresponds to times $t = 19.2, 20.8, 22.4, 24.0$.
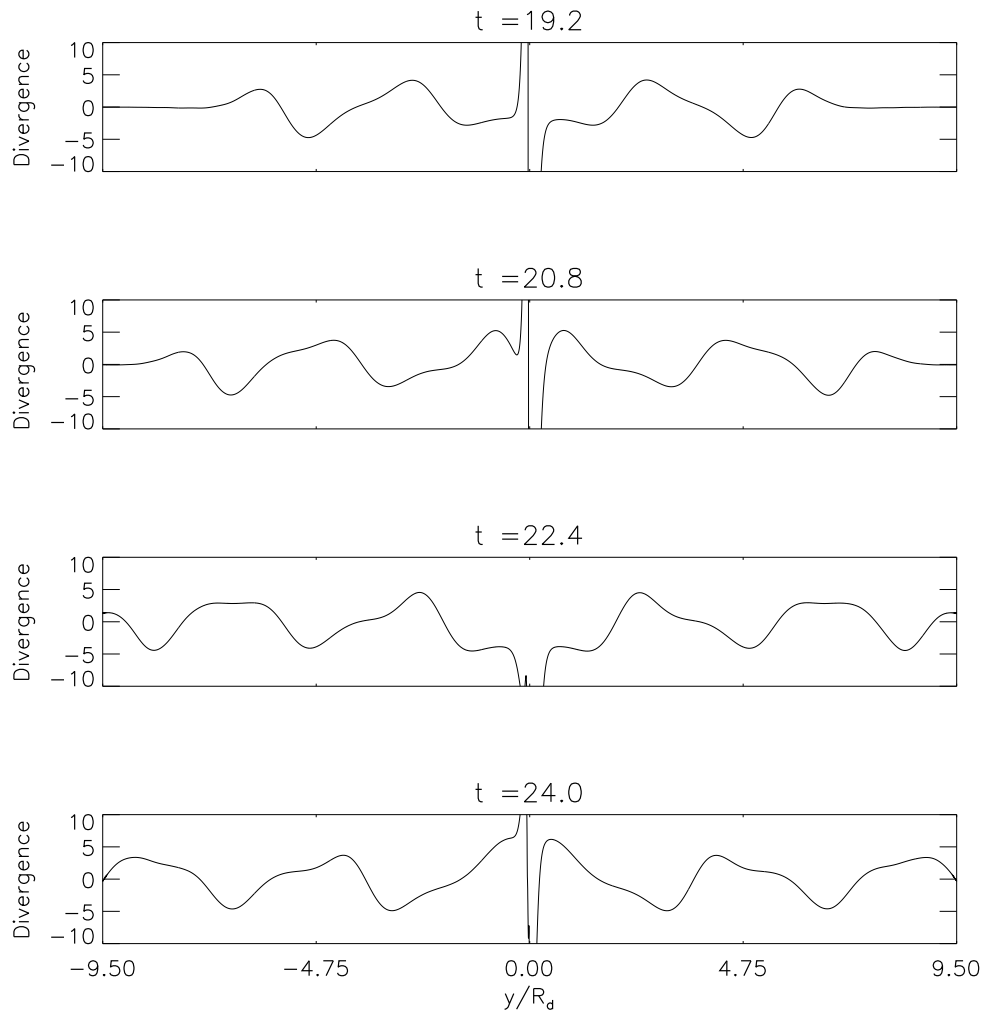
Figure 5.13: Figure showing the meridional cross-section of wave observed in fig. (5.12) along $x = .05625 R_d$. Divergence is expressed in units 10^{-9} s^{-1}.
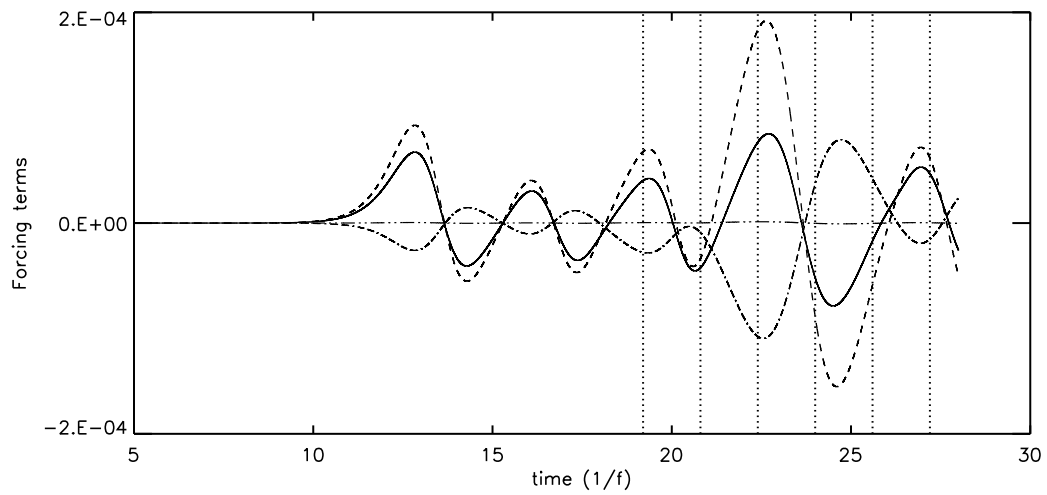
Figure 5.14: Temporal variation of the forcing function S[t] $(= \int_{-\infty}^{+\infty} \overline{T_{22}}^x dy)$ for simulation VM. Solid line indicates S $(= S_A + S_B + S_C)$, dashed line indicated S_A, dot-dashed line shows S_B, and dot-dot-dashed line shows S_C. See expression (4.16) for definition of S_A, S_B, and S_C.

162
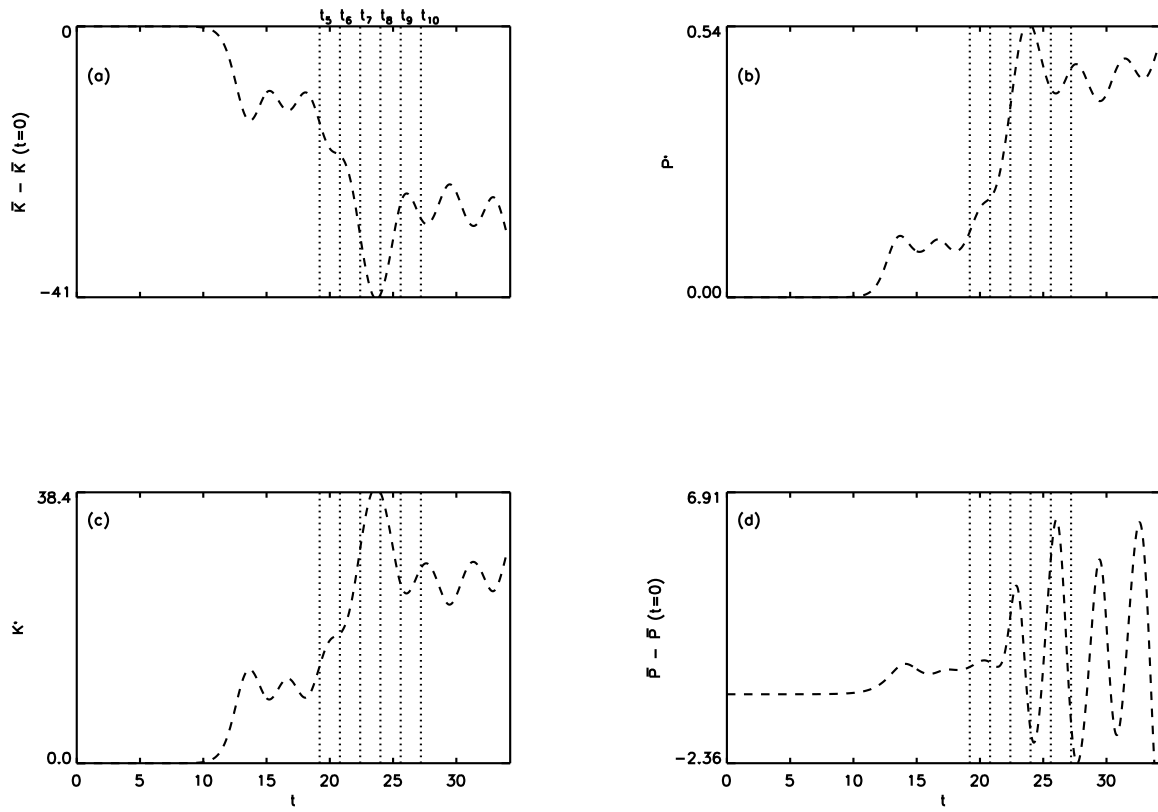
Figure 5.15: Figure showing temporal variations of **(a)** $\overline{K}$ - $\overline{K}(\mathrm{t}=0)$, **(b)** P', **(c)** K', **(d)** $\overline{P}$ - $\overline{P}$ $(\mathrm{t}=0)$. The dotted lines which are labeled t_5 - t_{10} correspond to plot times of frames (a) - (f), respectively, in figure (5.1).

163

Chapter 6

Summary, concluding remarks, and future work

6.1 Introduction

Over the last decade or so, our understanding of internal gravity wave emission from atmospheric jets and baroclinic vortices, specifically the so-called *spontaneous emission*, has improved significantly. There have also been studies of gravity wave emission from barotropic vortices. Our understanding of gravity wave emission from barotropic vortices has come mainly from Lighthill's (1952) theory of aerodynamic generation of sound, and our understanding of gravity wave emission from barotropic vortices in a rotating fluid have come from Ford's (1994a) extension of Lighthill's (1952) theory to rotating fluids. Yet, based on our current understanding it is difficult to draw a clear distinction between wave emission mechanism in barotropic and baroclinic vortices, which suggests a deeper understanding of the wave emission is required than that which is currently known.

The present thesis revisited the problem of shallow-water gravity wave emission from barotropic vortices in rotating fluids. Our aim was to seek a better understanding of the process of shallow-water gravity wave emission from these vortices.

Our approach, like the other studies in the past, used numerical simulations to study gravity wave generation from vortices developing in an unstable barotropic jet. Specifically, we chose to revisit the problem investigated by Ford (1994a), and performed a more detailed investigation compared to the earlier studies, because 1) Ford's (1994a) results could be used for purposes of bench-marking, and 2) there were some important aspects associated with the wave emission mechanism which were not addressed by Ford (1994a).

Specifically, one important issue concerning the wave emission mechanism that has not been discussed in the past can be understood as follows: The propagating shallow-water gravity waves that were emitted during Ford's (1994a) simulations showed minimal zonal or stream-wise variations. An explanation for this lack of zonal variation has not been provided.

Secondly, Ford's (1994a) extension of Lighthill's (1952) theory to rotating shallow-water flows led to the inclusion of a term on the wave forcing side of the Ford-Lighthill equation. The details and significance of this term for the wave emission mechanism has not been investigated in the past.

6.2   Summary of our main findings

Since the present study conducted a more detailed study of the process of shallow-water gravity wave emission from an unstable barotropic jet, important new details about the wave emission mechanism were revealed, which has provided a much

clearer and more intuitive picture of the wave generation process. Below we briefly summarize some of our new findings. These findings have been divided into three categories.

6.2.1   Insight on the wave generation mechanism

Our study has revealed that the process of wave generation associated with the instability of a parallel jet is more complex, and the picture is not as straight forward as can be understood on the basis of Lighthill's formulation, where the whole process of wave emission is explained on the basis of a non-homogeneous wave equation, with non-homogeneous terms regarded as wave forcing terms. Important fundamental details associated with the process of gravity wave generation from oscillating vortices are sidestepped, which makes formulation and the wave forcing terms difficult to interpret.

A much better insight into the problem of gravity wave emission from oscillating vortices, and a better physical interpretation of the wave forcing terms can be obtained by treating process of wave emission as comprising of two phases. Phase one is associated with the roll-up of the jet due to instability. During this phase, as the instability develops it causes the jet to roll-up during which there occurs a transfer of zonal mean kinetic energy to perturbation energy. This phase is characterized by intensification of near-field fluid circulations, both cyclonic and anticyclonic. This intensification of the circulations is accompanied by transfer of mass by the *rotational* wind from the low to the high pressure centers, which results in increase of perturbation potential energy.

Importantly, for the purpose of understanding the wave forcing terms, the intensification phase is also accompanied by some cross-isobaric flow produced by the *rotational* wind flowing across the zonal mean height field. Such cross-

166

isobaric flows produce fluctuations in the local mean zonal height field. Since the *rotational* wind has to do work in producing fluctuations in the zonal mean height, it loses some of its *rotational* kinetic energy in doing so. Therefore, the cross-isobaric rotational flow provides the necessary impetus required to force the shallow-water gravity waves away from the vortical region. Shallow-water gravity waves are essentially wave-like fluctuations in the divergence field. Therefore, they carry energy associated with divergent fluid motion. However, the energy associated with the *rotational* wind is not directly transferred to energy associated with *divergent* fluid motion, i.e., the forcing does not result in direct emission of gravity waves, instead it is accompanied by an intermediate process. This occurs because divergence and vorticity are physically independent properties, and the wind fields, which carry the energy, are also independent. The intermediate process is accompanied by appearance of singularities in *divergent* wind field. These singularities are the *sources* and *sinks*. In the case of simulated vortices, two such pairs of source and sinks are visible, therefore, constituting a *quadrupole source*. Importantly, the location of these sources and sinks do not coincide with the low and high pressure centers associated with cyclonic and anti-cyclonic circulations, indicating that the sources and sinks are not associated with the intensification of the circulations.

Furthermore, the sources and sinks are accompanied by *divergent* wind field, and the direction of the wind is from the sources to the sinks. Study showed that the *rotational* wind field associated with the fluctuations in the vorticity field remains confined to the near-field region. In contrast, the *divergent* wind field is able to transport mass from the near to the intermediate field. The mass that is transferred to the intermediate region by the divergent wind does not traverse beyond the intermediate region and recedes back to the near-field region during the *relaxation phase*, which is discussed in the next paragraph. Lastly, the divergence

field also consists of wave-like fluctuations, which continues to propagate away from the intermediate region as shallow-water gravity waves, even after the mass from the intermediate field have receded. However, the energy carried by the shallow-water waves is a tiny fraction of the total divergent energy.

The relaxation phase is characterized by the following observations. After the near-field circulations have attained a maximum intensity, the vortices begin to relax. This relaxation is associated with decrease of the perturbation kinetic energy and increase of zonal mean kinetic energy. During this phase, the circulations weaken, and this weakening is accompanied by transfer of mass from the high to the low-pressure centers by the *rotational* wind. This phase is also accompanied by withdrawal of some but not all of the mass that was expelled to the intermediate region during the intensification phase. This withdrawal assures that the mass of the system remains conserved.

After the relaxation phase, the vortices do not attain a steady state, but repeat the cycle of intensification and relaxation, and therefore provide the forcing necessary for the continuous emission of shallow-water gravity waves, and in the process the vortices lose a small fraction of their rotational energy as shallow-water gravity waves.

Such an in-depth analysis has not been conducted by earlier studies (e.g., Ford 1994a; Sugimoto et al. 2008). Our study also helps to understand why the wave forcing terms in Ford-Lighthill's equation can be so difficult to interpret.

6.2.2 Near-field numerical error and their insensitivity to the gravity waves emitted

The present study also discussed the numerical errors that arises in the simulation of near-field features as consequence of nonlinear evolution of the potential vorticity anomaly. Specifically, the numerical errors arose as a consequence of the model not being able to resolve the steepening of the PV-gradient. A sensitivity study of these errors to the process of gravity wave generation was performed. Interestingly, our results showed that the emitted waves are insensitive to these errors. The characteristics of the emitted waves were also found to be insensitive to varying numerical dissipation.

These results suggests that small-scale errors in the description of the near-field features are not important to the wave emission mechanism in rotating shallow-water flow. This is another important finding based on our study which provides additional insight on the wave forcing mechanism.

6.2.3 Effect of rotation of Earth on the gravity wave emission

Ford's (1994a) extension of Lighthill's (1952) theory to rotating shallow-water flows led to introduction of a new Coriolis term, which was included on the wave forcing side of the non-homogeneous wave equation. The nature of this term, and its role in the wave generation mechanism had not been discussed in the past. The present study investigated the nature of this term, and highlighted the significance of this term to the gravity wave generation mechanism. This study showed that this term captures the inhibiting effect of the planetary vorticity on fluid motions.

6.2.4 Wave emission associated with merging of vortices

Simulations were conducted to study the wave emission mechanism associated with merging of barotropic vortices using a rotating (constant f-plane) shallow-water model. Our study showed that merging results in the release of more mean kinetic energy to perturbation kinetic energy. The vortex formed as a consequence of merging was bigger and stronger compared to the vortices studied in the simulation S1. However, it was observed that merging did not produce significant change in the amplitude of the emitted gravity wave, when compared with the gravity waves observed in the single vortex case of simulation S1. The reason for this lack of increase in the wave amplitude was investigated, and it was found that it is a consequence of increased inhibiting effect of rotation of the Earth.

This study also showed that almost all of the adjustment in the mass or pressure fluctuations associated with merging of vortices is produced by the rotational component $\mathbf{v}'_\psi$ of the wind field. In contrast, the divergent component $\mathbf{v}'_\chi$ of the wind is responsible for producing only a tiny fraction of the total mass or pressure adjustment. This tiny fraction is, however, very important for production of gravity waves.

6.3 Concluding remarks

The present study has provided a much clearer picture of how shallow-water gravity waves are emitted from oscillating barotropic vortices. Our investigation has led us to a very interesting and important findings about how the energy transfer, i.e,, from rotational to divergent energy, occurs between two independent fields. Our study has also helped to provide a better insight and therefore, appreciation of Ford-Lighthill forcing terms.

Our study also showed that in common with dipole vortices, which are considered as an idealization of the atmospheric jet streak, the wave forcing in simulated barotropic vortices also occurred from the jet between the two counter-rotating vortices in the perturbation fields. It is our hope these findings will also help in understanding internal gravity wave emission from realistic atmosphere jets and vortices, and serve towards drawing a better distinction between the mechanisms observed in barotropic and baroclinic vortices.

6.4   Future work

As a future work, we recommend that the following topics warrant further investigation:

- Our study showed that only a tiny fraction of the divergent energy leaks as gravity waves. However, it was not clear what factors determine how much of the divergent energy should leak as gravity waves. More research and deeper understanding is required before such questions can be answered.

- Our study highlighted some new effects which play a vital role in the genesis of divergence in barotropic shallow-water fluid motions. It is only natural to seek the consequences of these new effects in baroclinic flows.

Bibliography

Aris, R., 1989: *Vectors, Tensors, and Basic equations of Fluid mechanics.* Dover Publication, 286 pp.

Asselin, R., 1972: Frequency filter for time integration. *Mon. Wea. Rev.*, **100**(6), 487–490.

Baines, P., 1998: *Topographic effects in Stratified flows.* Cambridge University Press, 500 pp.

Blumen, W., 1972: Geostrophic adjustment. *Rev. Geophys. Space Phys.*, **10**, 485–528.

Cahn, A., 1945: An investigation of the free oscillations of a simple current system. *J. Meteor.*, **2**(2), 113–119.

Crighton, D., 1975: Basics principles of aerodynamic sound generation. *Progress in Aerospace Sciences*, **16**(1), 31–96.

Cunningham, P., and D. Keyser, 2000: Analytical and numerical modelling of jet streaks: Barotropic dynamics. *Quart. J. Roy. Meteor. Soc.*, **126**, 3187–3217.

Cushman-Roisin, B., and J. M. Beckers, 2010: *An Introduction to Geophysical Fluid Dynamics.* Second Edition, Academic Press, pp.

Durran, D., 2010: *Numerical Methods in Fluid Dynamics.* Springer, 511 pp.

Ford, R., 1994a: Gravity radiation from vortex trains in rotating shallow water. *J. Fluid Mech.*, **281**, 81–118.

Ford, R., 1994b: Instability of axisymmetric vortex with monotonic potential vorticity in rotating shallow water. *J. Fluid Mech.*, **280**, 303–334.

Ford, R., M. McIntyre, and W. Norton, 2000: Balance and the slow quasimanifold: Some explicit results. *J. Atmos. Sci.*, **57**, 1236–1254.

Fritts, D. C., and M. J. Alexander, 2003: Gravity wave dynamics and effects in middle atmosphere. *Review of Geophysics*, **41**, 1–64.

Gill, A., 1982: *Atmosphere Ocean Dynamics*. Academic Press, Inc., 645 pp.

Harada, M., and K. Ishioka, 2011: Inertia-gravity wave radiation from an unstable bickley jet in rotating two-layer shallow water. *SOLA*, **7**, 113–116.

Holton, J. R., 2004: *An Introduction to Dynamic Meteorology*. Academic Press, Inc., San Diego, 554 pp.

Houghton, D., W. Campbell, and N. Reynolds, 1981: Isolation of the gravity-inertial motion component in a nonlinear atmospheric model. *Mon. Wea. Rev.*, **109**, 2118–2130.

Jiang, Q., 2014: Applicability of reduced-gravity shallow-water theory to atmospheric flow over topography. *J. Atmos. Sci.*, **71**, 1460–1480.

Klaassen, G. P., and W. R. Peltier, 1989: The role of transverse secondary instabilities in the evolution of free shear layers. *J. Fluid Mech.*, **202**, 367–402.

Kundu, P., 1990: *Fluid Mechanics*. Academic Press, San Diego, 638 pp.

Lighthill, M. J., 1952: On sound generated aerodynamically, i general theory. *Proc. R. Soc. Lond.*, **A 211**, 564–587.

Lighthill, M. J., 1978: *Waves in fluids*. Cambridge University Press, pp.

Lipps, F. B., 1970: Barotropic stability and tropical disturbances. *Mon. Wea. Rev.*, **98**(2), 122–131.

Maejima, Y., K. Iga, and H. Niino, 2006: Upper-tropospheric vortex street and its formation mechanism. *SOLA*, **2**, 80–83.

Mendez-Nunez, L., and J. J. Carrol, 1993: Comparison of leapfrog, smolarkiewicz, and marcormack schemes applied to nonlinear equations. *Mon. Wea. Rev.*, **121**, 565–579.

Mishra, S. K., V. B. Rao, and S. H. Franchito, 2007: Genesis of the northeast brazil upper-tropospheric cyclonic vortex: A primitive equation barotropic instability study. *J. Atmos. Sci.*, **64**, 1379–1392.

Morse, P. M., and H. Feshback, 1953: *Methods of Mathematical Physics II*. McGraw Hill, pp.

Nieto Ferreira, R., and W. Schubert, 1997: Barotropic aspects of itcz breakdown. *J. Atmos. Sci.*, **54**, 261–285.

O'Sullivan, D., and T. J. Dunkerton, 1995: Generation of inertia-gravity waves in a simulated life cycle of baroclinic instability. *J. Atmos. Sci.*, **52**, 3695–3716.

Plougonven, R., and C. Snyder, 2005: Gravity waves excited by jets: Propagation versus generation. *Geophysical Research Letters*, **32**.

Plougonven, R., and C. Snyder, 2006: Inertia-gravity waves spontaneously generated by jets and fronts, part 1: Different baroclinic life cysles. *J. Atmos. Sci.*, **64**, 2502–2520.

Plougonven, R., and F. Zhang, 2014: Internal gravity waves from atmospheric jets and fronts,. *Review of Geophysics*, **52**.

Ripa, P., 1983: General stability conditions for zonal flows in a one-layer model on the β-plane or the sphere. *Journal of Fluid Mechanics*, **126**, 463–489.

Robert, A., 1966: The integration of a low order spectral form of the primitive meteorological equations. *J Meteor Soc Jpn*, **44**, 237–244.

Rossby, C. G., 1938: On the mutual adjustment of pressure and velocity distributions in certain simple current systems, ii. *J. Marine Res.*, **1**, 239–263.

Sadourny, R., 1975: The dynamics of the finite-difference models of the shallow-water equations. *J. Atmos. Sci.*, **32**, 680–689.

Schecter, D., and M. Montgomery, 2006: Conditions that inhibit the spontaneous radiation of spiral inertia gravity waves from intense mesoscale cyclone. *J. Atmos. Sci.*, **63**, 435–456.

Snyder, C., D. Muraki, and R. a. Plougonven, 2007: Inertia-gravity waves generated within a dipole vortex. *J. Atmos. Sci.*, **64**, 4417–4431.

Snyder, C., R. Plougonven, and D. Muraki, 2009: Mechanisms for spontaneous gravity wave generation within a dipole vortex. *J. Atmos. Sci.*, **66**, 3464–3478.

Sugimoto, N., K. Ishioka, and K. Ishii, 2008: Parameter sweep experiments on spontaneous gravity wave radiation from unsteady rotational flow in a f-plane shallow water system. *J. Atmos. Sci.*, **65**, 235–249.

Vanneste, J., 2013: Balance and spontaneous wave generation in geophysical flows. *Annual Review of Fluid Mechanics*.

Vantuyl, A., and J. Young, 1982: Numerical simulation of nonlinear jetstreak adjustment. *Mon. Wea. Rev.*, **110**, 2038–2054.

Wang, S., and F. Zhang, 2007: Sensitivity of mesoscale gravity waves to the baroclinicity of jet-front systems. *Mon. Wea. Rev.*, **135**, 670–688.

Washington, W., and C. Parkinson, 1986: *An Introduction to Three-Dimensional Climate Modelling.* University Science Books, pp.

Wei, J., and F. Zhang, 2014: Mesoscale gravity waves in moist baroclinic jet-front systems. *J. Atmos. Sci.*, **71**, 929–952.

Weinand, B., 2000: Mesoscale shear eddies in the upper troposphere. *Mon. Wea. Rev.*, **128**, 4126–4130.

Yokota, S., H. Niino, and W. Yanase, 2015: Tropical cyclogenesis due to itcz breakdown: Idealized numerical experiments and a case study of teh event in july 1988. *J. Atmos. Sci.*, **72**, 3663–3684.

Zhang, F., 2004: Generation of mesoscale gravity waves in upper-tropospheric jet-front systems. *J. Atmos. Sci.*, **61**, 440–457.

Appendix A

Stability Analysis

The inviscid rotating shallow-water equations are

$$\left(\partial_t + u\partial_x\right)u + \left(\partial_y u - f\right)v + g\partial_x h \;=\; 0 \tag{A.1}$$

$$\left(\partial_t + u\partial_x\right)v + v\partial_y v + fu + g\partial_y h \;=\; 0 \tag{A.2}$$

$$\left(\partial_t + u\partial_x + v\partial_y\right)h + h\left(\partial_x u + \partial_y v\right) \;=\; 0 \tag{A.3}$$

We now rewrite the variables as comprised of basic state and small amplitude perturbations, i.e.,

$$u(x,y,t) = u_0(y) + u'(x,y,t) \tag{A.4}$$

$$v(x,y,t) = v'(x,y,t) \tag{A.5}$$

$$h(x,y,t) = h_0(y) + h'(x,y,t) \tag{A.6}$$

where the subscript 0 indicates the basic state variables. However, in what follows, the subscript zero notation from the basic state variables will be replaced by capital

letters, i.e.,

$$u = U(y) + u'; \qquad v = v'; \qquad \text{and} \qquad h = H(y) + h'.$$

Neglecting the product of the perturbation terms and using the expression for geostrophic balance,

$$fU(y) = -g\partial_y H(y),$$

we get

$$(\partial_t + U\partial_x)\, u' + (\partial_y U - f)\, v' + g\partial_x h' \;=\; 0 \tag{A.7}$$

$$(\partial_t + U\partial_x)\, v' + f u' + g\partial_y h' \;=\; 0 \tag{A.8}$$

$$(\partial_t + U\partial_x)\, h' + v'\partial_y H + H\,(\partial_x u' + \partial_y v') \;=\; 0 \tag{A.9}$$

Rearranging we get

$$g\partial_x h' + (\partial_t + U\partial_x)\, u' + (\partial_y U - f)\, v' \;=\; 0 \tag{A.10}$$

$$g\partial_y h' + f u' + (\partial_t + U\partial_x)\, v' \;=\; 0 \tag{A.11}$$

$$(\partial_t + U\partial_x)\, h' + H\partial_x u' + (\partial_y H + H\partial_y)\, v' \;=\; 0 \tag{A.12}$$

Seeking for normal-mode solutions of the form

$$\phi'(x, y, t) = \hat{\phi}(y)e^{ik(x-ct)} \tag{A.13}$$

we get

$$g(ik)\hat{h} + (-c + U)\,(ik)\hat{u} + (\partial_y U - f)\,\hat{v} \;=\; 0 \tag{A.14}$$

$$g\partial_y \hat{h} + f\hat{u} + (-c + U)\,(ik)\hat{v} \;=\; 0 \tag{A.15}$$

$$(-c + U)\,(ik)\hat{h} + H(ik)\hat{u} + (\partial_y H + H\partial_y)\,\hat{v} \;=\; 0 \tag{A.16}$$

178

The problem at hand is to solve the linear system of homogeneous ordinary differential equations (A.14–A.16), subject to the boundary condition

$$\hat{u}(y) = \hat{h}(y) = \hat{v}(y) = 0 \qquad \text{as} \qquad y \to \pm\infty \tag{A.17}$$

Dividing (A.14) – (A.16) by (ik), and then dividing (A.15) by $-k^2$, we get

$$g\hat{h} + U\hat{u} + (\partial_y U - f)\, v^* \;=\; c\hat{u} \tag{A.18}$$

$$g^* \partial_y \hat{h} + f^* \hat{u} + U v^* \;=\; c v^* \tag{A.19}$$

$$U\hat{h} + H\hat{u} + \partial_y H v^* + H \partial_y v^* \;=\; c\hat{h} \tag{A.20}$$

where $v^* = \hat{v}/(ik)$, $g^* = \text{-}g/k^2$ and $f^* = \text{-}f/k^2$.

Second-order finite difference approximation is used to discretize the above systems of equations on a staggered C-grid, i.e., we define variables $\hat{u}$ and $\hat{h}$ at half-integer grid points and v^* at the integer grid points. Second-order finite difference discretization results in

$$gh_j + U_j \hat{u}_j + (\delta_y U - f)\frac{v^*_{j+1} + v^*_j}{2} \;=\; c\hat{u}_j \tag{A.21}$$

$$g^* \frac{\hat{h}_{j+1} - \hat{h}_j}{dy} + f^* \frac{\hat{u}_{j+1} + \hat{u}_j}{2} + \frac{U_{j+1} + U_j}{2} v^*_{j+1} \;=\; c v^*_{j+1} \tag{A.22}$$

$$U_j \hat{h}_j + H_j \hat{u}_j + (\delta_y H)_j \frac{v^*_{j+1} + v^*_j}{2} + H_j \frac{v^*_{j+1} - v^*_j}{dy} \;=\; c\hat{h}_j \tag{A.23}$$

Equations (A.23) - (A.22) can be alternatively written in compact form as

$$g\hat{h}_j + U_j \hat{u}_j + l^l_j v^*_j + l_j v^*_{j+1} = c\hat{u}_j \tag{A.24}$$

$$a\hat{h}_j + a^u \hat{h}_{j+1} + b\hat{u}_j + b^u \hat{u}_{j+1} + p_j v^*_{j+1} = c\hat{v}_{j+1} \tag{A.25}$$

$$U_j \hat{h}_j + H_j \hat{u}_j + d^l_j v^*_j + d_j v^*_{j+1} = c\hat{h}_j \tag{A.26}$$

179

where

$$a = -g^*/\Delta y; \quad a^u = g^*/\Delta y; \tag{A.27}$$

$$b = f^*/2; \quad b^u = f^*/2 \tag{A.28}$$

$$p_j = \frac{U_{j+1} + U_j}{2} \tag{A.29}$$

$$d_j^l = \left[\frac{(\delta_y H)_j}{2} - \frac{H_j}{\Delta y}\right]; \text{and} \quad d_j = \left[\frac{(\delta_y H)_j}{2} + \frac{H_j}{\Delta y}\right] \tag{A.30}$$

$$l_j^l = \left[\frac{(\delta_y U)_j - f}{2}\right] \text{ and } \quad l_j = \left[\frac{(\delta_y U)_j - f}{2}\right], \tag{A.31}$$

The linear algebraic system of equations (A.24 - A.26) can be reduced to a matrix eigenvalue problem of the form

$$QX = cX \tag{A.32}$$

where c represents the eigenvalues to be determined, Q is a $(3N - 4)$ by $(3N - 4)$ matrix, and

$$X = [h_1, \cdots, h_{N-1}, u_1, \cdots, u_{N-1}, v_2, \cdots, v_{N-1}]^T \tag{A.33}$$